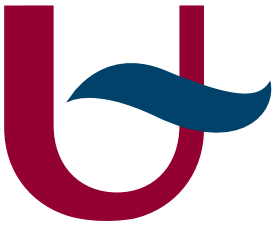

Faculteit Wetenschappen
Departement Fysica

Vortexmaterie in supergeleiders met concurrerende interacties:

vorming van vortex patronen en vortex dynamica

Vortex matter in superconductors with competing interactions:

formation of vortex patterns and vortex dynamics

具有竞争相互作用的超导体中涡旋物质的研究：

静态结构和磁通动力学

Proefschrift voorgelegd tot het behalen van de graad van
Doctor in de Wetenschappen
aan de Universiteit Antwerpen, te verdedigen door

Haijun Zhao

Promotoren: Dr. V. R. Misko
Prof. dr. F. M. Peeters

Antwerpen
2012

Members of the Jury:

Chairman
Prof. dr. J. Tempère, Universiteit Antwerpen, Belgium

Members
Prof. dr. S. Bals, Universiteit Antwerpen, Belgium
Dr. V. R. Misko (Promoter), Universiteit Antwerpen, Belgium
Prof. dr. F. M. Peeters (Co-promoter), Universiteit Antwerpen, Belgium
Prof. dr. D. Lamoen, Universiteit Antwerpen, Belgium
Prof. dr. R. Wördenweber, Forschungszentrum Jülich, Germany
Prof. dr. A. V. Silhanek, Université de Liège, Belgium

Contact Information

Haijun Zhao
Universiteit Antwerpen
Departement Fysica
Groenenborgerlaan 171
2020 Antwerpen
België
Haijun.Zhao@ua.ac.be

Acknowledgment

I was always dreaming of becoming a scientific researcher when I was a kid. Five years ago, I got the opportunity to start my Ph.D project at the University of Antwerp and step by step, I am approaching my dream. People I met in Belgium, especially my teachers and colleagues in the CMT group were so nice that I felt like home here. So at the end of my Ph.D student life, I want to thank all the people who ever helped during my study.

First and foremost, I am heartily thankful to my promotors Dr. V. R. Misko and Prof. dr. F. M. Peeters, whose guidance and encouragement greatly help me to hurdle all the obstacles in my research work. I really appreciate for providing me with an excellent atmosphere for doing research. This thesis would not have been possible without their invaluable help. My grateful thanks also go to Dr. W. V. Pogosov. His hard working spirit greatly encourages me and the co-operation is much indeed appreciated. I also want to thank all my teachers and classmates when I was a master student. During my study, other members of the CMT group also offer me a lot of help, for which I am extremely grateful too.

在此我也要感谢在比利时的中国朋友。感谢中国驻比利时大使馆的老师们多年来对我的关心和帮助。感谢本科阶段指导过我的老师沙健教授和张孝斌教授。感谢给我提供了很多帮助和建议的周世平老师和朱北沂老师。感谢我的室友谭海燕，和你住一起让我学到不少好习惯。感谢我十年的老同学，老友李斌晓丹，陈亚江黄海燕夫妇以及和我一起出国的王斌杰同学。感谢我的师兄师姐：贲哥番茄，林仕鑫，曹珊珊，张一帆，张亮，小麦，老吕，田博，卢博，朱家骥以及鲍莹师姐等，你们都给了我无微不至的关怀。感谢凌云，石慧，林南省，梁灵智，张凌峰，刘超宇，聂臻唐正夫妇，潘菊富，马诚还有经常一起打球的林枫，魏堃等等，和你们一起度过了很多美好的时光。也感谢我其他的同学和好朋友：丁宇，陈江，赵鹏飞，万雨挺，何铭，刘召辉，南志超，刘晓红，童欣杰，管丹丹以及王晓梅等等。最后怀恋我的挚友郝运来，真心的祝福郝叔叔郝阿姨。

在此，最真诚的感谢给一直以来支持我读书的父母，两位姐姐和姐夫。你们多年来辛苦了，我的成绩离不开你们的支持。

This work was supported by the “Odysseus” Program of the Flemish Government and the Flemish Science Foundation (FWO-Vl), the Interuniversity Attraction Poles (IAP) Programme — Belgian State — Belgian Science Policy, and the FWO-Vl.

Preface

More than 100 years have already passed since the discovery of superconductivity. A superconductor has two properties, i.e., perfect conductivity and perfect diamagnetism. However, in high magnetic fields, both properties are compromised. The magnetic flux can penetrate the superconducting material and create a mixed state of quantized vortices. The vortices, driven by supercurrent, dissipate energy and destroy the perfect conductivity. Therefore, stabilizing vortices by, e.g., vortex pinning can greatly improve the applicability of superconductivity.

In mesoscopic superconductors, the interest of studying the vortex matter is closely related to the recent progress in nanofabrication and perspectives of their use in nanodevices manipulating single flux quanta. In the meanwhile, studying vortex states and flux dynamics also helps to understand pattern formation and the dynamic properties of many other physical systems. Our goal is to learn vortex states and flux dynamics in systems with various *competing interactions*. In particular, in this thesis, we focus on the following three cases:
(I) Vortex states in mesoscopic superconductors,
(II) Vortex states and dynamics in superconductors with regular and random pinning sites,
(III) Vortex states in superconductors with competing vortex-vortex interaction.

In the first case, vortex configurations are determined by the competition between the repulsive vortex-vortex interaction and vortex-boundary interaction. We focus on square and triangular boundaries. For a square, the confinement energy always competes with the vortex-vortex interaction for any vorticity (i.e., total number of penetrated flux quanta). For an equilateral triangle, the confinement energy also favors the triangular lattices for some commensurate vorticities. The vortex states in squares and triangles with increasing vorticity is given in **Chapters** 2 and 3, respectively.

In the second case, the formation of vortex patterns and vortex dynamics are determined by the repulsive vortex-vortex interaction and the vortex-pinning attractive interaction. The vortex states in a square pinning array have attracted considerable attention mainly because it can produce a large

increase in the critical current at certain values of the magnetic field, which corresponds to the matching between the number of vortices and the number of pinning sites in the system. The pinning potential favors a square lattice, while the vortex-vortex interaction favors a triangular lattice. The competition between them leads to three different vortex states depending on the pinning strength. We add one more factor to this system, i.e., random pinning, which helps us to understand how disorder affects the vortex lattice with increasing random pinning. The results are presented in **Chapter** 4. By adding an external driving force, we are able to study the vortex dynamics. The different dynamic regimes are discussed in **Chapter** 5.

In the third case, vortex pattern formation depends on the non-monotonic vortex-vortex interaction. Pattern formation in many systems is governed by competing interactions. In general, there is a strong correlation between the formed patterns and the inter-particle interaction. In **Chapter** 6, we modeled a non-monotonic interaction with a repulsive core and an attractive tail. By varying the coefficients of the modeled potential, our model is applicable to many physical systems containing interacting classical objects, e.g., colloids and vortices in low-κ superconductors. In particular, our model can also be used as a model for the vortex states in recently discovered so called "type-1.5" superconductors.

Contents

Chapter 1

Introduction

1.1 Superconductivity: Historical overview

Superconductivity is a phenomenon of exactly zero electrical resistance and expulsion of magnetic fields discovered in many materials when cooled below a characteristic critical temperature. On April 8th, 1911, Dutch physicist Heike Kamerlingh Onnes and his team in Leiden University first cooled mercury down to the temperature of liquid helium, 4 degrees Kelvin (4 K) [1]. He found that its resistance suddenly disappeared. This zero resistance phenomenon, which is now known as superconductivity, was also found in many other metals such as lead and tin. It appears when the temperature is decreased below a critical temperature T_c, which is characteristic of the material. In 1913, he was awarded with the Nobel Prize in physics for his research in this area.

The *perfect conductivity* is the first traditional hallmark of superconductivity. This phenomenon is most sensitively demonstrated by experiments with persistent currents in superconducting rings. By using nuclear resonance to detect any slight decrease in the field produced by the circulating current, File and Mills found such currents were flowing without measurable decrease for a year, and a lower bound was of some 10^5 years for their characteristic decay time [2].

Another hallmark of superconductivity is *perfect diamagnetism*, which was found in 1933 by Meissner and Ochsenfeld [3]. The perfect conductivity can explain that the magnetic field is excluded from entering the superconductor. However, for a field in a normal sample, the field is expelled as the sample cooled across T_c. This phenomenon certainly cannot be explained by the perfect conductivity, which tries to freeze the pre-penetrated fluxes. The existence of such phenomenon, which is now called the *Meissner effect*, implies that superconductivity can be destroyed by the external magnetic field. More precisely, the critical field H_c is a function of the temperature T, which

was found to be well approximated by a parabolic law

$$H_c(T) \approx H_c(0)[1 - (T/T_c)^2]. \tag{1.1}$$

In 1935, brothers Fritz and Heinz London proposed the first, also the simplest meaningful phenomenological theory [4], i.e., the London theory. The major achievement of their equation, called London equation is its ability to explain the Meissner effect. The two hallmarks of superconductivity were reconciled by the phenomenological theory proposed by V.L. Ginzburg and L.D. Landau [named the Ginzburg-Landau (GL) theor] in 1950 [5]. The Ginzburg-Landau theory was very successful to handle the so-called intermediate state of superconductors, in which superconducting and normal domains coexist. However, the underlying microscopic mechanism of superconductivity was unclear. In 1957, John Bardeen, Leon Cooper, and John Schrieffer [6] proposed a microscopic theory (the BCS theory) of superconductivity, which was later widely-accepted and brought them a Nobel Prize in 1972. The BCS theory explained superconductivity at temperatures close to absolute zero for elements and simple alloys. However, for higher temperatures and for different superconductor systems, it is believed that BCS theory alone cannot explain those phenomenons. Another significant theoretical achievement came in 1962, when D. Josephson theoretically considered a superconducting loop separated by a thin non-superconductor or isolator. He predicted that the electrons would "tunnel" thought the non-superconducting region even in the absent of external voltage. His prediction was later conformed experimentally and brought him a share of Nobel Prize in 1973. This tunneling phenomenon is now known as the "Josephson effect", which is applied in many very sensitive electronic devices such as SQUID, an instrument capable of detecting extremely weak magnetic fields.

However, before 1980s, the extremely low critical temperature of superconducting materials greatly limited their applications. According to the BCS theory, physicists believed that superconductivity at temperatures above about 30K is forbidden. In 1986, Alex Müller and Georg Bednorz made a truly breakthrough discovery in the field of superconductivity. They found a lanthanum-based cuprate perovskite material, which had a transition temperature of 35 K [7]. Later in 1987, based on Müller and Bednorz's crystal, superconductivity was found at incredible 93 K [8], which is higher than the boiling point of liquid nitrogen (77 K). Thus, it is possible to use liquid nitrogen instead of liquid helium as coolant. Alex Müller and Georg Bednorz were immediately awarded with Nobel Prize in the following year after their great discovery. The world record Tc of 138 K is now held by a thallium-doped, mercuric-cuprate comprised of the elements Mercury, Thallium, Barium, Calcium, Copper and Oxygen [9].

1.2 Theory of superconductivity

In this section, a brief introduction is given to the theory of superconductivity. As discussed in previous section, the phenomenological Ginzburg-Landau theory was very successful as regards the description of vortex state in superconductors. However, in this thesis, we are interested in vortex static patterns and flux dynamics, i.e., of many vortices, moving, e.g., on complex potential landscapes. In this case, the London theory, which treats vortices as point-like "particles" an appropriate theory to describe the vortex matter. Thus, we mainly discuss the London theory and briefly introduce the Ginzburg-Landau theory and the link between them. We also provide a basic introduction to the microscopic Bardeen-Cooper-Schrieffer (BCS) theory.

1.2.1 London theory

We introduced the London theory in Sec. 1.1. Here we present the derivation of the London equation following Ref. [10].

The standard Drude model for electrical conductivity is given by:

$$m\frac{d\mathbf{v}}{dt} = e\mathbf{E} - \frac{m\mathbf{v}}{\tau} \tag{1.2}$$

Here, $\mathbf{v}$ is the average velocity of electrons, thus, it is constant in a normal metal with steady current. τ is phenomenological relaxation time describing the average time to stop the electrons' motion due to scattering. Set $\mathbf{v} = const$, then $e\mathbf{E} = m\mathbf{v}/\tau$. This gives $\mathbf{J} = ne\mathbf{v} = (ne^2\tau/m)\mathbf{E} = \sigma\mathbf{E}$, i.e., Ohm's law.

To describe the zero resistance of a superconductor, the second term of Eq. (1.2) is zero. Thus, Eq. (1.2) become an accelerative equation, and the supercurrent $\mathbf{J}_s$ is governed by:

$$\frac{d\mathbf{J}_s}{dt} = n_s e^2/m\mathbf{E} \tag{1.3}$$

This is the first London equation describing perfect conductivity. Taking the curl on both sides of Eq. (1.3) and using the Maxwell equation $\nabla \times \mathbf{E} = -(1/c)\partial\mathbf{h}/\partial t$, we obtain

$$\frac{\partial}{\partial t}\left[\nabla \times \mathbf{J}_s + \frac{n_s e^2}{cm}\mathbf{h}\right] = 0 \tag{1.4}$$

Imaging a field is penetrated in a normal conductor, after it was cooled across T_c, Eq. (1.4) indicates that the pre-penetrated flux was freezed inside the superconductor. Of course this does not happen due to Meissner effect. F. London and H. London assumed that

$$\nabla \times \mathbf{J}_s + \frac{n_s e^2}{cm}\mathbf{h} = 0. \tag{1.5}$$

Thus, a supercurrent will be generated to expel the flux outside the sample. Eq. (1.5) is the second London equation describing perfect diamagnetism.

The combination of Eq. (1.5) with the Maxwell equation $\nabla \times \mathbf{h} = 4\pi\mathbf{J}/c$ leads to

$$-\lambda^2\nabla^2\mathbf{h} + \mathbf{h} = 0, \tag{1.6}$$

with

$$\lambda = \sqrt{\frac{mc^2}{4\pi n_s e^2}}. \tag{1.7}$$

Eq. (1.6) indicates that the magnetic field is exponentially decreasing as it is penetrating the superconducting slab. The parameter λ was later named *London penetration length*. Typical values of λ range from 50 to 500 nm [11]. The London theory is successful to describe extreme type-II superconductors where the vortices act like point-particles (see Sec. 1.2.4).

1.2.2 Ginzburg-Landau theory

The Ginzburg-Landau (GL) theory was proposed by V.L. Ginzburg and L.D. Landau based on Landau's previously-established theory of second-order phase transitions. They introduced a pseudowavefuction $\psi(\mathbf{r})$ as a complex order parameter [5] to describe how deep into the superconducting phase the system is.

In the Ginzburg-Landau theory, the free energy density is given by [10]:

$$f_s = f_n + \alpha|\psi|^2 + \frac{\beta}{2}|\psi|^4 + \frac{1}{2m^*}|(-i\hbar\nabla - \frac{e^*}{c}\mathbf{A})\psi|^2 + \frac{h^2}{8\pi}. \tag{1.8}$$

Here, f_n is the free energy density of the normal phase, α and β are phenomenological parameters, m^* and $e^* = 2e$ are the effective mass and charge of a Cooper pair, respectively. $\mathbf{A}$ is the magnetic vector potential. $h^2/8\pi$ is the energy density of penetrated field. In the absence of a field, we have

$$f_s - f_n = \alpha|\psi|^2 + \frac{\beta}{2}|\psi|^4, \tag{1.9}$$

which can be considered as the taking the first two terms of series expansion of f_n in powers of $|\psi|^2 = n_s$. If $\alpha > 0$, Eq. (1.9) takes minimum when $|\psi|^2 = 0$, corresponding to the normal state. On the other hand, if $\alpha < 0$ the minimum occurs when $\psi|^2 = \psi|^2_\infty = -\alpha/\beta$, here $\psi|^2_\infty$ means the Cooper pair density deep in the interior of the superconductor where all the field and currents can not reach. It is obvious that α changes the sign when the temperature crosses T_c. The fourth term of Eq. (1.8) is corresponding to the kinetic energy. The free energy is obtained by taking the volume integral of Eq. (1.8). Minimizing the free energy with respect to fluctuations of ψ and A, one arrives at the GL equations:

$$\alpha\psi + \beta|\psi|^2\psi + \frac{1}{2m^*}(\frac{\hbar}{i}\nabla - \frac{e^*}{c}\mathbf{A})^2\psi = 0 \tag{1.10}$$

and

$$\mathbf{J} = \frac{c}{4\pi} curl\mathbf{h} = \frac{e^*\hbar}{2m^*i}(\psi^*\nabla\psi - \psi\nabla\psi^*) - \frac{{e^*}^2}{m^*c}\psi^*\psi\mathbf{A}, \tag{1.11}$$

The boundary condition at the interface of a superconductor and vacuum or an insulator is given by:

$$(\frac{\hbar}{i}\nabla - \frac{e^*}{c}\mathbf{A}) \cdot \mathbf{n} = 0, \tag{1.12}$$

where $\mathbf{n}$ is a unite vector normal to the interface.

In the absence of magnetic field, we take ψ real since Eq. (1.10) only have real coefficients. For a superconducting slab, ψ only varies in $\mathbf{z}$ direction. Let $\psi = f\psi_\infty$, where $|\psi_\infty|^2$ is the Cooper pair density far away from the interface. Thus, $f(\infty) = 1$. Eq. (1.10) becomes

$$-\xi^2\frac{d^2f}{dz^2} - f + f^3 = 0. \tag{1.13}$$

with

$$\xi = \sqrt{\frac{\hbar^2}{2m^*|\alpha|}}. \tag{1.14}$$

The parameter ξ describes how quick the Cooper pair density heals to $|\psi_\infty|^2$, thus called *coherence length*. ξ together with the London penetration length λ composed the two characteristic lengths of a superconductor. Both of them are proportional to $|\alpha|^{-1/2}$, thus, depends on the temperature. However, the Ginzburg-Landau parameter ($\kappa = \lambda/\xi$) is approximately independence of the temperature. Depending on κ being bigger or smaller then $1/\sqrt{2}$, the bulk superconductor is classified into two groups: type-I and type-II. For a type-I bulk superconductor with the magnetic field not strong enough to destroy the superconductivity (i.e., $H < H_c$), the superconductor have a single phase, i.e., Meissner state. For a type-II bulk superconductor, the superconductor have the Meissner state when then magnetic field is small (i.e., $H < H_{c1}$) and the superconductivity is destroyed when the magnetic field is strong (i.e., $H > H_{c2}$). In the intermediate region when $H_{c1} < H < Hc2$, the magnetic field is penetrated into the sample in the form of *vortices* and the penetrated field is quantized in units of the flux quantum $\Phi_0 = hc/2e$. This classification is only valid in bulk superconductors. For mesoscopic superconductors, it also depends on the geometry.

1.2.2.1 High-κ approximation

Considering the case when the Ginzburg-Landau parameter ($\kappa \gg 1$), comparing with the field, the density of Cooper pairs heals to a constant in a short distance near the interface of the superconductor state and normal state (see

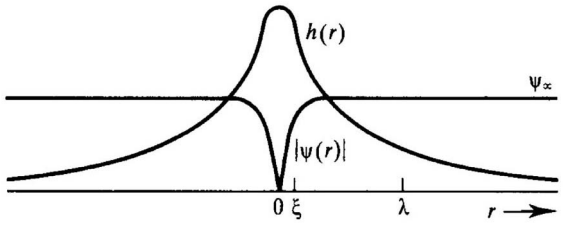

Fig. 1.1 Structure of an isolated Abrikosov vortex in a material with $\kappa \approx 8$. The maximum value of $h(r)$ is approximately $2H_{c1}$ (*After Ref.* [10])

.

Fig. 1.1). Therefore, the order parameter ψ in high-κ superconductors can be treated uniform except the core region of the vortex with a radius $r \simeq \xi$ and the region near the surface. Thus, the two Ginzburg-Landau equations (i.e., Eqs. (1.10) and (1.11)) turn into only one equation (i.e., the London equation Eq. (1.6). In this case, vortices act as point-like particles, which allows us to use molecular dynamics simulation to study the vortex configurations in this thesis.

To describe the vortex states, Eq. (1.6) is not suitable since the fluxoid for any path would be zero. Considering the case where the vortex flux lines are straight and paralleling to the external magnetic field (e.g., superconducting films), the vortex core can be taken into account by adding an additional term to Eq. (1.6):

$$-\lambda^2\nabla^2\mathbf{h} + \mathbf{h} = \Phi_0\hat{\mathbf{z}}\sum_i \delta(\boldsymbol{r} - \boldsymbol{r}_i), \tag{1.15}$$

where $\hat{\mathbf{z}}$ is a unit vector alone the vortex, $\delta(\boldsymbol{r} - \boldsymbol{r}_i)$ is a two-dimensional δ function, $\boldsymbol{r}_i$ is position of the vortex. With those modifications, one can first solve Eq. (1.15) to obtain the magnetic field distribution inside the superconductor, and then calculate the Gibbs free energy, which can be minimized to find the stable states.

1.2.3 BCS theory of superconductivity

In 1957, John Bardeen, Leon Cooper, and John Schrieffer [6] published the first truly microscopic theory of superconductivity. Early study showed that, the crystal structure did not change when a material changed from normal state to superconducting state. Thus, the phase transition is due to the change of the electron state. The electrons in a normal metal are described by a Fermi sea. In 1956, Leon Cooper showed that at sufficiently low temperatures, the Fermi sea of electrons is unstable when there is an arbitrarily small at-

tractive interaction between electrons [12]. Electrons near the Fermi surface wound bind together and form electron pairs, which are now called *Cooper pairs*. Those coupled electrons have opposite momenta and spins. They act like bosons, which lead to a condensation of the electrons into a state leaving a band gap above them. Such condensation is seen with superfluid helium. Such gap inhibits the collision interactions which lead to ordinary resistivity. Thus for thermal energy proportional to temperature not sufficient to overcome the band gap, the material exhibits zero resistivity. The magnetic flux quantization shows the effective unit of charge is $2e$ rather than e, which indicates the perfect conductivity is cause by Cooper pairs' motion instead of normal electrons.

The origin of this attraction is a quantum effect, but it can roughly explained in the flowing classical picture: one electron slightly deforms its neighbor lattices, i.e., exchanging momenta with phonons. This deformation causes the increase of positive charges, which attracts the second electron. At long distances this attraction between electrons can overcome the screened electrons' repulsion due to their negative charge, and cause them to pair up. This electron-phonon-electron attractive interaction was provided by the isotope effect on the superconducting transition temperature.

In 1959, Gor'kov showed that the Ginzburg-Landau theory is just a limiting form of the BCS theory which is valid near T_c. The order parameter ψ can be seen as the wavefunction of the center-of-mass motion of the Cooper-pairs in BSC theory.

1.2.4 Vortex-vortex interaction

1.2.4.1 Vortex-vortex interaction in infinite superconductors

One isolated Abrikosov vortex

Considering the case where one vortex is located in an infinite large sample. The London equation has an exact solution in this case [10]:

$$h(r) = \frac{\Phi_0}{2\pi\lambda^2} K_0\left(\frac{r}{\lambda}\right), \tag{1.16}$$

where K_0 is a zeroth order Hankel function of imaginary argument. To avoid the divergence when $r \to 0$, a cut off at $r \sim \xi$, where the Cooper pair density starts dropping to zero is needed. The London free energy per unit volume of the superconducting sample is given by

$$\mathscr{F} = \frac{1}{8\pi A}\int d^2r\{\mathbf{h}^2 + \lambda^2|\nabla\times\mathbf{h}|^2\}. \tag{1.17}$$

Using:

$$\begin{aligned} |\nabla\times\mathbf{h}|^2 &= (\nabla\times\mathbf{h})\cdot(\nabla\times\mathbf{h}) \\ &= \nabla\cdot(\mathbf{h}\times\nabla\times\mathbf{h}) + \mathbf{h}\cdot(\nabla\times\nabla\times\mathbf{h}) \\ &= \nabla\cdot(\mathbf{h}\times\nabla\times\mathbf{h}) - \mathbf{h}\nabla^2\mathbf{h}, \end{aligned} \tag{1.18}$$

one obtains:

$$\begin{aligned}\mathscr{F} &= \frac{1}{8\pi A}\int d^2r\mathbf{h}\cdot(\mathbf{h}-\lambda^2\nabla^2\mathbf{h}) + \frac{\lambda^2}{8\pi A}\int d^2r\nabla\cdot(\mathbf{h}\times\nabla\times\ \mathbf{h}).\\ &= \frac{1}{8\pi A}\int d^2r|\mathbf{h}|\Phi_0\sum_i\delta(\boldsymbol{r}-\boldsymbol{r}_i) + \frac{\lambda^2}{8\pi A}\oint dl\mathbf{h}\times\nabla\times\ \mathbf{h}. \qquad (1.19)\end{aligned}$$

where Eq. (1.15) and Gauss theorem was used in the last step. The integration in Eq. (1.19) excludes the cores of vortices, so the first term is zero and the second term gives contribution in encircling the cores of vortices (also at the boundary for the finite sample). For the isolated vortex, one obtains:

$$\epsilon_1 = \frac{\lambda^2}{8\pi}\left[h\frac{dh}{dr}2\pi r\right]_\xi, \qquad (1.20)$$

where ϵ_1 is the energy per unit length. Using a approximation

$$K_0(r/\lambda) \approx 0.12 - ln(r/\lambda), \quad \text{when} \quad \xi \ll r \ll \lambda, \qquad (1.21)$$

one arrives at

$$\epsilon_1 = \frac{\phi_0}{8\pi}h(\xi) \approx \frac{\phi_0}{8\pi}h(0), \qquad (1.22)$$

where $h(\xi) \approx h(0)$ because the density of Cooper pairs drops to zero when $r \leq \xi$. Using Eq. (1.21) again and dropping the term 0.12 as not significant in view of the approximation made in imposing a cut off at ξ, we finally arrive at

$$\epsilon_1 = \left(\frac{\Phi_0}{8\pi\lambda}\right)^2 ln\ \kappa. \qquad (1.23)$$

Since this depends only logarithmatically on the core size, the result should be quite reliable, despite the crude treatment of the core.

Interaction between two well separated vortex lines

In the high-κ case, the field is given by

$$\begin{aligned}\mathbf{h(r)} &= \mathbf{h}_1(\mathbf{r}) + \mathbf{h}_2(\mathbf{r})\\ &= \big[h(|\mathbf{r}-\mathbf{r}_1|) + h(|\mathbf{r}-\mathbf{r}_2|)\big]\hat{\mathbf{z}}, \qquad (1.24)\end{aligned}$$

where $\mathbf{r}_1$ and $\mathbf{r}_2$ are the coordinates of the two vortices and $h(r)$ is given by Eq. (1.16). The energy can be obtained by substituting this in Eq. (1.19). The result for the increase in free energy per unit length associated with the interaction between the vortex lines can be written

$$\begin{aligned}\Delta F &= \frac{\Phi_0}{8\pi}[h_1(\mathbf{r}_1)+h_1(\mathbf{r}_2)+h_2(\mathbf{r}_1)+h_2(\mathbf{r}_2)] \\ &= 2\left[\frac{\Phi_0}{8\pi}h_1(\mathbf{r}_1)\right]+\frac{\Phi_0}{4\pi}h_1(\mathbf{r}_2), \end{aligned} \tag{1.25}$$

where we use the symmetry properties $h_1(r_1) = h_2(r_2)$ and $h_1(r_2) = h_2(r_1)$. The first term is just the sum of the energies of two individual vortex lines. The second term is the well-known vortex-vortex interaction energy that we were looking for

$$F_{12} = \frac{\Phi_0}{4\pi}h_1(\mathbf{r}_2) = \frac{\Phi_0^2}{8\pi^2\lambda^2}K_0(r_{12}/\lambda). \tag{1.26}$$

As shown in Fig. 1.2, this falls off as $r_{12}^{1/2}e^{-r_{12}/\lambda}$ at large distances and varies logarithmically at small distances. The interaction is repulsive for the usual case, in which the flux has the same direction in both vortices. The force arising from this interaction is obtained by taking a derivative of F_{12}.

$$\mathbf{f}_{12} = \frac{\Phi_0^2}{8\pi^2\lambda^3}K_1(r_{12}/\lambda)\hat{\mathbf{r}} \tag{1.27}$$

where $\hat{\mathbf{r}} = \mathbf{r}_{12}/r_{12}$ is a unit vector and K_1 is a first order Hankel function of imaginary argument. The vortex can be in static equilibrium at any given position only if the total force from the other vortex is zero. This can be accomplished if each vortex is surrounded by a symmetrical array such as square or triangle. However, it turns out that square and any other kind of array except triangle are unstable states. The triangle array is stable [13].

Unfortunately even the triangle array will feel a force transverse to any transport current, so that the vortices will move unless they are pinned in place by inhomogeneities in the medium. Since flux motion causes energy dissipation and induces a longitudinal resistive voltage, this situation is crucial in determining the usefulness of type II superconductors in the construction of high-field superconducting solenoids, where strong currents and fields inevitably must coexist.

1.2.4.2 Vortex-vortex interaction in mesoscopic superconductors

The growing interest in studying vortex matter in mesoscopic and nano-patterned superconductors is closely related to recent progress in nano-fabrication and perspectives of their use in nano-devices manipulating single flux quanta. Therefore, it become important to describe vortex structures in mesoscopic superconductors of various geometries. The vortex-vortex interaction in mesoscopic superconductors can be found by solving Eq. (1.15) plus the boundary conditions at the interface of superconductor and vacuum (or insulator):

$$j|_n = 0, \tag{1.28}$$

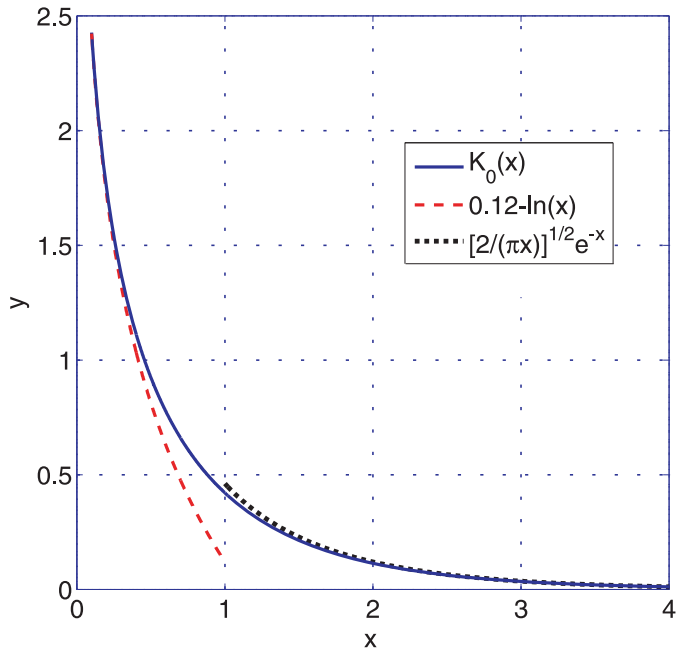

Fig. 1.2 Plot of the zeroth-order Bessel function $K_0(x)$ (solid curve) and its asymptotic approximations for small (dashed curve) and large (dotted curve) x.

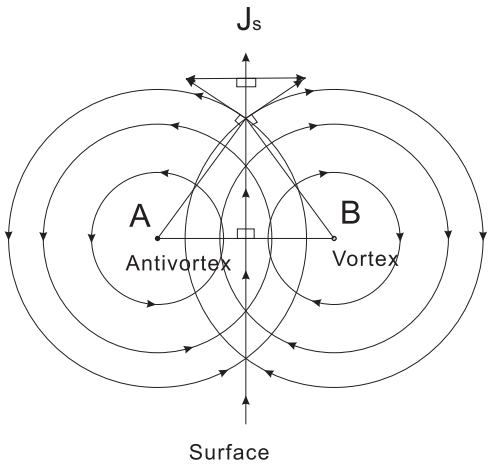

Fig. 1.3 Illustration of the image method. The normal component of the current of a vortex near a slab surface can be canceled by placing an anti-vortex at the mirror image position.

where $j|_n$ means the normal current.

In principle, the screening current around the vortex core is circular when vortices are far away from the boundary. However, near the boundary, the restriction on the supercurrent (Eq. (1.28)) leads to the interaction between vortices and boundary. For a vortex near an infinitely long straight boundary, the boundary condition is identical to the placing an anti-vortex at the mirror image position (see Fig. 1.3). Using image method, Eq. (1.15) and Eq. (1.28) were solved for circular symmetry [14], which allows one to calculate the Gibbs free energy for an arbitrary vortex configuration in a mesoscopic superconducting disk [14]. The result can also be found for other geometries (e.g., stripes, squares and triangles) by using the Green function method and the image technique (see, e.g., Ref. [15]). By minimizing the Gibbs free energy using various methods (e.g., MD or MC simulation), one can find stable vortex configurations of superconductors with different geometry.

1.2.5 Superconductors with non-monotonic vortex-vortex interaction

In superconductors, the vortex-vortex interaction is usually considered to be either repulsive (in type-II superconductors where the GL parameter κ, i.e., the ratio of the magnetic field penetration depth λ to the coherence length ξ, $\kappa > 1/\sqrt{2}$) or attractive (in type-I superconductors, where $\kappa < 1/\sqrt{2}$ and vortices are unstable) while vortices do not interact with each other at the so-called "dual point" when $\kappa = 1/\sqrt{2}$ [16]. In type-II superconductor (as shown by Kramer [16, 17]), the vortex-vortex interaction can be presented in the form:

$$V(r) = 2\pi c^2(\kappa) K_0(l) - \frac{\pi}{\kappa^2} d^2(\kappa) K_0(\sqrt{2}\kappa l). \tag{1.29}$$

Here,$K_0(l)$ is the modified Bessel function of zero order, $l = r/\xi$, $c(\kappa)$ and $d(\kappa)$ are coefficients which depend on κ. When $\kappa = 1/\sqrt{2}$, $c = d$, thus $V(r) = 0$. However, a deeper analysis of the vortex-vortex interaction in type-II superconductors near the dual point revealed an attractive tail [17–20]. This repulsive-attractive interaction (similar to that in colloids and other systems with non-monotonic interaction [21–23]) was used for the explanation of unusual patterns in the intermediate state in low-κ superconductors (e.g., Nb): islands of Meissner phase surrounded by vortex phase or vice versa, i.e., vortex clusters surrounded by Meissner phase [18, 19]. In Ref. [24, 25], the vortex-vortex interaction was modeled as:

$$F_{vv} = f_0(\lambda/r - q\exp(-r/\xi)), \tag{1.30}$$

where f_0 is the unit of force, q is a coefficient to adjust the real vortex-vortex interaction. Eq. (1.30) is very similar to the modeled vortex-electron interaction used in 2D electron systems [21–23].

Recent discovery of "type-1.5" superconductors [26] induced a new wave of interest (see, e.g., Ref. [27, 28]) to systems with non-monotonic interactions,

due to the fact that the observed vortex patterns in those superconductors revealed a clear signature of the repulsive-attractive vortex-vortex interaction. In particular, several properties (e.g., vortex lattice with voids, the nearest-neighbor distribution) of the observed vortex patterns were explained using a simple model that involved a non-monotonic vortex-vortex interaction based on a more general approach to multi-order-parameter condensates [29].

1.2.6 Vortex dynamics: Langevin-equation approach

1.2.6.1 Langevin equation

The Langevin equation was originally developed by French physicist Paul Langevin. Considering a Brownian particle in a fluid in one dimension, the corresponding stochastic dynamics is described by the inertial Langevin equation [30, 31]:

$$m\ddot{x} = -V'(x) - m\gamma\dot{x} + F + \xi(t), \tag{1.31}$$

where m and $x(t)$ are the mass and coordinate of the Brownian particle, respectively, $V(x)$ can be some external potential, γ is the friction coefficient, F is the external force, the prime indicates differentiation with respect to x, and the overdot differentiation with respect to time t, $\xi(t)$ is the thermal fluctuation term. If the stochastic process satisfies the Markov property, i.e., the fluctuations of the random force are faster than any other process, then $\xi(t)$ obeys the following conditions:

$$\langle \xi(t) \rangle = 0 \tag{1.32}$$

and

$$\langle \xi(t)\xi(t') \rangle = 2D_p\delta(t - t'), \tag{1.33}$$

where the momentum-diffusion strength reads $D_p = m\gamma k_B T$, with k_B denoting the Boltzmann constant and T the temperature of an equilibrium heat bath.

1.2.6.2 Overdamped limit of the Langevin equation

We now consider the overdamped limit of Eq. (1.31), i.e., γ is large. If we only consider the friction force, we have $\dot{x} \propto exp(-\gamma t)$, which means that the particle slows down from its initial velocity with characterisitic time $\tau = 1/\gamma$. Thus, when τ is much shorter than any other relevant time scale (except thermal fluctuations), the Brownian particle looses its velocity immediately when the force is zero. Hence the acceleration term in Eq. (1.31) can be ignored (this is also called the Smoluchowski approximation) and the overdamped Langevin equation reads:

$$m\gamma\dot{x} = -V'(x) + F + \xi(t). \tag{1.34}$$

Here, $m\gamma$ can be scaled to unity for convenience. Thus, the Brownian particle acts like a massless particle in this case. A strict mathematical derivation of Eq. (1.34) can be found in Ref. [31].

1.3 Experimental methods of vortex imaging

To investigate the position of the vortices in a superconductor, a number of experimental methods and techniques have been developed. In this section, we mainly focus on the Bitter decoration technique, because Bitter decoration images will be compared with our numerical results in **Chapters** 2 and 3. We also provide a brief introduction to other techniques, e.g., scanning tunneling microscopy (STM), magnetic force microscopy (MFM), scanning SQUID microscopy (SSM) and scanning Hall probe microscopy (SHPM).

1.3.1 Bitter decoration technique

The Bitter decoration technique was first developed by Träuble and Essmann in 1966 [32, 33] and independently by Sarma and Moon [34]. The main principle of the decoration technique is as follows [35]: it uses small ferromagnetic particles to sense the field at the surface of a superconductor. Those small ferromagnetic particles are collected in the region where a magnetic field is present, i.e., in our case vortices. Thus, static vortex configuration can be observed by imaging the distribution of those ferromagnetic particles. However, in practice, it is not so easy to decorate vortices: first, because the size of the ferromagnetic particles must be much smaller than the vortex size, i.e., 5-10 nm. Second, the particles should not stick together on their way to the superconductor surface. Third, the kinetic energy of ferromagnetic particles is small. Those requirements are satisfied by evaporating a ferromagnetic material at a small distance from the superconductor in a background of helium gas. The particle size and concentration, as well as the experiment temperature are adjusted by the helium pressure. The particles are held in place once on the surface, giving a "snapshot" of vortex structure at the time of decoration. Decorations are normally carried out at $T = 4.2$ K, so no temperature dependence of the equilibrium vortex structures are involved. Decorations at higher temperature become difficult because an increased kinetic energy blurs the decoration image. After the decoration, the superconductor is warmed up to room temperature and the distribution of ferromagnetic particles, which replicates the distribution of vortices (or magnetic domains), is examined in an optical microscope or scanning electron microscope (SEM). However, decoration studies are limited to low magnetic field case, i.e., there is little overlap of vortices. For higher fields, one have to use other methods, e.g., scanning tunneling microscope (STM).

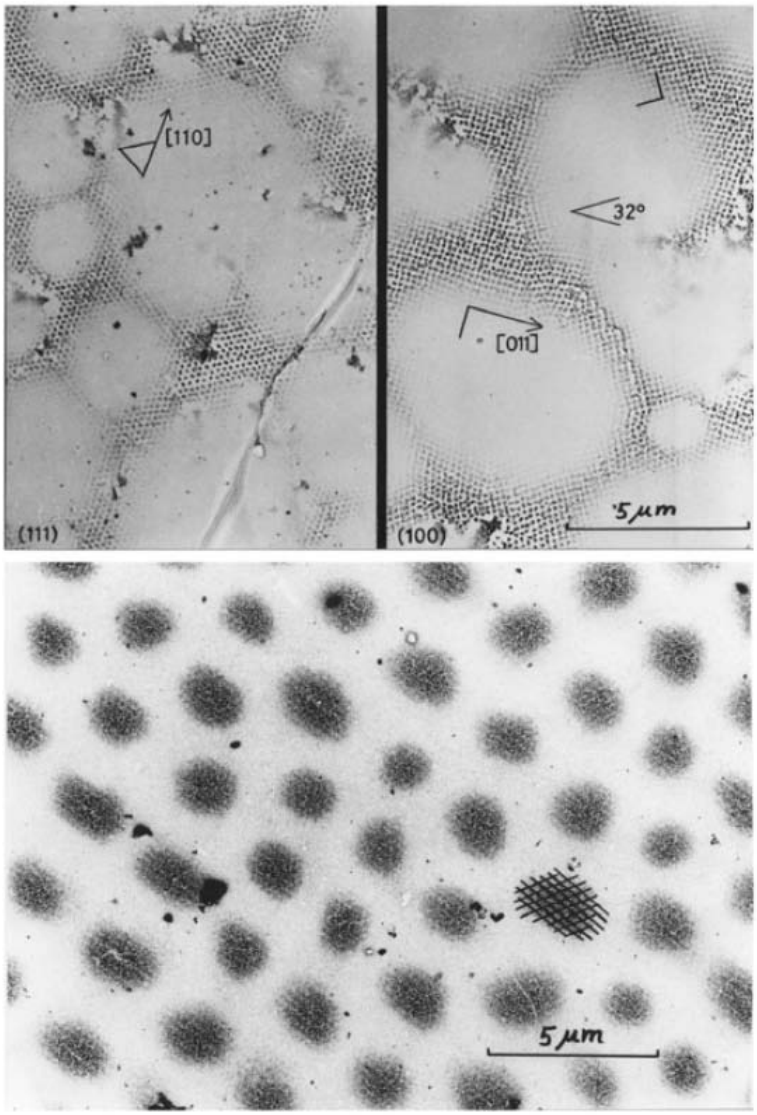

Fig. 1.4 Flux-line lattice observed at the surface of type-II superconductors in an electron microscope after decoration with Fe microcrystallites ("magnetic smoke"). Top: High-purity Nb disks of 1 mm thick and 4 mm diameter, for different crystallographic orientations [110] and [011], at temperature $T = 1.2$ K and applied magnetic field $B_a = 800$ Gauss. Due to demagnetizing effects and the small $\kappa \approx 0.70$, round islands of Meissner phase are surrounded by a regular vortex lattice ("intermediate mixed state"). Bottom: High-purity Nb foil 0.16 mm thick at $T = 1.2$ K and $B_a = 173$ Gauss (*After Ref.* [19]).

There have been many exciting discoveries realized from Bitter decoration, e.g., visualization of the vortex configurations in a superconducting Niobium disc (see for more discussion Sec. 1.4.1.1), the attractive vortices in low-κ superconductors [18, 19] (see Fig. 1.4) and the unusual vortex configurations in the MgB_2 [26] superconductor (see Fig. 1.5), which were also introduced in Sec. 1.2.5. More details on this technique, can be found in the review paper Ref. [35].

1.3.2 Scanning tunneling microscopy (STM) and scanning tunneling spectroscopy (STS)

The scanning tunneling microscope (STM) was invented by Binnig and Rohrer for which they received the Nobel Prize in Physics in 1986, together with Ernst Ruska for his work on the development of electron microscopy. The STM is based on the concept of quantum tunneling. The operation of a STM is started by bringing a sharp conducting tip to the surface that one wants to examine. The tip's motion is controlled by a piezoelectric tube in all three dimensions. The tip-sample separation W is typically in the 4-7 Å range, which is the equilibrium position between attractive and repulsive interactions. In this situation, adding a voltage bias between the tip and sample will create a tunneling current that can be measured. The resulting tunneling current is a function of tip-sample distance, applied voltage, and the local density of states (LDOS) of the sample. When the tip is moved across the sample in the x-y plane, a constant current is maintained by adjusting the height of the tip. Therefore, recording the tip's motion displays the topography of the sample surface.

The STM can also be used to probe LDOS and the band gap of surfaces at the atomic scale. This type of measurement is called scanning tunneling spectroscopy (STS). The operation of STS is obtained by fixing a STM tip above the sample at a particular position, and then measuring the electron tunneling current as a function of the voltage between the tip and the sample. Therefore, an I-V curve is obtained, which allows one to calculate the LDOS as a function of electron energy. Additionally, topographic and spectroscopic data can be recorded simultaneously.

It is very interesting to investigate the vortex states in superconductors with topographic defects, i.e., vortex pinning. A STM can observer the topography of a superconductor on the atomic scale and determining the vortex normal core position in the mean time, since the tunneling current is related to the density of states.

1.3.3 Scanning magnetic microscopy

In a superconductor, the vortex state can also be imaged by detecting its magnetic structure by using scanning magnetic microscopy. Here we briefly

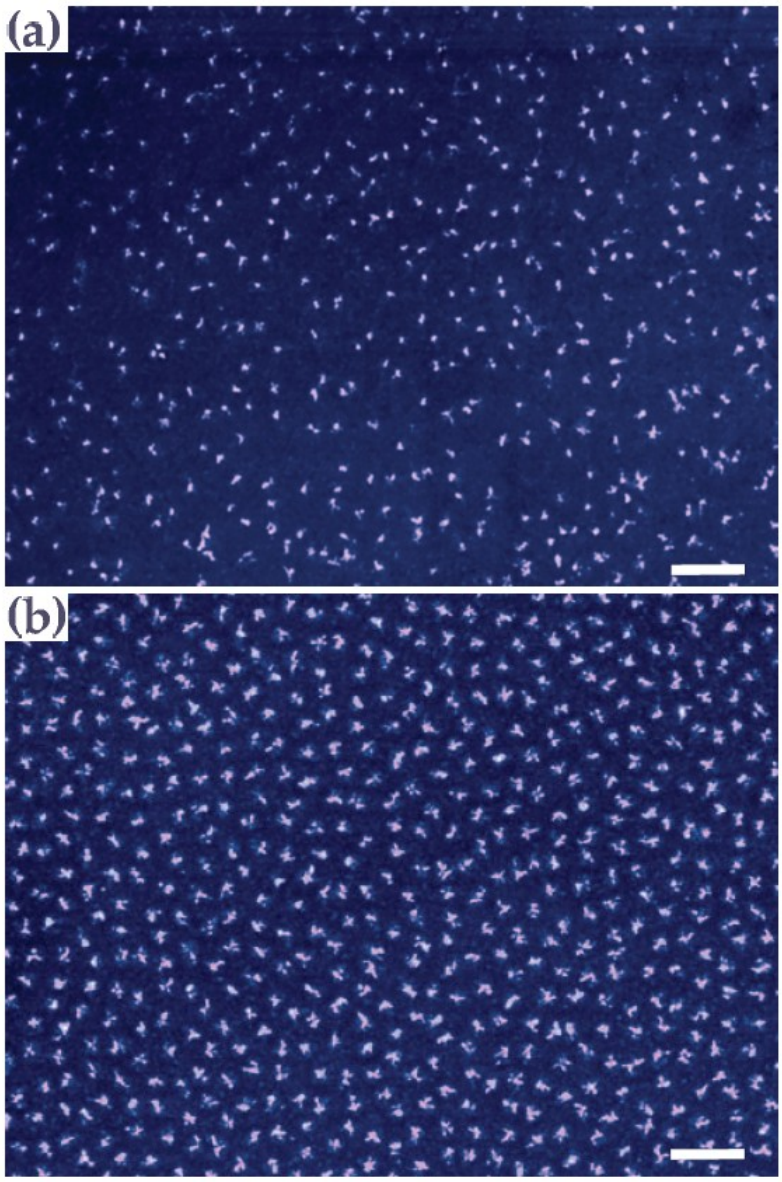

Fig. 1.5 Magnetic decoration images of the vortex structure at T=4.2 K and H=1 Oe in (a) MgB_2 and (b) $NbSe_2$ single crystals. The scale bars in the images correspond to 10 μm (*After Ref.* [26]).

introduce three types of scanning magnetic microscopy: magnetic force microscopy (MFM), scanning SQUID microscopy (SSM) and scanning Hall probe microscopy (SHPM) (see Ref. [36] for a review).

MFM is an imaging technique based on atomic force microscopy (AMF), where a sharp magnetized tip controlled by a piezoelectric tube (similar as STM) is used to detect the magnetic structure of the sample surface. The sample is often scanned by using the "lift height" method: first, the tip is brought into close proximity of the sample and scans the topography through a normal AMF measurement. Second, the magnetized tip is lifted further away from the sample and scans the same imaging region. Then, the magnetic signal is extracted. Typically, a resolution of 30 nm can be achieved. MFM tips can also be used to manipulate vortices.

SSM uses a superconducting quantum interference device (SQUID) to detect the magnetic flux. A SQUID is a superconducting ring with at least one Josephson weak link. For SSM applications, a SQUID with two weak links is most often used. SQUIDs are currently the most sensitive magnetic sensors, which makes a SSM to be the most sensitive tool for measuring the magnetic field. However, since such a sensor normally has a much larger size than a tip, comparing with MFMs, the resolution of SSMs are very limited (typically $1 \sim 10$ μm). However, very recently, nanoscale SQUIDs ($\sim$100 nm) mounted on sharp tips have been realized [37].

SHPM is a variety of a scanning probe microscope (SPM), which uses a nano-Hall probe to scan over the sample surface to measure the perpendicular component of the surface magnetic fields [38]. A Hall probe uses a conducting cross made with a two-dimensional electron gas (2-DEG) to measure the magnetic field. Considering a 2-DEG in the x-y plane in the presence of a magnetic field B_z perpendicular to the plan. Due to the Lorentz force, the magnetic field creates a transverse voltage $V_x = I_y B_z / n_{2d} e$ when a current I_y is applied in the y direction, where n_{2d} is the carrier density in two dimension. Therefore, the perpendicular magnetic field B_z can be obtained by measuring the Hall voltages V_x. SHPM can be used over a broader temperature range than SSM and in contrast to MFM, which measures magnetic field gradients, it gives quantitative values of the magnetic field perpendicular to the probe. Similar as SSM, the resolution of SHPM is rather low (typically 0.35 μm).

1.4 Vortex pattern formation and flux dynamics

1.4.1 Vortex states in mesoscopic superconductors

As distinct from bulk superconductors, vortex states in nano- and mesoscopic samples are determined by the interplay between the vortex-vortex interaction (which is modified due to the presence of boundaries) *and* the confinement.

In general, the shape of a mesoscopic sample is inconsistent with the triangular Abrikosov lattice, and the vortex patterns display strong features of the sample shape, which may differ strongly from a triangular lattice. Strong finite size effects in conjunction with strong *shape* effects determine the vortex configurations. For example, the circular shape forces the vortices to form circular symmetric shells [39–47]. Furthermore, due to strong confinement effects in small disks vortices can even merge into a giant vortex (GV), i.e., a single vortex containing more than one flux quantum [43, 48]. In squares and triangles, vortex configurations are also strongly affected by the sample shape. Strong boundary effects can even lead to symmetry-induced vortex states with antivortices [49–52] (i.e., the symmetry of the vortex configuration with antivortices can be restored by generation of a vortex-antivortex pair). Therefore, it is expected that different geometries will favor different arrangements of vortices and will make certain vortex configurations more stable than others.

1.4.1.1 Vortex states in mesoscopic disks

A mesoscopic superconducting disk is the most simple system to study confined vortex matter where the effects of the sample boundary play a crucial role. Early studies shows that in thin disks or disks with small radii, vortices arrange themselves in rings [39–44]. In Ref. [14], the vortex-vortex interaction as well as the Gibbs free energy of arbitrary vortex configuration was calculated within the London theory. By numerically minimizing the Gibbs free energy, the authors of Ref. [14] found that up to $L = 5$ (L is the vorticity, i.e, the total number of penetrated flux quanta) the vortices form only polygons, while for $L = 6$ it is more favorable to have a pentagon and one vortex at the center although the energy difference is small. Palacios calculated the vortex matter structure and associated magnetization in mesoscopic disks [53]. Geim *et al.* [54] studied experimentally and theoretically the magnetization of different vortex configurations in superconducting disks. Later, this magnetization was analyzed by Schweigert and Peeters [43] using the nonlinear Ginzburg-Landau (GL) functional. Kanda *et al.* studied the response of a mesoscopic superconducting disk to perpendicular magnetic fields by using the multiple-small-tunnel-junction method. The vortex distributions in mesoscopic superconducting disks in an inhomogeneous applied magnetic field was studied in Ref. [55, 56], where Wigner molecules of vortices and antivortices are found. In the work of Baelus *et al.* [45] the distribution of vortices over different vortex shells in mesoscopic superconducting disks was investigated in the framework of the nonlinear GL theory and the London theory. They found vortex shells and combination of GV and vortex shells for different vorticities L.

The direct observation of rings of vortices in mesoscopic Nb disks was done by Grigorieva *et al.* [47, 57] using the Bitter decoration technique. The formation of concentric shells of vortices was studied for a broad range of

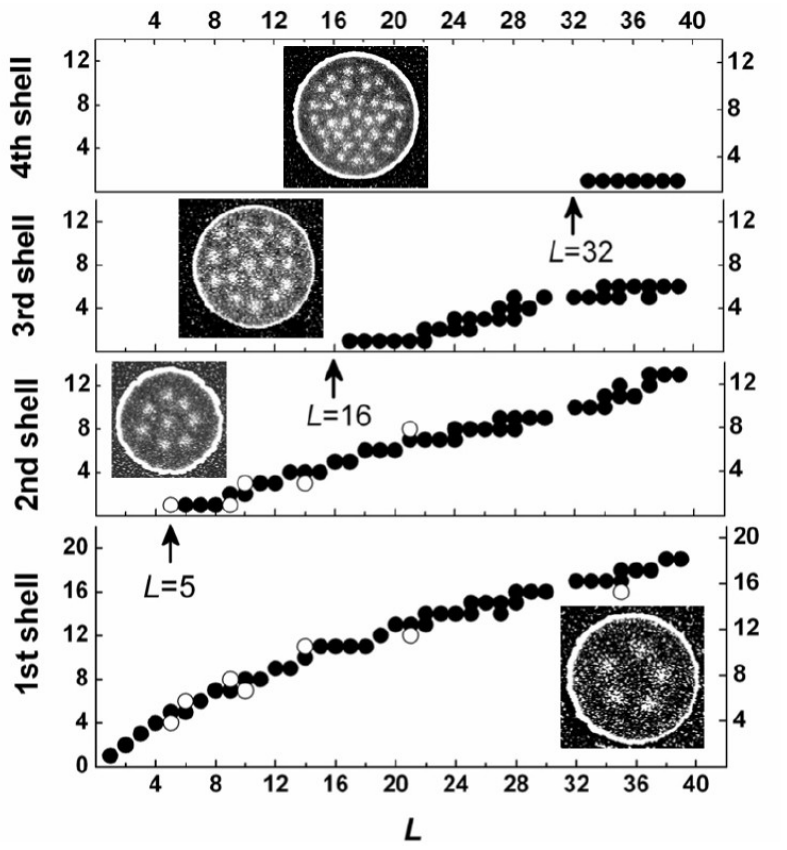

Fig. 1.6 Number of vortices populating different shells as a function of L. Open circles show numbers of vortices in a shell corresponding to the configurations that are clearly identified as metastable. Arrows indicate magic numbers, i.e., L corresponding to closed shell configurations, just before the appearance of the 2nd, 3rd, and 4th shell. Insets: SEM images of vortex states with different numbers of shells (After Ref. [47]).

vorticities L (see Fig. 1.6). From images obtained for disks of different sizes in a range of magnetic fields, the authors of Ref. [47] traced the evolution of vortex states and identified stable and metastable configurations of interacting vortices. Furthermore, the analysis of shell filling with increasing L allowed them to identify magic number configurations corresponding to the appearance of consecutive new shells. The filling rules found in Ref. [47] were later systematically studied in Ref. [46]. It was found that for vorticities up to $L = 5$ all the vortices are arranged in a single shell. Second shell appears at $L = 6$ in the form of one vortex in the center and five in the second shell [state (1,5)], and the configurations with one vortex in the center remain stable until $L = 8$ is reached, i.e., (1,7). The inner shell starts to grow at $L = 9$, with the next two states having 2 vortices in the center, (2,7) and (2,8), and so on. It is clear that vortices generally form circular configurations as expected for a disk geometry. It was also shown in Ref. [46] that some of the vortex configurations are very sensitive to the size of the disk. For instance, depending on the radius of the disk, there are two crossovers between states (1,8) and (2,9). The (1,8) to (2,7) transition occurs for large disks due to the effect of the London screening , while in small disks this transition happens due to the compression of the outer eight-vortex shell.

1.4.1.2 Vortex states in squares, triangles and other noncirclar geometries

Mesoscopic superconductors with square, triangle and other noncirclar geometries have attracted a considerable interest due to the opportunity to study the interplay between the circular symmetry of the applied magnetic field and noncircluar boundaries. Moshchalkov *et al.* [58] measured the superconducting/normal transition in superconducting lines, squares, and square rings using resistance measurements. Bruyndoncx *et al.* [59] calculated the $H - T$ phase diagram for a square with zero thickness in the framework of the linearized Ginzburg-Landau theory, which is only valid near the superconducting/normal boundary. They compared their results with the $H - T$ phase boundary obtained from resistance measurements. Using the nonlinear Ginzburg-Landau equations, the distributions of the order parameters and magnetic field in square loops with leads attached to it were studied [60, 61]. It was found that the order parameter distribution in the loop is very inhomogeneous, with the enhancement near the corners of the square loop. Using the criterion of a "superconducting path", the $H - T$ phase boundary was calculated [60, 61], in agreement with the experiment [58].

Schweigert and Peeters [42, 62], calculated the nucleation field as a function of the sample area for disks, squares, and triangles with zero thickness. Jadallah *et al.* [63] computed the superconducting/normal transition for mesoscopic disks and squares of zero thickness. For macroscopic squares, the magnetic field distribution and the flux penetration are investigated in detail by experimental observations using the magneto-optical Faraday effect and by

first-principles calculations that describe the superconductor as a nonlinear anisotropic conductor [64, 65]. The noncirclar geometry brings new properties to the vortex matter, which offers unique possibilities to study the interplay between the C_∞ symmetry of the magnetic field and the discrete symmetry of the boundary conditions. Superconductivity in mesoscopic equilateral triangles, squares, etc., in the presence of a magnetic field nucleates by conserving the imposed symmetry (C_3, C_4) of the boundary conditions [49, 50] and the applied vorticity. In an equilateral triangle, for example, in an applied magnetic field H generating two flux quanta, $2\Phi_0$, superconductivity appears as the C_3-symmetric combination $3\Phi_0 - \Phi_0$ (denoted as "3-1") of three vortices and one antivortex in the center. These symmetry-induced antivortices can be important not only for superconductors but also for symmetrically confined superfluids and Bose-Einstein condensates. Since the order parameter patterns reported in Refs. [49, 50] have been obtained in the framework of the linearized Ginzburg-Landau (GL) theory, this approach is valid only close to the nucleation line $T_c(H)$. In the limit of an extreme type II superconductor ($\kappa \gg 1$), it has been shown that a configuration of one antivortex in the center and four vortices on the diagonals of the square is unstable away from the phase boundary [66, 67]. Such a vortex state is very sensitive to any distortion of the symmetry and can easily be destroyed by a small defect set to the system [68]. Mertelj and Kabanov found the symmetry-induced solution with an antivortex in a thin-film superconducting square [69], in a broader region of the phase diagram than that in Refs. [49, 50]. Possible scenarios of the penetration of a vortex into a mesoscopic superconducting triangle with increasing magnetic field have been studied in Ref. [70]. While a single vortex enters the triangle through a midpoint of one side, a symmetric ("3-2") combination of three vortices and one antivortex with vorticity $L_{av} = 2$ turns out to be energetically favorable when the vortices are close to the center of the triangle [70]. Misko *et al.* [51] studied the stable vortex-antivortex molecules. Since the interaction between the vortex and antivortex is repulsive in the type-I superconductor, the vortex-antivortex configuration is stable, while in type-II, it is unstable because the sign in the forces of vortex-vortex and vortex-antivortex interaction is changed when passing the dual point $\kappa = 1/\sqrt{2}$, combined with the condensate confinement by the boundaries of the mesoscopic triangle [51]. Those antivortex predicted by the theory [49–51] remain experimentally undetected, mainly because of their high sensitivity to defects in sample edges [68] and extreme vortex proximity [67]. Geurts *et al.* [71] discovered that these fascinating (but experimentally not observed so far) states can be enforced by artificial fourfold pinning, with their diagnostic features enhanced by orders of magnitude. The second-order nucleation of vortex-antivortex molecules can be driven by either temperature or an applied magnetic field, with stable asymmetric vortex-antivortex equilibria found on its path.

Comparing with the disk, the vortex patterns in mesoscopic square and triangle are quite different. Baelus and Peeters [66] compared the vortex state

of superconducting disks, squares, and triangles with the same surface area having nonzero thickness. They found that for given vorticity the vortex lattice is different for the three geometries, i.e., it tries to adjust to the geometry of the sample. For squares and triangles they found magnetic field regions where there is a coexistence between a giant vortex state in the center and several separated vortices in the direction of the sample corners. The research of the mesoscopic superconductor with noncirclar geometries was mainly done within the Ginzburg-Landau theory. The formation of vortices in rectangles in the case when $\kappa \gg 1$ and the external field $H_{c1} < H \ll H_{c2}$, and the London theory gives a good approximation in the multivortex regiume, was done by Sardella *et al.* [15]. They found the free energy with arbitrary vortex configurations in rectangle and mainly discussed the *elongated* rectangles or thin films, where the energy expression takes a relatively simple form.

1.4.2 Vortex states in superconductors with periodic pinning sites

Magnetic and current-carrying properties of superconducting films with nanoengineered arrays of periodic and quasi-periodic pinning sites attract a lot of attention both from the experimental [72–84] and theoretical [85–99] points of view. The main reason of this interest is that the regularity in positions of pinning sites produces a large increase of the critical current at certain values of the magnetic field which correspond to the matching between the number of vortices and the number of pinning sites in the system. The highest value of the critical current in films with periodic pins was obtained for the same concentration of vortices and pinning sites. If the pinning potential is strong enough, vortices in a film with a square array of pinning sites also form a square lattice instead of the triangular one, the latter being energetically favorable in the absence of pinning. This regime corresponds to single-vortex pinning when vortices are pinned individually and the flux-line lattice behaves not as a collective media. However, if the pinning strength becomes of the order of the elastic energy of the flux-line lattice, the vortex-vortex interaction becomes important, and the triangular symmetry of the vortex array is recovered. Thus, at the filling factor 1, low values of the pinning strengths favor a deformed triangular vortex lattice, which is basically depinned from the pinning array. At high values of the pinning strength, the regular square array of pinned vortices is the lowest energy state. There is also an intermediate regime, where the vortex lattice is regular, but half of the vortex rows is depinned and form a lattice with a symmetry close to the triangular one.

Structural phase transitions due to the tuning of the regular pinning strengths were studied theoretically within the framework of the London theory [100–102] where vortices were treated as point-like objects, i.e., near the first critical field. The same regime was considered in Refs. [103, 104] by using molecular dynamics simulations. Ref. [105] analyzes such transitions near

the second critical field using the linearized Ginzburg-Landau theory, whereas in Refs. [95, 96, 106] the whole system of the Ginzburg-Landau equations was solved numerically. There are also applications of the same ideas for the vortex lattices in rotating Bose-Einstein condensates of alkali metal atoms, where regular pinning potential can be formed and easily tuned, in a broad range, by using lasers. At first, structural transitions of vortex lattices in this system were predicted theoretically in Refs. [107, 108] using Gross-Pitaevskii equation and then observed experimentally [109]. The experimental work [110] on elastic lattices of millimeter-size charged particles in a square array of traps exhibit similar physics as the here considered vortex phases. Another example is colloidal particles on periodic substrates [111, 112]. Thus, the problem of the competition between the symmetry of the underlying pinning array and the lattice of repealing particles is important in various fields of modern physics. Note that in the case of superconducting films, holes which are usually used to create regular pins produce a strong pinning potential, which always dominate the vortex-vortex interaction. Weak enough pinning sites can be fabricated, for example, by imposing a periodic modulation on the film surface and were recently studied theoretically in Ref. [106].

The behavior of an elastic media under the competitive action of a regular potential and disorder is a common problem in various fields of modern physics. Examples of such media are vortex lattices in superconductors [72, 92, 94, 96] or in Bose-Einstein condensates of ultracold atoms [109], interacting colloids on periodic substrates [112, 113], charge and spin density waves in metals [31], polarization density waves in ferroelectrics and many others. Regular pinning potential can be either of artificial origin, as in nanostructured superconductors and in Bose-Einstein condensates with optical lattices, or it can be imposed by the crystal structure of the material. In superconductors, pinning efficiency determines the value of the critical current, while the enhancement of this current is of great practical importance. Theoretical description of such systems is a quite complicated problem, which in one-dimensional case can be reduced to the well-known Frenkel-Kontorova model [31, 114]. Numerical simulations supplemented by analytical arguments thus can be considered as an effective approach for understanding of basic properties of systems with both regular and random potentials.

1.4.3 Pattern formation in systems with competing interaction

Pattern formation in a variety of systems is governed by competing interaction [115]. Examples of such systems are: Langmuir monolayers [116, 117], colloids and gels [118–122], ferrofluids [123–126], magnetic garnet thin films, type-I superconductors [127], the pasta phase in neutron stars [128], etc. In general, there is a strong correlation between the pattern formation and the inter-particle interaction. Thus, attraction favors aggregation while repulsion

favors low local densities. This competition between repulsive and attractive interaction leads to very rich morphologies and phases, such as stripes, clusters, bubbles, etc. [129]. Those different patterns were observed in many diverse systems. In ferrofluid systems, rich phases due to the competition between dipolar forces and short-range forces opposing density variations were found experimentally [123] and theoretically [124]. In neutron stars, the competition between the short-range nuclear attraction and the long-range Coulomb repulsion leads to complex pasta phases [128]. Pattern formation was extensively studied in colloidal systems where the colloid-colloid interaction is characterized by the competition of the hardcore excluded volume interaction, on the one hand, and the polarization of the particles, on the other hand. The interaction potential can be further controlled by introducing other contributions to the interaction. As a result, rich configurations, such as clusters, repulsive or attractive glassy states, gels, were found numerically [21–24, 130, 131], analytically [132, 133] and experimentally [119, 121] in colloidal systems with short range attractive interaction. The properties of isolated clusters formed by the short-range attractive and long-range repulsive interaction were recently studied [134]. By controlling the interaction, the growth of the cluster was shown to change from nearly spherical to one-dimensional patterns. The one-dimensional growth of the clusters facilitated the collective packing into columnar or lamellar phases [134]. The columnar and lamellar phases in three dimension were analyzed using molecular dynamics (MD) simulations [135].

Chapter 2

Vortex states in mesoscopic superconducting squares*

As we discussed in Sec. 1.4.1, vortex patterns in Mesoscopic superconductor are determined by the competing between the vortex-vortex interaction and the confinement energy due to the boundary. In contrast to C_{3n}-symmetric (where n is an integer) polygons, squares are *incommensurate* with triangular vortex lattice for *any* applied magnetic field. The vortex-vortex interaction and the effect of boundaries are always competition in mesoscopic squares. Resulting from this interplay: i) the ground state of the vortex system always involves nonzero elastic energy and, as a consequence, ii) there are metastable states with energies close to the ground state (or, in principle, the ground state even could be degenerate). Early studies on vortices in mesoscopic squares were either limited to very small samples with characteristic sizes of the order of ξ (where ξ is the coherence length) which were able to accommodate only few vortices [66], or they focused on the possibility of generation and stability of vortex-antivortex patterns in squares [52, 67, 68]. Here we present a systematic theoretical analysis of vortex configurations in mesoscopic squares [136] and their first direct observation in μm-sized niobium squares using the Bitter decoration technique [136, 137]. To study the formation of vortex patterns and transitions between the ground and metastable states, we analytically solve the London equation using the Green function method and the image technique, and perform molecular dynamics (MD) simulations. To obtain

* This chapter is based on the following publications:
[1] H. J. Zhao, V. R. Misko, F. M. Peeters, V. Oboznov, S. V. Dubonos, and I. V. Grigorieva, Phys. Rev. B **78**, 104517 (2008).
[2] V. R. Misko, H. J. Zhao, F. M. Peeters, V. Oboznov, S. V. Dubonos, and I. V. Grigorieva, Superconductor Science and Technology 22, **034001** (2009).

the stable vortex configurations, we analyze the filling of squares by vortices with increasing applied magnetic field and the formation of vortex "shells", similarly to those observed in disks.

2.1 Theory: The London approach

We consider a strong type-II superconductor (i.e., characterized by the Ginzburg-Landau parameter $\kappa = \lambda/\xi \gg 1$, where λ is the London penetration depth and ξ is the coherence length) with rectangular cross section in the x-y plane. Note that the London approach is applicable also for *weak* type II superconductors in case of thin-film samples with thickness $d \ll \lambda$ where the penetration depth is modified: $\lambda \to \Lambda = \lambda/d^2$, or in case of low vortex densities in rather *large* mesoscopic samples where vortices are well separated and the order parameter is $|\Psi|^2 = 1$ everywhere except at the vortex cores. The latter case corresponds to the experiments with μm-sized niobium squares as described below. In our model the external magnetic field $\mathbf{H}$ is applied normal to the x-y plane, i.e., along the z-axis: $\mathbf{h} = h\mathbf{z}$. We also assume that the vortex cores are straight lines along the z-direction. Then the local magnetic field can be found by solving the London equation (i.e., Eq. (1.15)):

$$-\lambda^2\nabla^2 h + h = \Phi_0 h \sum_{i=1}^{L} \delta(\boldsymbol{r} - \boldsymbol{r}_i), \tag{2.1}$$

where Φ_0 is the flux quantum and $\{\mathbf{r}_i = (x_i, y_i),\, i = 1, \ldots, L\}$ are the positions of L-vortices. If we also neglect the distortion of the external magnetic field due to the sample, i.e., assume that the value of the magnetic field outside the sample near its boundary is equal to the applied field, then the boundary conditions for the magnetic field are:

$$h(\pm a/2, y) = h(x, 0) = h(x, b) = H. \tag{2.2}$$

The geometry of the problem is shown in Fig. 2.1. The Green function method for solving the London equation Eq. (2.1) with the boundary conditions Eq. (2.2) was previously used by Sardella *et al.* [15]. However, they limited themselves to the special case where one of the sides of the rectangle is much larger than the other: $a \gg b$, i.e., *a stripe*. Such an approximation considerably simplifies the problem but the resulting solution missed the generality (the symmetry with respect to the permutation $x \to y$) and thus could not be used in our case of a square: $a = b$. We seek for a solution of Eq. (2.1) with the boundary conditions Eq. (2.2) which is valid for a rectangle with arbitrary aspect ratio a/b. The Green function associating with the boundary problem defined by Eqs. (2.1) and (2.2) must satisfy the following equation:

$$-\lambda^2\nabla^2 G + G = \delta(x - x')\delta(y - y'), \tag{2.3}$$

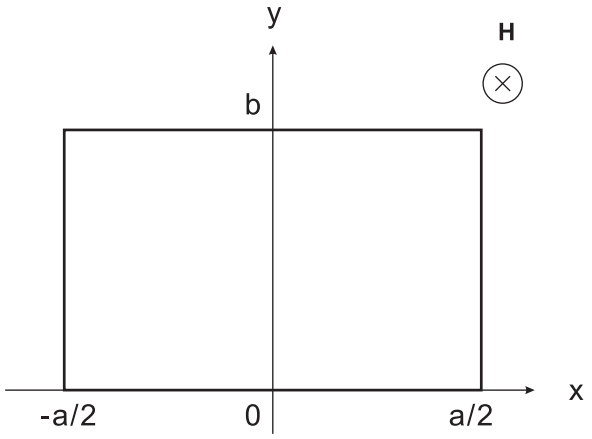

Fig. 2.1 The cross-section of a rectangular superconductor with sides a and b. The external magnetic field $\mathbf{H}$ is applied along the z-axis, and its value is assumed to be constant outside the sample.

and the boundary conditions:

$$G(\pm a/2, y) = G(x, 0) = G(x, b) = 0. \tag{2.4}$$

Multiplying Eq. (2.1) by G and Eq. (2.3) by h and subtract one from another, we obtain

$$\begin{aligned} &-\lambda^2(G\nabla^2 h - h\nabla^2 G) \\ &\quad = G\Phi_0 \sum_{i=1}^{L} \delta(\boldsymbol{r} - \boldsymbol{r}_i) - h\delta(x - x')\delta(y - y'). \end{aligned} \tag{2.5}$$

Integrating Eq. (2.5) over the sample area, we arrive at

$$\begin{aligned} &-\lambda^2 \int_{-a/2}^{a/2} dx \int_0^b dy (G\nabla^2 h - h\nabla^2 G) \\ &\quad = \int_{-a/2}^{a/2} dx \int_0^b dy \big[G\Phi_0 \sum_{i=1}^{L} \delta(\boldsymbol{r} - \boldsymbol{r}_i) - \\ &\qquad h\delta(x - x')\delta(y - y') \big]. \end{aligned} \tag{2.6}$$

Further we use Gauss theorem,

$$\begin{aligned} &-\lambda^2 \int_{-a/2}^{a/2} dx \int_0^b dy (G\nabla^2 h - h\nabla^2 G) \\ &\quad = -\lambda^2 \oint_{boundary} dl \big(G\frac{\partial h}{\partial n} - h\frac{\partial G}{\partial n} \big), \end{aligned}$$

where $\partial/\partial n$ is the derivative in the normal direction to the boundary, and the boundary conditions Eqs. (2.4) and (2.2), and we find the expression for the magnetic field:

$$h(x',y') = H\left[1 - \int_{-a/2}^{a/2} dx \int_0^b dy G(x,y,x',y')\right] + \Phi_0 \sum_{i=1}^{L} G(x_i,y_i,x',y'). \tag{2.7}$$

Therefore, the problem of finding the solution for the local magnetic field is reduced to the determination of the Green function $G(x,y,x',y')$. In order to find a solution to Eq. (2.3) with the boundary condition Eq. (2.4), we expand the Green function in a Fourier series,

$$G(x,y,x',y') = \frac{2}{b}\sum_{m=1}^{\infty} \sin(\frac{m\pi y'}{b}) \sin(\frac{m\pi y}{b}) g_m(x,x'). \tag{2.8}$$

Note that the boundary conditions Eq. (2.4) are satisfied at $y = 0, b$. Further we substitute this expansion into Eq. (2.3) and obtain

$$\begin{aligned} &-\lambda^2 \frac{2}{b}\sum_{m=1}^{\infty}\Big[\frac{\partial^2 g_m(x,x')}{\partial x^2}\sin(\frac{m\pi y'}{b})\sin(\frac{m\pi y}{b}) \\ &-(\frac{m\pi}{b})^2 g_m(x,x')\sin(\frac{m\pi y'}{b})\sin(\frac{m\pi y}{b}) \\ &+\sin(\frac{m\pi y'}{b})\sin(\frac{m\pi y}{b})g_m(x,x')\Big] \\ &= \delta(x-x')\frac{2}{b}\sum_{m=1}^{\infty}\sin(\frac{m\pi y'}{b})\sin(\frac{m\pi y}{b}), \end{aligned} \tag{2.9}$$

where we used the following δ-function representation

$$\delta(y-y') = \frac{2}{b}\sum_{m=1}^{\infty}\sin(\frac{m\pi y'}{b})\sin(\frac{m\pi y}{b})$$

since $\left\{\sqrt{\frac{2}{b}}\sin(\frac{m\pi y}{b}),\ m = 1,2,3\ldots\right\}$ forms a complete set of orthonormal functions. As a result, we obtain the following equation for the Fourier-transform of the Green function $g_m(x,x')$,

$$-\lambda^2\frac{\partial^2 g_m(x,x')}{\partial x^2} + \alpha_m^2 g_m(x,x') = \delta(x-x'). \tag{2.10}$$

Where,

$$\alpha_m = \left[1 + \lambda^2(\frac{m\pi}{b})^2\right]^{1/2}. \tag{2.11}$$

The functions $g_m(x,x')$ must satisfy the boundary conditions $g_m(\pm a/2,x')=0$. In order to solve Eq. (2.10), we first take its Fourier transform,

$$-\lambda^2(i\omega)^2F(\omega)+\alpha_m^2F(\omega)=\frac{1}{2\pi}e^{-i\omega x'},$$

where

$$F(\omega)=\frac{e^{-i\omega x'}}{2\pi(\lambda^2\omega^2+\alpha_m^2)},$$

from which we obtain a particular solution to Eq. (2.10)

$$\begin{aligned}g_m|_{a\to\infty}&=\frac{1}{2\alpha_m\lambda}e^{-\alpha_m|x-x'|/\lambda}\\&=\frac{1}{2\alpha_m\lambda}\big[\cosh(\alpha_m(x-x')/\lambda)-\sinh(\alpha_m|x-x'|\lambda)\big].\end{aligned}$$

The general solution of Eq. (2.10) reads as:

$$\begin{aligned}g_m=&\frac{1}{2\alpha_m\lambda}\big[\cosh(\alpha_m(x-x')/\lambda)-\sinh(\alpha_m|x-x'|\lambda)\big]\\&+A(x')\sinh(\alpha_m x/\lambda)+B(x')\cosh(\alpha_m x/\lambda)\\=&\frac{1}{2\alpha_m\lambda}\big[-\sinh(\alpha_m|x-x'|\lambda)+C(x')\sinh(\alpha_m x/\lambda)\\&+D(x')\cosh(\alpha_m x/\lambda)\big].\end{aligned}$$

Using the boundary conditions Eq. (2.4) we find the coefficients $C(x')$ and $D(x')$:

$$\begin{aligned}C(x')&=-\coth(\alpha_m a/2\lambda)\sinh(x');\\D(x')&=\tanh(\alpha_m a/2\lambda)\cosh(x').\end{aligned}$$

Then the solution for $g_m(x,x')$ is given by

$$\begin{aligned}g_m(x,x')=&\frac{1}{2\lambda\alpha_m\sinh(\alpha_m a/\lambda)}\\&\times\Big\{\cosh\big[\alpha_m(|x-x'|-a)/\lambda\big]\\&-\cosh\big[\alpha_m(x+x')/\lambda\big]\Big\}.\end{aligned}\tag{2.12}$$

Insecting this result into Eq. (2.8), we obtain the expression for the Green function:

$$\begin{aligned}G(x,y,x',y')=&\frac{2}{b}\sum_{m=1}^{\infty}\sin(\frac{m\pi y'}{b})\sin(\frac{m\pi y}{b})\\&\times\frac{1}{2\lambda\alpha_m\sinh(\alpha_m a/\lambda)}\Big\{\cosh\big[\alpha_m(|x-x'|-a)/\lambda\big]\\&-\cosh\big[\alpha_m(x+x')/\lambda\big]\Big\}.\end{aligned}\tag{2.13}$$

From it we obtain an expression for the local magnetic field:

$$\begin{aligned} h(x,y) =&\Phi_0 \sum_{i=1}^{L} G(x_i,y_i,x,y) + H\Bigg\{ \frac{\cosh[(y-b/2)/\lambda]}{\cosh(b/2\lambda)} \\ &+ \frac{4}{b}\sum_{m=0}^{\infty} \frac{b}{\alpha_{2m+1}^2(2m+1)\pi} \sin\left[\frac{(2m+1)\pi y}{b}\right] \\ &\times \frac{\cosh(\alpha_{2m+1}x/\lambda)}{\cosh(\alpha_{2m+1}a/2\lambda)}\Bigg\}. \end{aligned} \tag{2.14}$$

Note that this solution is valid for a rectangle with arbitrary aspect ratio a/b and is a generalization of the earlier result presented in Ref. [15], which was valid for $a/b \gg 1$. Using the obtained solution or the London equation for the local distribution of the magnetic field $h(x,y)$, the Gibbs free energy per unit length of an arbitrary vortex configuration can be find by substituting Eq. (2.14) to Eq. (1.17):

$$\begin{aligned} \mathscr{G} =&\sum_{i=1}^{L}\left(\epsilon_i^{shield} + \sum_{j=1}^{L}\epsilon_{ij}^{v}\right) + \epsilon^{core} + \epsilon^{field} \\ =&\frac{\Phi_0 H}{4\pi A}\sum_{i=1}^{L}\Bigg\{\frac{\cosh[(y_i-b/2)/\lambda]}{\cosh(b/2\lambda)} + \\ &\frac{4}{b}\sum_{m=0}^{\infty}\alpha_{2m+1}^{-2}\frac{b}{(2m+1)\pi}\sin\big[\frac{(2m+1)\pi y_i}{b}\big]\frac{\cosh(\alpha_{2m+1}x_i/\lambda)}{\cosh(\alpha_{2m+1}a/2\lambda)}\Bigg\} \\ &+\frac{\Phi_0^2}{8\pi A}\sum_{i=1}^{L}\sum_{j=1}^{L}G(x_i,y_i,x_j,y_j) \\ &-\frac{H^2}{8\pi}\Bigg\{\frac{\tanh(b/2\lambda)}{b/2\lambda} - \frac{8}{\pi^2}\sum_{m=0}^{\infty}\frac{\tanh(\alpha_{2m+1}a/2\lambda)}{[(2m+1)\alpha_{2m+1}]^2(\alpha_{2m+1}a/2\lambda)}\Bigg\} \\ &-N\frac{\Phi_0 H}{4\pi A}. \end{aligned} \tag{2.15}$$

The last two terms are the energies associated with the external magnetic field and the vortex cores, respectively. The first term represents the interaction between the i^{th} vortex and the shielding currents, Which is proportional to the local magnetic field. Note that in Ref. [15], the authors limited their consideration to the case of a thin film such that $(\pi\lambda/b)^2 \gg 1$ and the term "1" in Eq. (2.11) can be neglected. As we expect, the local magnetic field given by Eq. (2.14) equals the the external magnetic field at the boundary and has the minimal value at center (see Fig. 2.2 (a)). Thus, the shielding currents try to push the vortices inside the square. The London theory has a singularity for the interaction between a vortex and its own image (self-interaction). We notice that when $i = j$ the Green function does not converge. To avoid

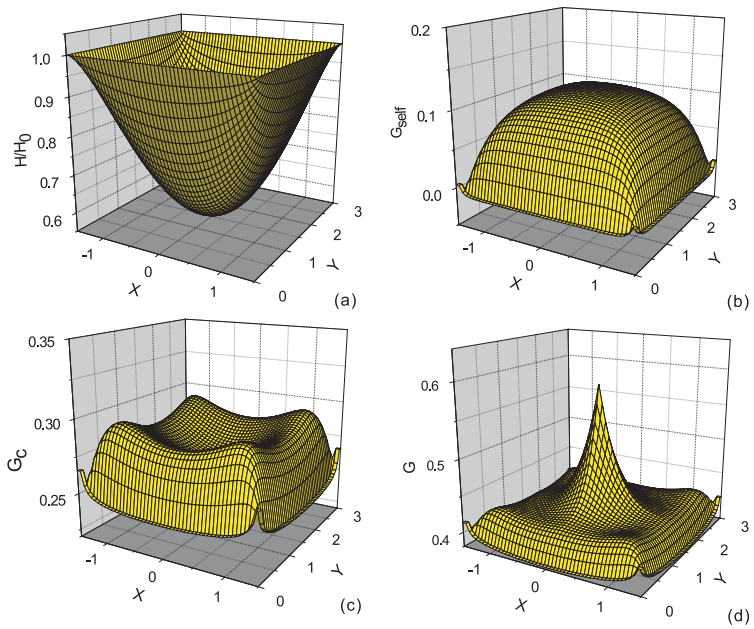

Fig. 2.2 (a) The magnetic field distribution in a superconducting square with the length of the side $a = 3\lambda$. H_0 is the external magnetic field . (b) The self-energy distribution shows the attractive effect of the surface. (c) Confinement energy when the external field $H_0 = 0.023Hc_2$ shows the surface barrier. (d) The free energy distribution when $H_0 = 0.036Hc_2$ and one vortex is located in the center. G(x,y) is equal to the free energy increase by adding a vortex at the point (x, y).

the divergency, we apply a cutoff procedure (see, e.g., Refs. [14, 138, 139]), which means a replacement of $|\mathbf{r}_i - \mathbf{r}_j|$ by $a\xi$ for $i = j$. It was shown in Ref. [140] that the results of the London theory agree with those of the Ginzburg-Landau theory, the vortex size should be chosen as $\sqrt{2}\xi$, and therefore we take $a = \sqrt{2}$. The self-interaction energy $\epsilon_{self} = \epsilon_{ii}$ shows that the boundary attracts the vortices (see Fig. 2.2 (b)). The confinement energy is given by $\epsilon_c = \epsilon_i^{shield} + \epsilon_{ii}$. As shown in Fig. 2.2 (c), the competition between these two terms form the well know surface (Bean-Livingston) barrier. The interaction between the vortices are repulsive. Thus, it costs high energy to put two vortices close to each other (see Fig. 2.2 (d)).

In Figs 2.3(a) and (b), we plot the distribution of the confinement energy for mesoscopic squares with $a = 3\lambda$ and $a = 15\lambda$, correspondingly. In the mesoscopic square with $a = 3\lambda$, Fig. 2.3(a), the screening current extends inside the square and interacts with all the vortices. But in the large mesoscopic square (we call it "macroscopic") with $a = 15\lambda$, only the vortices

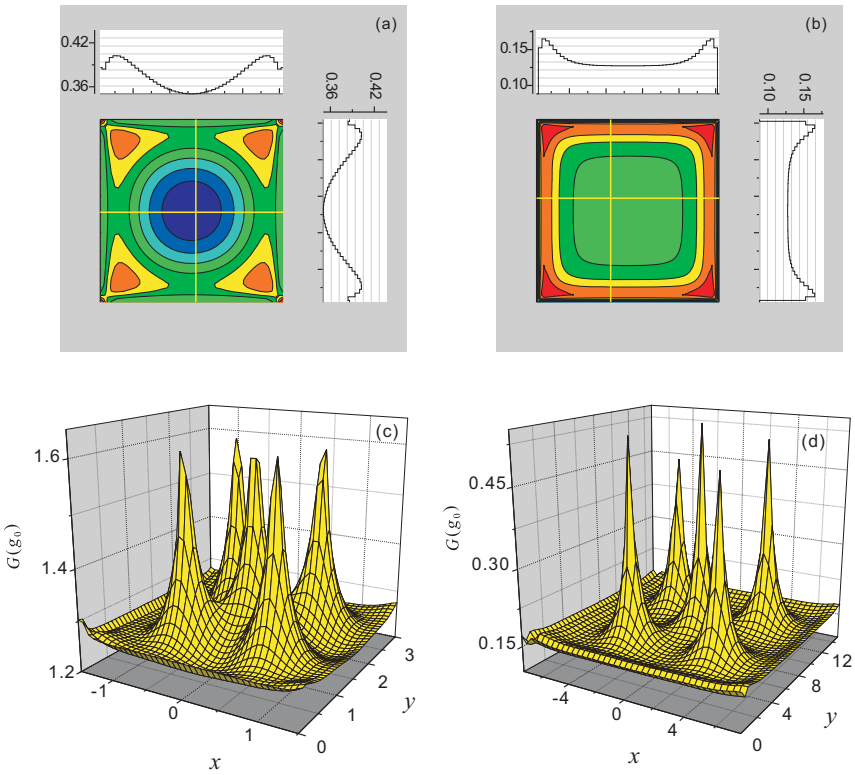

Fig. 2.3 The profiles of the confinement energy (measured in units of $g_0 = \Phi_0^2/8\pi A \cdot 1/\lambda^2$, where A is the area of the sample) for mesoscopic superconducting squares with size $a = 3\lambda$ (a) and 15λ (b). The distributions of the energy in squares with $a = 3\lambda$ (c) and 15λ (d) for the vortex state with $L = 5$.

which are close to the boundary feel the screening current. In the mesoscopic square, vortices strongly overlap with each other (see Fig. 2.3(c)) while in the macroscopic square, the interaction between vortices is rather weak and only the closest neighbors are important (see Fig. 2.3(d)) (see Ref. [46]).

2.2 The evolution of vortex patterns with magnetic field

2.2.1 Molecular dynamics simulations of vortex patterns

Within the London approach, vortices can be treated as point-like "particles", and it is convenient to employ molecular dynamics (MD) for studying the vortex motion driven by external forces (see, e.g., Refs. [46, 57, 85, 90–92, 97–99]), similarly as for a system of classical particles [141]. In the previous section we obtained the analytic expression for the free energy of a system of L vortices as a function of the applied magnetic field, Eq. (2.15). The force felt by the i^{th} vortex can be obtained by taking the derivative of the energy:

$$F_i = -\nabla_i \mathscr{G}. \tag{2.16}$$

where $\nabla_i = \frac{\partial}{\partial x_i}\mathbf{e}_x + \frac{\partial}{\partial y_i}\mathbf{e}_y$ is the two dimensional Laplacian.

The overdamped equation of vortex motion (see Sec. 1.2.6.2) can be presented in the form:

$$\eta \mathbf{v}_i = \mathbf{F}_i = \sum_{j \neq i} \mathbf{F}_{ij} + \mathbf{F}^i_{self} + \mathbf{F}^i_M + \mathbf{F}^i_T. \tag{2.17}$$

where the first three terms are as follows: $\mathbf{F}_{ij}$ is the force due to the repulsive vortex-vortex interaction of the i^{th} vortex with all other vortices, $\mathbf{F}^i_{self}$ is the interaction force with the image, and $\mathbf{F}^i_M$ is the interaction force with the external magnetic field; η is the viscosity, which is set here to unity. Note that Eq. (2.16) contains these three terms (with the free energy defined by Eq. (2.15)), and in Eq. (2.17) we added a thermal stochastic term $\mathbf{F}^i_T$ to simulate the process of annealing in the experiment. This temperature contribution should obey the following conditions:

$$\langle F^T_i(t) \rangle = 0 \tag{2.18}$$

and

$$\langle F^T_i(t) F^T_i(t') \rangle = 2\eta k_B T \delta_{ij} \delta(t - t'). \tag{2.19}$$

It is convenient to express the lengths in units of λ, the fields in units of H_{c2}, the energies per unit length in units of $g_0 = \Phi_0^2/8\pi A \cdot 1/\lambda^2$, and the force per unit length in units of $f_0 = \Phi_0^2/8\pi A \cdot 1/\lambda^3$, where A is the sample's area. In our calculations we use the value of the Ginzburg-Landau parameter $\kappa = 6$ taken from the experiment with Nb (see below).

In order to find the ground state vortex configurations in squares, we perform stimulated annealing simulations (SAS) by numerically integrating the overdamped equations of motion Eq. (2.17). The procedure is as follows.

First we generate a random vortex distribution and set a high value of temperature. Then we gradually decrease the temperature to zero, i.e., simulating the annealing process in the experiments (see, e.g., Ref. [142]). To find the minimum energy configuration , we perform many simulation runs with random initial distributions and count the statistics of appearance of different vortex configurations for each L. This procedure simulates [46] the statistical analysis of experimental data with simultaneous measurements of vortex configurations in arrays of *many* (up to 300) practically identical samples. It was used in experiments with Nb disks in Refs. [47, 57] and also in experiments with Nb squares presented in this section.

2.2.2 Filling rules for vortices in squares with increasing magnetic field: Formation of vortex shells

The results for the vortex patterns for different vorticities L are shown in Figs 2.4 and 2.5. With increasing applied magnetic field, vortex configurations evolve as follows: starting from a Meissner state with no vortex, first one vortex appears in the center Fig. 2.4(a), then two are located symmetrically on the diagonal Fig. 2.4(b). Further increase of the magnetic field leads to the formation of a triangular vortex pattern. Fig. 2.4(c) having a common symmetry axis with the square, which is the diagonal. For $L = 4$ vortices arrange themselves in a perfect square, Fig. 2.4(d) whose symmetry is commensurate with the sample and therefore it turns out that this is a highly stable vortex configuration [143]. Note that even in bulk the gain in the elastic energy is very small during the transition from the triangular vortex lattice to the square one, and consequently, in the presence of a square boundary, it turns out that the square vortex lattice can be easily stabilized (for commensurate vortex numbers). For vorticity $L = 5$, vortices tend to form either a pentagon, or a square with one vortex in the center (see Fig. 2.4(e), the transition between this configuration and the pentagon-like pattern will be discussed below). The additional vortex appears in the center thus forming a second *shell* in a similar way as in disks [45–47], but in the later, this occurred for larger L-value. To distinguish different shells and indicate the number of vortices in each shell, we use the notations as in Refs. [45–47]. For example, the pentagon-like configuration and the pattern with four vortices in the outershell and one vortex in the center are denoted as (5) and $(1, 4)$, respectively. (It is clear that vortex shells in squares are not as well defined as in disks and sometimes it is a matter of choice how to define them.) Compared with disks, which have C_∞ symmetry, the C_4 symmetry of squares induces a new element of symmetry in the resulting vortex patterns. In other words, vortex patterns in squares (tend to) acquire elements of the C_4 symmetry even if they are not arranged in a perfect square lattice. For example, the calculated vortex patterns share one ($L = 6$, Fig. 2.4(f)) or two

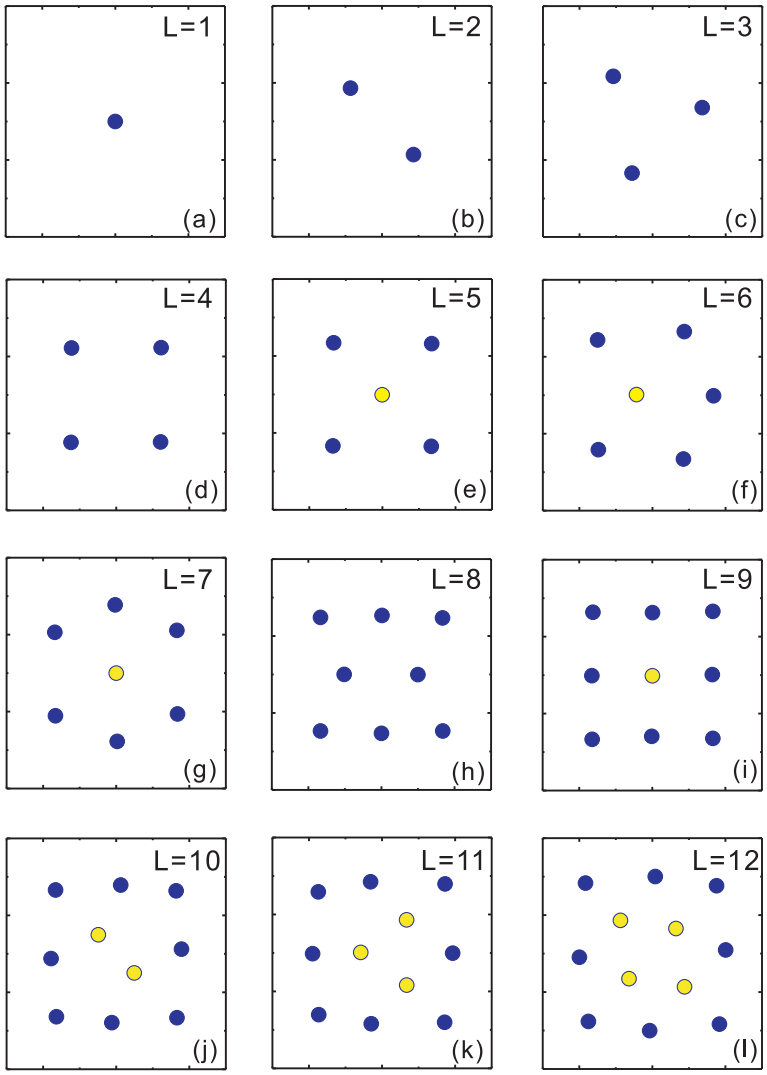

Fig. 2.4 The evolution of vortex configurations for the states with vorticity increasing from $L = 1$ to 12, in a superconducting square with $a = 3\lambda$. The vortices in the outer shell are shown by the blue (black) circles while the inner-shell vortices are shown by the yellow (grey) circles. The formation of the second shell starts when $L = 5$.

($L = 7$ and 8, Figs. 2.4(g) and (h), correspondingly) symmetry axes of the square parallel to its side. This tendency to share symmetry elements with the square boundary remains also for larger vorticities as can be seen, e.g., in Figs. 2.4(j), (k), and (l) for vorticities $L = 10$, 11, and 12, respectively. For the commensurate number of vortices $L = 9$, a perfect symmetric square-lattice pattern is formed.

Using the concept of vortex shells, we analyzed the filling rules for mesoscopic superconducting squares with increasing magnetic field. To summarize these rules, for $L = 1$ to 4, vortices are arranged in a single "shell"; the second shell appears when $L = 5$, and then vortices fill the shells as follows: As the vorticity L increases from $L = 5$ to 9, the new vortices fill the outer shell. Then the number of vortices in the inner shell starts to increase for $L \geq 9$ (see Figs. 2.4(j), (k), and (l)). This occurs because the outer shell is formed by 8 vortices (i.e., three per each side) which turns out to be stable. Thus, the new vortices fill the inner shell until $L = 12$. Then, again, the newly generated vortices start to fill the outermost shell until $L = 16$, when the number of vortices in the outermost shell becomes 12, which is also stable (i.e., commensurate with the square boundary). The formation of the third shell starts when the vorticity becomes $L = 17$ (note that for $L = 17$ the vortices can arrange themselves either in a two-shell configuration (5,12), or in a three-shell configuration (1,4,12) which occurs to have a slightly lower energy, see analysis below). In a similar way, the filling of shells occurs for larger values of L (e.g., for 3-, 4-shell patterns, etc.). As a general rule, the outermost shells containing $4N$ vortices, where N is an integer, are very stable. With increasing the density of vortices, the average distance between them decreases. As a result, the interaction between vortices becomes more and more important leading to the formation of the triangular-lattice phase away from the boundary. Therefore, the triangular lattice is recovered for large vorticities being distorted near the square boundaries. Note that for large enough L vortices do not form a square lattice even for commensurate vortex numbers (e.g., for $L = 25$, 36, etc.) as it does for $L = 4$, 9, and 16. Some expamples of two- and three-shell vortex patterns are shown in Fig. 2.5. The vortex states for $L = 1 \sim 30$ are summarized in table 2.1.

2.2.3 The influence of sample deformation

In order to study the influence of the symmetry, we slightly deformed the square [137]. We change the square to a rectangle, by reducing the length in y direction b to 2.8λ. Since the diagonal lines are no longer the symmetry axis, the configurations such as (2), (5), (2,10), (4,8), (5,12), which used to take the diagonal lines as their symmetry axis, are strongly deformed (see Fig. 2.6). The vortices used to locate on the diagonal lines (except the ones in the center) are moved to form lines that are parallel to the boundary with other vortices. The state (4,8) is disappeared, since both the two diagonal lines are its symmetry axis. Other states that have the other two symmetry axis of the

L	states	L	states	L	states
1	(1)	11	(3,8)	21	$(1,5,15)^d$
2	(2)	12	(4,8),(2,10)	22	$(4,4,14)^d$
3	(3)	13	(4,9),(2,11)	23	(1,6,16)
4	(4)	14	(3,11),(4,10)	24	(1,7,16)
5	(1,4),(5)	15	(3,12)	25	(1,8,16)
6	(1,5)	16	(4,12)	26	(1,8,17)
7	(1,6)	17	(5,12),(1,4,12)	27	$(2,8,17)^d$
8	(1,7)	18	(4,14)	28	$(2,9,17)^d$
9	(2,7)	19	(1,4,14)	29	$(3,8,18)^d$
10	(2,8)	20	(1,5,14),(4,4,12)	30	$(3,8,19)^d$

Table 2.1 Filling of the "shells" in vortex configurations for different L in squares. Note that in squares the "shells" are not as well defined as in disks. In some cases square-shaped "shells" can be easily distinguished, but in some cases the distributions look rather as a distorted vortex lattice (we denote such unclear cases with ^{d}) (*After Ref.* [137]).

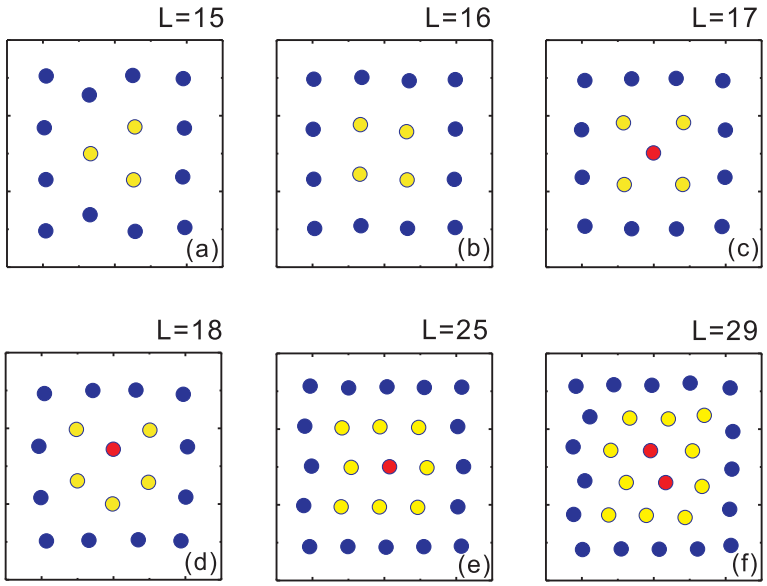

Fig. 2.5 The evolution of vortex configurations for $L = 15$ to 18 (a)-(d), and for $L = 25$ (e) to 29 (f), in a superconducting square with $a = 3\lambda$. The meaning of the colored dots is the same as that in Fig. 2.4. For vorticities $L = 15$ to 18 ((a)-(d)), the outermost shell formed by 12 vortices is complete (commensurate with the square boundary), and with increasing magnetic field vortices fill inner shells. Note that when the inner shell also becomes complete ($L = 16$, state (4,12) (b)), the third shell starts to form for $L = 17$ (c). For states with larger vorticities, e.g., $L = 25$ (e) $L = 29$ (f), the vortex patterns are very close to a triangular lattice which is distorted near the boundary.

square are relatively stable, because the symmetry did not change during the deformation. For $L = 16$, the square lattices are deformed to form triangular lattices.

As we change the size of the square, The observed states are stable. But the possibility to find the different states for the same vorticity is different, i.e. for $L = 12$, it is much easier to get the state (2,10) when we increase the size of square from 3λ to 10λ.

2.2.4 The ground state and metastable states

The incommensurability of the square boundary with the triangular vortex lattice creates metastable vortex configurations. While in many cases metastable states are well separated in energy from the ground state, in some cases, namely, for borderline configurations having n and $n + 1$ shells, the lowest-energy metastable state can become almost indistinguishable from the ground state. In such cases, vortex states with very close energies can have comparable probability to be realized experimentally. An example of a such state is the case $L = 5$. The stable states for $L = 5$ are shown in the insets of Fig. 2.7. In order to examine which one is more stable, we investigate the free energy as a function of the displacement of one of the vortices while we allow the other vortices to relax to their lowest-energy positions. We start with the pentagon-like configuration (5) (the left inset) and we change the position of this vortex moving it towards the center of the square and let the other vortices adjust their positions accordingly. At the end, we arrive at the square-symmetric state (1,4). We plot the free energy of the system as a function of the displacement of this vortex from its equilibrium position, and we repeat this procedure for all the vortices A, B, C, D, and E (we always move only one vortex while all others relax to minimize the free energy). For any of the five vortices, this procedure leads to a barrier between the two states. We notice that there are two possible pentagon-like configurations (5) which share different symmetry axes with the square, see Figs. 2.7(a) and (b). The difference of their free energy is less than 10^{-4}. In Fig. 2.7(a) we see that the motion of vortex C is accompanied with the lowest energy barrier. This is because vortices A, B, D and E are already close to their final positions in state (1,4). Moving vortices B or D lead to a higher energy barrier. Finally, moving vortex A or E to the center is associated with the highest barrier and passing over a saddle point (jump in $G - G_0$). Then we move the central vortex of state (1,4) back to its initial positions in state (5). The highest-barrier transitions (i.e., curves A and E) show a hysteretic behaviour which is an indication of metastable states.

In Fig. 2.7(b), we show the results of the calculation of the free energy as a function of the displacement of a vortex, for a different modification of the state (5), i.e., when the vortex configuration has the symmetry axis coinciding with the diagonal of the square (cp. Fig. 2.7(a)). Note that these two configurations of state (5) have practically *the same* free energy and thus

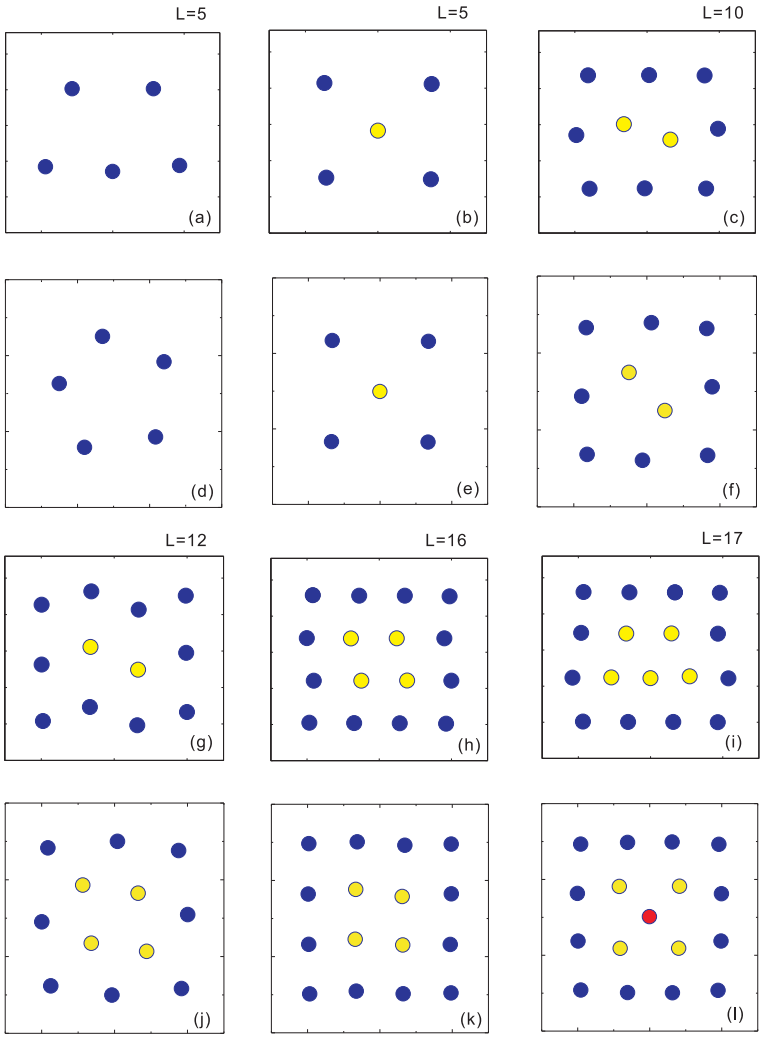

Fig. 2.6 The vortex states in deformed and perfect squares. The meaning of the colored dots is the same as that in Fig. 2.4. (a), (b), (c), (g), (h) and (i) show the vortex configurations in a deformed square with the horizontal length $a = 3\lambda$ and vertical length $b = 2.8\lambda$. (d), (e), (f), (j), (k) and (l) show the vortex configurations in a perfect square with $a = b = 3\lambda$. The corresponding vorticities L are given on top of the deformed squares.

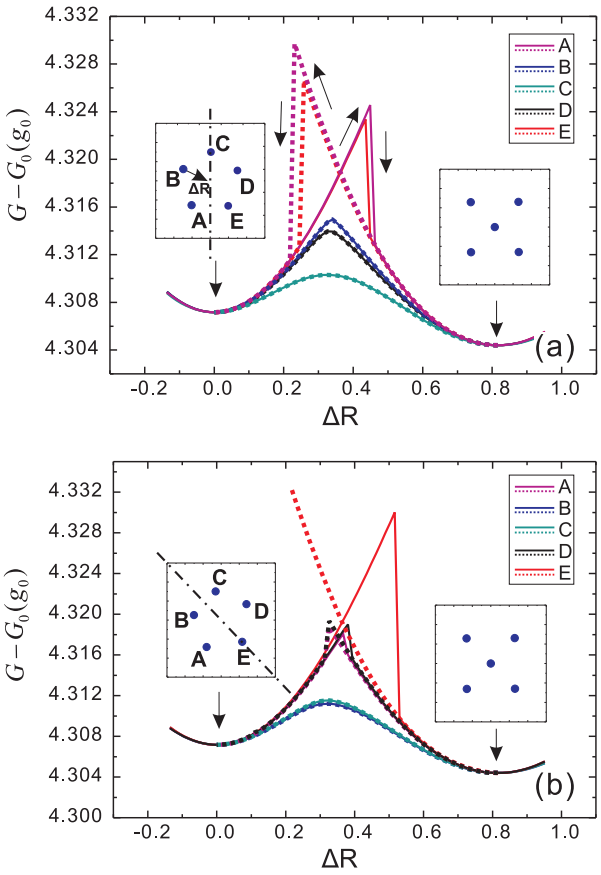

Fig. 2.7 The change of the free energy $(G - G_0)$ versus the displacement R of one of the vortices in the initial pentagon-shaped configuration from its initial position towards the center (two different lines for each configuration correspond to increasing and decreasing ΔR as shown by the arrows in (a)). G_0 is the free energy associated with external magnetic field and the vortex cores (term "4" in Eq. (2.15)), which is independent of the positions of the vortices. The two stable states, the pentagon-like state (5) and the square symmetric state (1,4), are shown in the insets. The vortices are labeled by A, B, C, D and E. Two different symmetry axes of the configuration (5) are shown by the dash-dotted line in the insets of (a) and (b), respectively. The side of the square is $a = 3\lambda$. In both cases, the configuration with one vortex in the center (1,4) has a lower energy than the pentagon-like pattern (5). Note that the curves for B and D (and for A and E) are slightly different due to the fact that the configuration (5) is not perfectly aligned with respect to the symmetry axes.

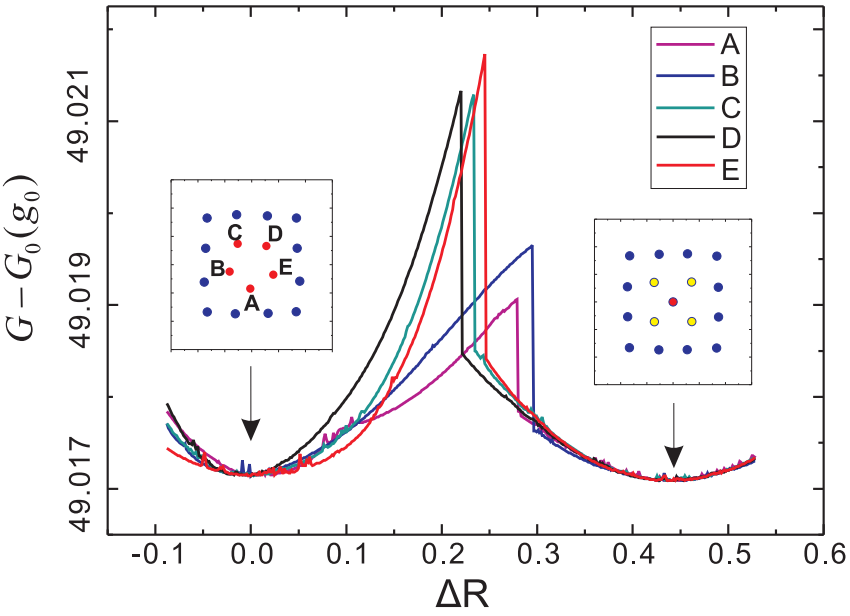

Fig. 2.8 The change of the free energy $(G - G_0)$ versus the displacement R of one of the vortex in the inner shell of the state (5,12) from its initial position towards the center; G_0 is defined in the caption of Fig. 2.7. The change in the free energy due to the movement of the vortices in the inner shells (i.e., (5,12) $\rightarrow$ (1,4,12)) is damped by the movement of the vortices in the outermost shell which act as a "softer" wall than the boundary (in the case of the transition (5) $\rightarrow$ (1,4), see Fig. 2.7). The movement of the vortices in the outmost shell causes more saddle points. The two states, (5,12) and (1,4,12), have very close free energies.

equal probability to appear in experiment. Moving vortex E, which is situated on the diagonal of the square (see the left inset in Fig. 2.7(b)), is accompanied by the highest energy barrier compared to moving other vortices. The reverse process (i.e., moving the central vortex to position E) leads to a very high potential barrier, and the pentagon-like state cannot be restored unless a random (thermal) force is added to break the symmetry. Moving vortex B or C is accompanied by the lowest energy barrier. State (1,4) has a lower free energy than state (5). According to our calculations, it is the ground state for $L = 5$.

Similar transitions are found between two- and three-shell vortex configuration for $L = 17$ (see Fig. 2.8). Twelve vortices form the outermost shell and the other five can form either a one-shell or two-shell configurations similarly as state $L = 5$. Again, we move one of the five vortices in the inner shell of the state (5,12) to the center of the square. The analysis of the free energy shows that the difference of the free energy between the two states ($|\triangle G| \sim 10^{-5}$) is much smaller compared to the states for $L = 5$ ($|\triangle G| \sim 10^{-3}$). The reason for this is that for $L = 17$, the twelve vortices in the outermost shell can adjust themselves to lower the free energy, which create much "softer" walls for the five vortices in the inner shell than the sample boundary. Thus, the change of the free energy due to the movement of the vortices in the inner shells can be more or less compensated by the movement of the vortices in the outermost shell.

For $L = 13$, we move the vortex shown by the yellow (gray) circle in the left inset of Fig. 2.9 towards the center. Instead of artificially change the exact position of a particular vortex, we only change its x-component and its coordinates in y direction as well as the coordinates of the other vortices are determined by minimizing the free energy [137]. As shown in Fig. 2.9, the state (4,9) has lower free energy, which is the ground state. A relatively small barrier is existed between this two states.

2.3 Experimental observation of vortex configurations in mesoscopic Nb squares*

To visualise the corresponding vortex configurations experimentally we used the well-known Bitter decoration technique which is based on *in situ* evaporation of $10 - 20$ nm Fe particles that are attracted to regions of magnetic field created by individual vortices and thus allow their visualisation (details of the technique are described in Sec. 1.3). The mesoscopic samples for this study

* The experiments were performed at the University of Manchester (UK) by I. V. Grigorieva, in collaboration with V. Oboznov and S. V. Dubonos from the Institute of Solid State Physics in Chernogolovka (Russia).

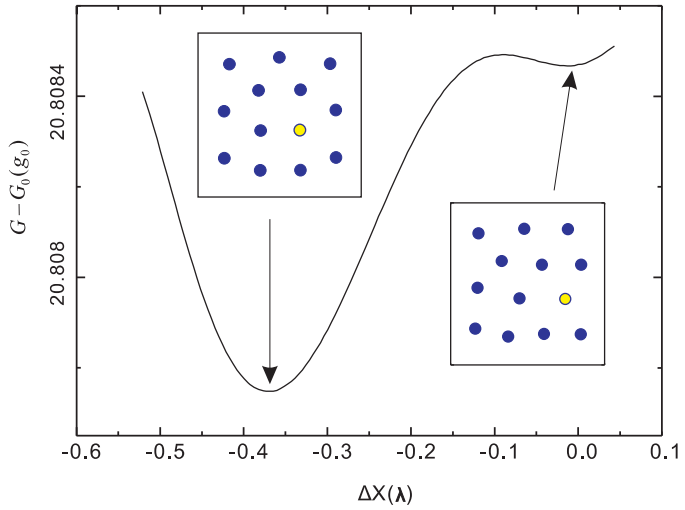

Fig. 2.9 The change of the free energy $(G - G_0)$ versus the x-component of the displacement X of the vortex (the yellow (gray) circle) in the outermost shell of the state (2,11) from its initial position towards the center; G_0 is the free energy associated with external magnetic field and the vortex cores (term "4" in Eq. (2.15)), which is independent of the positions of the vortices. The side of the square is $a = 3\lambda$. The two stable states (2,11) and (4,9) are shown in the insets. The state (4,9) has lower free energy than the state (2,11).

were made from a 150 nm thick Nb film deposited on a Si substrate using magnetron sputtering. The film's superconducting parameters were: transition temperature $T_c = 9.1$ K, magnetic field penetration depth $\lambda(0) \approx 90$ nm; coherence length $\xi(0) \approx 15$ nm; upper critical field $H_{c2}(0) \approx 1.5$ T. Using e-beam lithography and dry etching with an Ar ion beam through a 250 nm thick Al mask, the films were made into arrays of small square "dots" of 4 different sizes, with the side of the square, a, varying from 1 to 5 μm. Each array typically contained 150 to 200 such dots. A whole array was decorated in each experiment, allowing us to obtain a snapshot of up to 100 vortex configurations in dots of the same shape and size, produced in identical conditions (same applied magnetic field H and temperature T, same decoration conditions). It was therefore possible to simultaneously visualise vortex configurations for several different vorticities L (in samples of different sizes) and also to gain enough statistics for quantitative analysis of the observed vortex states in terms of their stability, sensitivity to sample imperfections, and so on. Below we present the results obtained after field-cooling to $T \approx 1.8$ K in perpendicular external fields ranging from $H = 20$ to 60 Oe. We note that the above temperature (1.8 K) represents the starting temperature for the experiments. Thermal evaporation of Fe particles usually leads to a tempo-

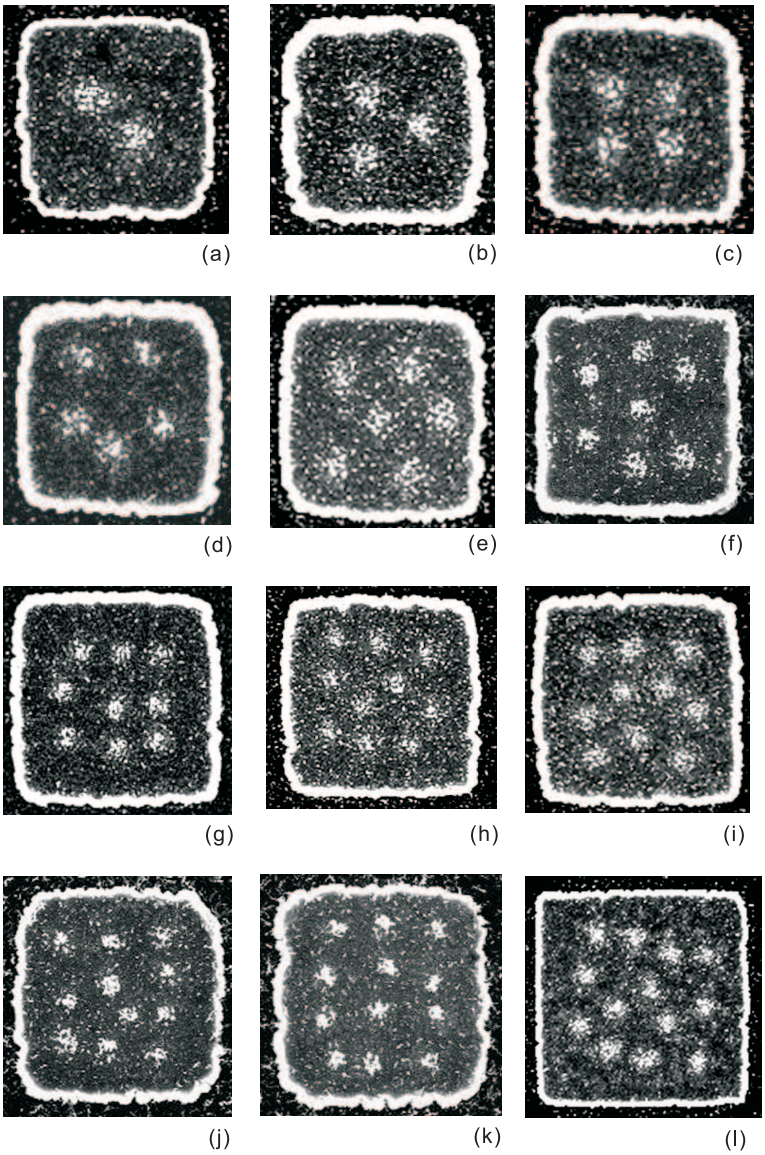

Fig. 2.10 Scanning electron microscope (SEM) images of vortex configurations observed experimentally for vorticities $L = 2$ to 13. Vortex positions are indicated by clusters of small white (Fe) particles. (a) $L = 2$; sample size (side of the square) $a \approx 2.5$ μm, $H = 20$ Oe; (b) $L = 3$; $a \approx 2$ μm, $H = 35$ Oe; (c) $L = 4$; $a \approx 2.4$ μm, $H = 40$ Oe; (d) $L = 5$; $a \approx 2.4$ μm, $H = 40$ Oe; (e) $L = 6$; $a \approx 2.5$ μm, $H = 40$ Oe; (f) $L = 7$; $a \approx 2$ μm, $H = 60$ Oe; (g) $L = 9$; $a \approx 3.5$ μm, $H = 35$ Oe; (h) $L = 10$; $a \approx 3.5$ μm, $H = 35$ Oe; (i) $L = 10$; $a \approx 3.5$ μm, $H = 35$ Oe; (j) $L = 11$; $a \approx 2.5$ μm, $H = 60$ Oe; (k) $L = 12$; $a \approx 2.6$ μm, $H = 60$ Oe; (l) $L = 13$; $a \approx 5$ μm, $H = 20$ Oe.

rary increase in temperature of the decorated samples but the increase never exceeded 2 K in the present experiments, leaving the studied Nb dots in the low-temperature limit, $T < 0.5\ T_c$.

Fig. 2.10 shows examples of vortex configurations observed for vorticities $L = 2$ to 13. The images shown in Fig. 2.10 were obtained in several different experiments and on samples of different sizes (see figure caption). We note that the same vorticity L could be obtained for different combinations of the applied field and the size of the square, e.g., $L = 6$ was found for $H = 60$ Oe, $a = 2$ μm and $H = 40$ Oe, $a = 2.5$ μm, see images in Figs. 2.11(b) and 2.10(e), respectively. Sometimes two different vorticities were found in the same experiment for nominally identical squares, e.g., both $L = 9$ and $L = 10$ were found for $H = 35$ Oe and $a = 3.5$ μm (see images in Figs. 2.10(g), (h), (i)). The latter finding can be explained by slightly different shapes of individual squares or by an extra vortex captured during field cooling (see Ref. [47] for a more detailed discussion), where the same effect was found for circular mesoscopic disks. Overall, the vorticity as a function of the applied field H showed the same behaviour as that found earlier for circular disks [47], i.e., the square dots showed strong diamagnetic response for small vorticities $L < 10$ (also observed earlier in disks with a strong disorder [57]) while for larger vorticities the extra demagnetisation per vortex saturated at $\delta\Phi/\Phi \approx 0.2$, in excellent agreement with earlier numerical studies [66].

Most of the vortex configurations shown in Fig. 2.10 represent just one of several possible states for each vorticity (with the exception of images (h) and (i) which both correspond to $L = 10$). Indeed, for most vorticities we found more than one well-defined vortex configuration and some of these were found with almost the same probability, indicating that, in agreement with theory described above, vortices in mesoscopic squares form not only the ground, but also metastable states, and the energies of the latter are often very close to the energy of the ground state. This conclusion follows from our statistical analysis of all observed vortex configurations which resulted in histograms such as those shown in Fig. 2.11 for $L = 2$, 4, 5, and 6. For $L = 2$ and 4, the most frequently observed states agree with the ground states found theoretically (see Fig. 2.4(b), (d)) and the metastable states appear to have similar energies, as they are found with similar probabilities. As expected, both states for $L = 2$ and two of the states for $L = 4$ have vortices sitting along the symmetry axes of the square, with the diagonal axis being slightly preferable. The third state for $L = 4$ (on the right-hand side in Fig. 2.11(a)) is more unusual in that the vortices are sitting in the apexes of a rhombus that is slightly rotated with respect to the diagonal of the square. Although this particular state did not come out in the numerical simulations [144], it was found with a high probability in experiment and, moreover, the rhombus-based vortex configurations were also found for larger vorticities both in experiment (see, e.g., Fig. 2.10(l) for $L = 13$) and theory (see rhombic inner shells for $L = 12$ and 16 in Figs. 2.4(l) and 2.5(b), respectively).

For $L = 6$, one of the two most frequently observed states (also shown in Fig. 2.10(e)) corresponds exactly to the ground state found numerically (Fig. 2.4(f)) but the state found in experiment with the highest probability is the more symmetric two-shell configuration with the outer shell having the same pentagon shape as that found for $L = 5$. This $L = 6$ state can be viewed as a direct precursor of the two-shell states for $L = 7$ and 9, which were found as ground states both in theory (Fig. 2.4(g),(i)) and experiment (Fig. 2.10(f),(g)). For $L = 5$, two possible states – a two-shell configuration with one vortex in the center (1,4) and four vortices in the corners and a pentagon-like configuration (5) – were found in experiment and in numerical simulations. However, numerical simulations found a slightly lower energy for the two-shell configuration (1,4) (see Fig. 2.7), while in experiment the pentagon-shaped configuration was found to appear more frequently. This discrepancy is unlikely to be related to the non-ideal character of the experimental squares: As we show below, neither the roughness of the boundaries, nor the presence of some pinning in the experimental samples have any noticeable effect on the observed vortex configurations, due to strong confinement (see, e.g., Fig. 2.3). It is possible that, due to the very small difference in free energies between the two states (which becomes practically negligible for samples with $a \gg \lambda$), the vortex configurations for $L = 5$ are particularly sensitive to the exact sample size (in experiment the squares are almost 10 times larger than in the analysis of Fig. 2.7). The sensitivity of vortex configurations to sample size was studied in detail for circular disks (see Ref. [46]) and was indeed found to affect the stability of some (but not all) vortex states. For higher vorticities, $L = 7$ to 13, we found well defined two-shell configurations most of which correspond to the stable configurations found numerically. The outer shell in these configurations was either square (see Figs. 2.10(g)-(k) for $L = 9$ to 12), circular ($L = 7$, Fig. 2.10(f)) or rhombic ($L = 13$, Fig. 2.10(l)) with vortices of the inner shell either sitting along one of the symmetry axes of the square, as for $L = 2$, or forming a triangle, as for $L = 3$. For certain matching vorticities ($L = 9$ and 12), the observed two-shell configurations correspond to a square vortex lattice.

We note that the irregularities of the sample shape and uneven boundaries of some of our dots have, surprisingly, no discernable effect on the observed configurations of vortices (i.e., the vortices form regular, symmetric patterns). For example, the dots in Figs. 2.10(j),(k) have especially rounded corners and very rough boundaries but the vortex configurations have square symmetries. Similarly, the same $L = 6$ state was found in dots with rounded corners, as in Fig. 2.10(e), and in almost perfect squares, as in the image shown in Fig. 2.11(b). Furthermore, we found that for a given value of L the observed configurations did not depend on the sample size or the applied field, at least within the studied field range (see Fig. 2.12 for an example).

Finally, we compared the experimentally observed positions of vortices within the square dots with those found numerically and found an excellent agreement, as demonstrated by Fig. 2.12. Here we show a superposition of

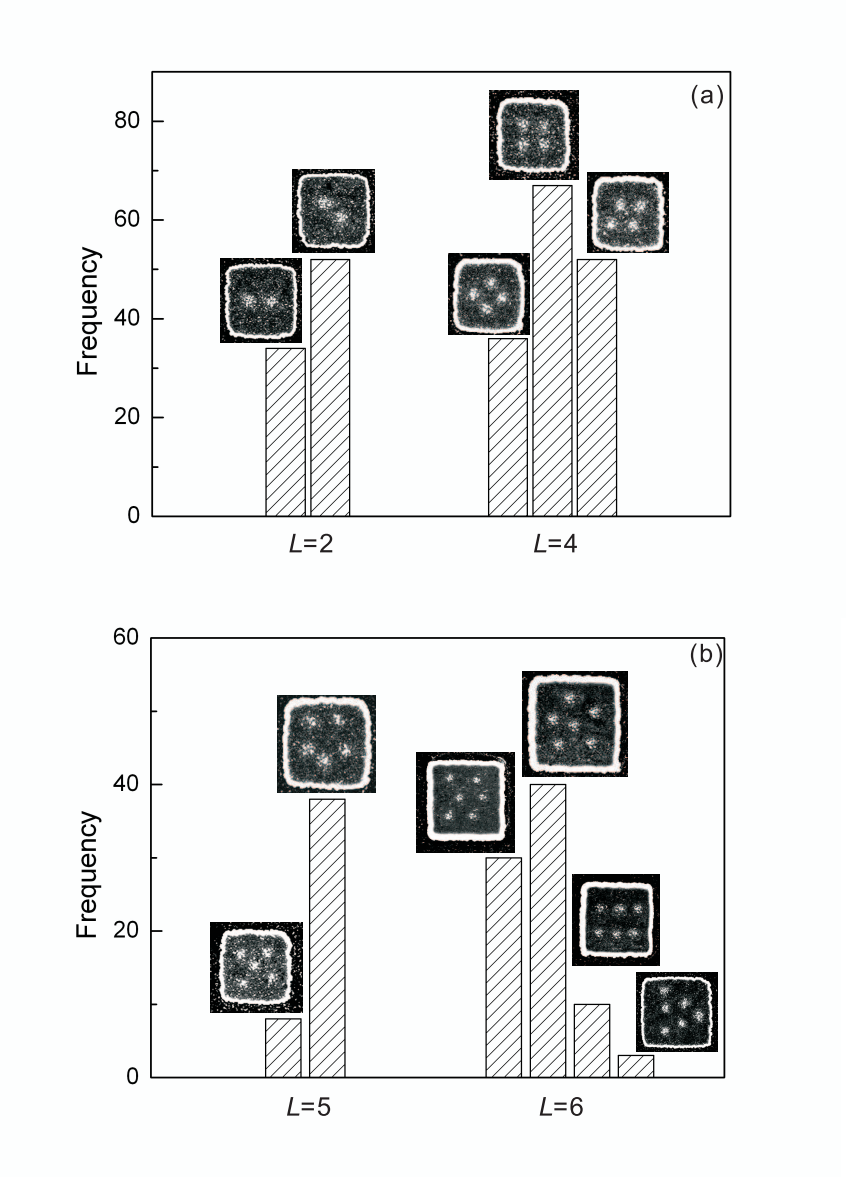

Fig. 2.11 Histograms of different vortex states observed for vortcities $L = 2$, 4 (for squares with $a = 2\mu m$) (a) and $L = 5$ (for squares with $a = 2\mu m$) and 6 (b) ($a = 2\mu m$ and $a = 2.5\mu m$). SEM images of the corresponding vortex configurations are shown as insets.

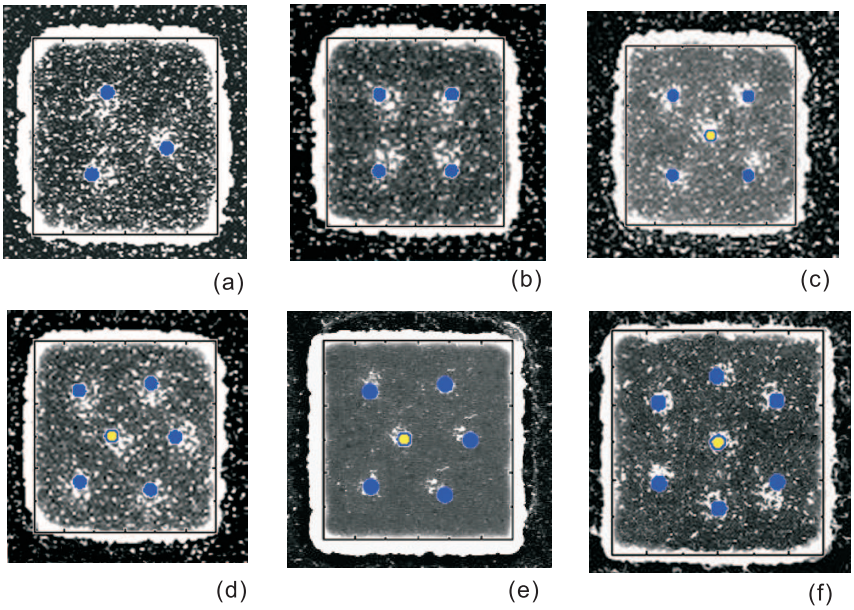

Fig. 2.12 Comparison of the experimentally observed positions of vortices within the square dots with those found numerically (colored dots). Superimposed on the experimental images are vortex configurations shown in Figs. 2.4(c),(d),(e),(f),(g). Two experimental images for $L = 6$ ((d) and (e)) are superimposed on the same theoretical image (Fig. 2.4(f)), to demonstrate that the observed configurations did not depend on the sample size or the applied field (for image (d) $H = 40$ Oe, $a \approx 2.5$ μm, for image (e) $H = 60$ Oe, $a \approx 2$ μm).

theoretical images from Fig. 2.4 and experimental images for the same vortex configurations. Two of the images (Figs. 2.12(d),(e)) compare the same theoretical configuration with experimental images obtained on dots of different sizes in different applied fields ($H = 40$ Oe, $a = 2.5$ μm and $H = 60$ Oe and $a = 2$ μm, respectively) illustrating the point made above that the vortex configurations do not depend on the sample size and/or applied field.

Overall, despite the inevitable presence of some disorder in our samples, which was not taken into account in the calculations, there is a very good agreement between the observed vortex configurations and the calculated vortex patterns. The main features of the vortex states revealed by experiment is formation of vortex shells with predominantly square symmetry for vorticities $L \geq 7$ and vortex patterns following the main symmetry axes of the square for small vorticities $L \leq 4$. The two intermediate vorticities $L = 5$ and 6 appear to be a special case: Here the mismatch between the square shape of the dot and the natural symmetry of the vortex lattice is more difficult to accommodate and the preferred vortex configurations turned out to be the pentagon-shaped shell for $L = 5$ and three different patterns for $L = 6$, none of which has the four-fold symmetry of the square.

In conclusion, we performed a systematic study of vortex configurations in mesoscopic superconducting squares and compared the results with vortex patterns observed experimentally in μm-sized Nb squares using the Bitter decoration technique.

In the theoretical analysis we relied upon the analytical solution of the London equation in mesoscopic squares by using the Green function method and the image technique. The stable vortex configurations were calculated using the technique of molecular dynamics simulations simulating the stimulated annealing process in experiments.

We revealed the filling rules for squares with growing number of vortices L when gradually increasing the applied magnetic field. In particular, we found that for small L vortices tend to form patterns that are commensurate with the symmetry of the square boundaries of the sample. The filling of "shells" (similar to mesoscopic disks) occurs by periodic filling of the outermost and internal shells. With increasing vorticity, the outermost shell is filled until it is complete (i.e., the number of vortices in it becomes $4N$, where N is an integer, i.e., commensurate with the square boundary). Then vortices fill internal shells untill the number of vortices becomes large enough to create the outermost shell with $4(N + 1)$ vortices. Again, after that vortices fill internal shells. With increasing vorticity, the shell structure becomes less pronounced, and for large enough L the vortex patterns in squares becomes a traingular lattice distorted near the boundaries.

Chapter 3

Vortex configurations in mesoscopic superconducting triangles*

Triangles stand apart from mesoscopic superconductors of other geometries. An equilateral triangle has the same symmetry as the Abrikosov vortex lattice. This means that for certain (e.g., *commensurate*) number of vortices, a triangle can accommodate a piece of the vortex lattice without any distortion. As a result, such vortex patterns occur to be much more stable because both the vortex-vortex interaction and the effect of boundaries favour the stability of triangular vortex patterns. Strikingly, it turns out that if one of the vortices in a commensurate set is missing (i.e., the applied flux is insufficient to generate it), the symmetric vortex configuration can *restore*, with the simultaneous generation of an antivortex, due to the strong effect of boundaries. These predicted symmetry-induced vortex states [49] can be stabilized in mesoscopic triangular type-I superconductors with the Ginzburg-Landau parameter $\kappa \lesssim 1/\sqrt{2}$) [51]. (Note that for $\kappa \ll 1/\sqrt{2}$ states with antivortices cannot be stabilized even in the presence of confinement as shown, e.g., for triangles [51] and squares [52].) The dependence of the vortex configurations on the geometry of mesoscopic flat samples, including equilateral triangles, was studied in [66]. It was shown that in very small samples with characteristic sizes of the order of a few ξ (where ξ is the coherence length) and vorticities $L \lesssim 6$, vortex configurations are consistent with the symmetry of the boundary [66]. Moreover, the structure, dynamics of vortices and commensurability effects

* This chapter is based on the following publication:
[1] H. J. Zhao, V. R. Misko, F. M. Peeters, S. Dubonos, V. Oboznov, and I. V. Grigorieva, Europhys. Lett. **83**, 17008 (2008).

were studied in pinning arrays in shape of triangular and kagomé lattices [145] and in arrays of triangular pinning potentials [80, 146–149]. It was demonstrated that triangular pinning potentials, due to their strong asymmetry, can rectify the flux motion either along the driving force (longitudinal rectification) [80, 146–151] or in the perpendicular direction (transverse rectification) [152–154].

Here we present the first direct observation of vortex configurations in μm-sized niobium triangles obtained using the Bitter decoration technique. We also studied the formation of vortex patterns theoretically by analytically solving the London equations using the Green function method and the image technique, and by performing molecular dynamics simulations. We analyze the formation of vortex "shells" similarly to those observed in disks, although unlike vortex shells in disks they are less well defined [155].

3.1 Theory and simulation

To analyze the vortex states in mesoscopic equilateral triangles we use the London approach as we did for studying vortex states in squares in **Chapter** 2. We also neglect the distortion of the magnetic field at the boundary of the sample, then the boundary condition is

$$h|_{\text{boundary}} = H, \tag{3.1}$$

where H is the applied magnetic field. The London Equation Eq. (1.15) with boundary condition Eq. (3.1) can also be solved by the Green function method. The results given in Eq. (2.7) is applicable to other symmetries if the integral is taken in corresponding symmetries instead of rectangle. In equilateral triangles, the local magnetic field is given by

$$\begin{aligned} h(x',y') =& H\left[1-\int_0^{\sqrt{3}a/2} dy \int_{a/2-y/\sqrt{3}}^{a/2+y/\sqrt{3}} dx G(x,y,x',y')\right] \\ &+ \Phi_0 \sum_i G(x_i,y_i,x',y'), \end{aligned} \tag{3.2}$$

where the Green function G associated with the London equation is determined by

$$-\lambda^2\nabla^2 G + G = \delta(x-x')\delta(y-y'), \tag{3.3}$$

using the Cartesian coordinates as depicted in Fig. 3.1(a)). It is more convenient however to use the triangular coordinates (u,v,w) (see Fig. 3.1(a))

defined as follows [156]:

$$\begin{aligned} u &= r - y, \\ v &= \sqrt{3}(x - a/2)/2 + (y - r)/2, \\ w &= -\sqrt{3}(x - a/2)/2 + (y - r)/2. \end{aligned} \tag{3.4}$$

Here, a is the triangle side, $r = a/2\sqrt{3}$ is the inradius of the triangle. Then the boundary condition for the Green function is given by:

$$G(r, v, w) = G(u, r, w) = G(w, v, r) = 0. \tag{3.5}$$

We expand G in a series,

$$\begin{aligned} G(x, y; x', y') = \sum_{m=1}^{\infty} \Bigg\{ & A_m \phi_s^{m,m}(x, y) \phi_s^{m,m}(x', y') \\ & + \sum_{n=m+1}^{\infty} \big[B_{m,n} \phi_s^{m,n}(x, y) \phi_s^{m,n}(x', y') \\ & + C_{m,n} \phi_a^{m,n}(x, y) \phi_a^{m,n}(x', y') \big] \Bigg\}. \end{aligned} \tag{3.6}$$

where $\phi_s^{m,n} = P_{m,n} T_s^{m,n}$, and $\phi_a^{m,n} = Q_{m,n} T_a^{m,n}$. Here, $T_s^{m,n}$ and $T_a^{m,n}$ are the symmetric and antisymmetric eigenfunctions of the Laplace operator with triangular boundary conditions given by:

$$\begin{aligned} T_s^{m,n} = \Bigg\{ & \sin\Big[\frac{2\pi}{9r}(lu + mv + nw + 3lr)\Big] + \sin\Big[\frac{2\pi}{9r}(nu \\ & + mv + lw + 3nr)\Big] + \sin\Big[\frac{2\pi}{9r}(mu + nv + lw + 3mr)\Big] \\ & + \sin\Big[\frac{2\pi}{9r}(mu + lv + nw + 3mr)\Big] + \sin\Big[\frac{2\pi}{9r}(nu + lv \\ & + mw + 3nr)\Big] + \sin\Big[\frac{2\pi}{9r}(lu + nv + mw + 3lr)\Big] \Bigg\}/2, \end{aligned} \tag{3.7}$$

and $T_a^{m,n}$ is described by a similar expression where "sin" is replaced by "cos" and the sign of the even terms is changed to "$-$". Here, $l = -m - n$. The normalization factors are $P_{m,n} = Q_{m,n} = \sqrt{2/(9r^2\sqrt{3})}\, a_{m,n}$ with $a_{m,m} = 1$ and $a_{m,n} = \sqrt{2}$ for $m \neq n$. As proved in Ref. [156], those two functions are complete. The δ-function in Eq. (3.3) can be expanded as

$$\begin{aligned} \delta(x - x')\delta(y - y') = \sum_{m=1}^{\infty} \Bigg\{ & \phi_s^{m,m}(x, y) \phi_s^{m,m}(x', y') + \\ \sum_{n=m+1}^{\infty} & \big[\phi_s^{m,n}(x, y) \phi_s^{m,n}(x', y') + \phi_a^{m,n}(x, y) \phi_a^{m,n}(x', y') \big] \Bigg\}. \end{aligned} \tag{3.8}$$

Then the coefficients in Eq. (3.6) can be determined using Eq. (3.3), which gives:

$$B_{m,n} = C_{m,n} = 1/(-\lambda^2\epsilon_{m,n} + 1)A_m = B_{m,m}. \tag{3.9}$$

and

$$A_m = B_{m,m}. \tag{3.10}$$

Here $\epsilon_{m,n} = (4/27)(\pi/r)^2[m^2 + mn + n^2]$ is the eigenvalue of the Laplace operator. Then, the Green function can be achieved by substituting those coefficients to Eq. (3.6). The integral of the Green function in Eq. (3.2) gives the magnetic field distribution in the Meissner. When $m \neq n$,

$$\int\int dxdy\phi_s^{m,n}(x,y) = \int\int dxdy\phi_a^{m,n}(x,y) = 0. \tag{3.11}$$

Here, the integral is over all the area of the triangle. Thus, the magnetic field is given by

$$\begin{aligned} h(x',y') =& H\left[1 - \sum_{m=1}^{\infty} \frac{2}{\pi m} \cdot \frac{1}{-\lambda^2\epsilon_{m,m} + 1} T_s^{m,m}(x',y')\right] \\ &+ \Phi_0 \sum_i G(x_i, y_i, x', y'). \end{aligned} \tag{3.12}$$

The first part is the contribution of the penetrating external field and the second part is a sum of the contributions of all vortices and their images.

Notice that this result is valid for an equilateral triangle of any size. The first term contains only the eigenfunctions with $m = n$, which gives the contribution from the penetrated external field. The second term associated with the Green function gives the contribution from vortices. Similar as in squares (see Eq. (2.15)), the Gibbs free energy per unit length for an equilateral triangle can also be achieved by substituting Eq. (3.12) to Eq. (1.17). There are two terms (i.e., ϵ^{core} and ϵ^{field}) associated with the vortices' positions. In particular, the screening energy $\epsilon_i^{\text{shield}}$ is given by:

$$\epsilon_i^{\text{shield}} = \frac{\Phi_0 H}{4\pi A}\left[1 - \sum_{m=1}^{\infty} \frac{2}{\pi m} \cdot \frac{1}{-\lambda^2\epsilon_{m,m} + 1} T_s^{m,m}(x_i, y_i)\right], \tag{3.13}$$

where A is the area of the sample. The interaction energy ϵ_{ij}^{v} contains two contributions: one is the interaction between the i^{th} vortex and the j^{th} vortex, another is the interaction between the i^{th} vortex and all the images of the j^{th} vortex. This term is much more complex since the summation of the Green function converges slowly. We thus treat this term by using the image method. The distribution of images of a vortex in a triangle is shown in Fig. 3.1(b). The contribution of the vortices to the magnetic field decays fast at large

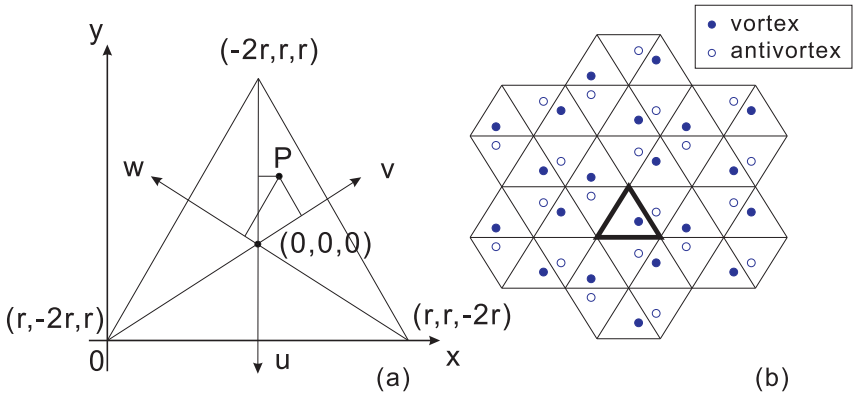

Fig. 3.1 (a)The coordinate system of the triangle. $r = a/2\sqrt{3}$ is the inradius of the triangle. The three boundaries in the triangular coordinate system are given by $u = r$, $w = r$ and $v = r$. The external magnetic field is applied along the z-axis which is perpendicular to this surface, and its value is assumed to be constant outside the sample region. (b) Image technique to determine the vortex-boundary interaction: vortex images in an equilateral triangle. The number of images corresponding to a vortex located inside the triangular sample (the inside region of the thick black lines) is infinite in principle, but since the interaction decays fast ($\sim e^{-r/\lambda}$) at large distances, it is safe to introduce a cut off at a suitable distance ($\sim 6\lambda$).

distances ($\sim e^{-r/\lambda}$). Thus, it is safe to use a cut off ($\sim 6\lambda$) for the interaction between the vortices and with the images. The repulsive vortex-vortex (also vortex-image) interaction is given by Eq. (1.27). The interaction of vortex and antivortex, which is located virtually outside the sample can be obtained by taking a negative sign in Eq. (1.27) as it is attractive. Then the total force which acts on the i^{th} vortex is given by

$$\mathbf{F}_i = -\nabla_i \epsilon_i^{\text{shield}} + \sum_{j\neq i}^{L} \mathbf{f}_{i,j} + \sum_{v} \mathbf{f}_{i,v}. \tag{3.14}$$

The index j in the second term runs over all the vortices inside the triangle. The summation in the third term is taken over all the images v of the vortices inside the sample (within the distance $r < 6\lambda$). The vortex configurations and the field of forces acting on the vortices can be obtained by minimizing the free energy.

To study the stable vortex configurations, we use MD simulations (similar as in squares). The results of our numerical calculations for different vorticities are presented in Figs. 3.2 and 3.3. In Fig. 3.2, vortex configurations are shown for vorticities from $L = 1$ to 9. (Note that in large triangles (i.e., with the size $a > \lambda$) for vorticities $L < 10$, vortex patterns practically do not change with the sample's size. In Fig. 3.2, we show vortex patterns for $a = 3\lambda$. For larger

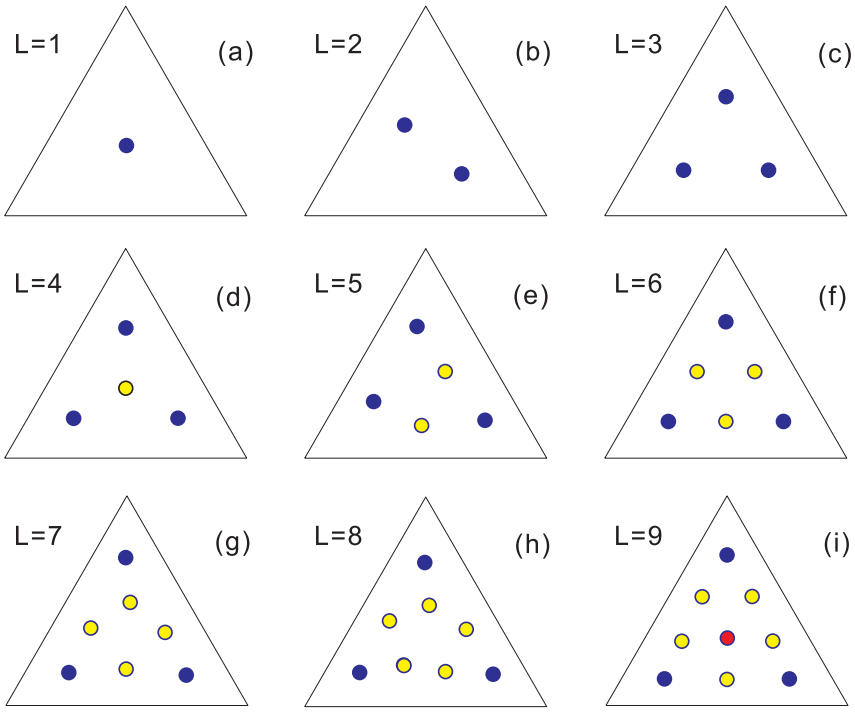

Fig. 3.2 The evolution of vortex configurations for the states with vorticity increasing from $L = 1$ to 9, in superconducting equilateral triangles with side $a = 3\lambda$. The dots show the position of the vortices, and different colors are used to show the different "shells".

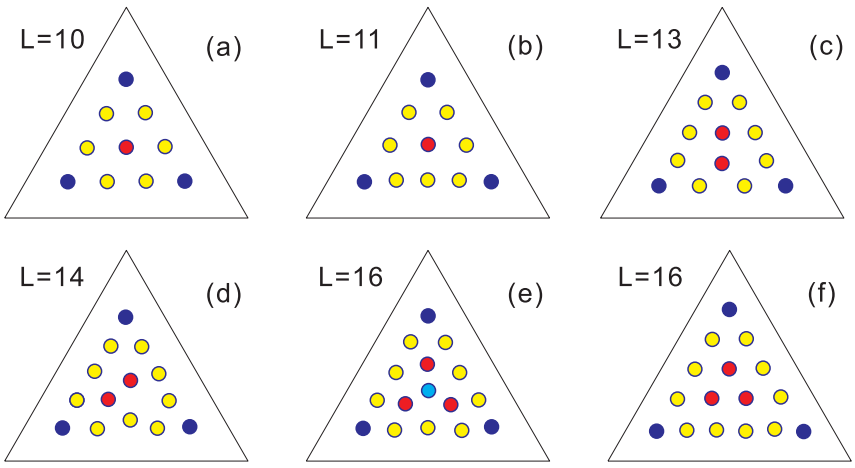

Fig. 3.3 The filling rule of the shells in triangles ($a = 20\lambda$). The new vortices fill the outer "shell" first (e.g., (1,5,3) to (1,7,3)). The number of vortices in the inner "shell" increases to 2 for $L = 13$, and to 3 for $L = 15$. For $L = 16$, there are two configurations, (3,10,6) and (1,3,9,3), with very close free energies.

vorticities, vortex configurations become sensitive to the sample's size. In Figs. 3.3 and 3.6(a), the results for $a = 20\lambda$ are shown.) For the three lowest values of L, Figs. 3.2(a), (b) and (c), vortices appear, correspondingly, in the center, at the line close to the diagonal (notice that in much smaller triangles, $a \sim 10\xi$, where the confinement is much stronger, vortices are situated exactly at the diagonal for $L = 2$ [66]) and in the corners. Fourth vortex appears in the center, thus preserving the C_3 symmetry. Following the terminology and the notations used for disks (e.g., [46, 47, 66]), we can classify vortices with respect to different "shells". Thus, we can define the vortex in the center for $L = 4$ as an inner "shell", i.e., the second "shell" appears when $L = 4$. We notice that for $L > 2$ there are always three vortices in the corners which can be interpreted as an "outer shell" (which is, of course, a matter of choice). Then, the vortices fill the inner shell until $L = 9$, when the third "shell" appears. Since the space close to the boundary in the triangle is much wider than that near the center, the vortices tend to fill the outer shell first (see Figs. 3.2 and 3.3). The vortex configurations always try to occupy at least one of the three symmetry axes of the triangles except $L = 5, 20$. Note that for $L = 3, 6, 10, 15$, perfect triangular lattices are formed.

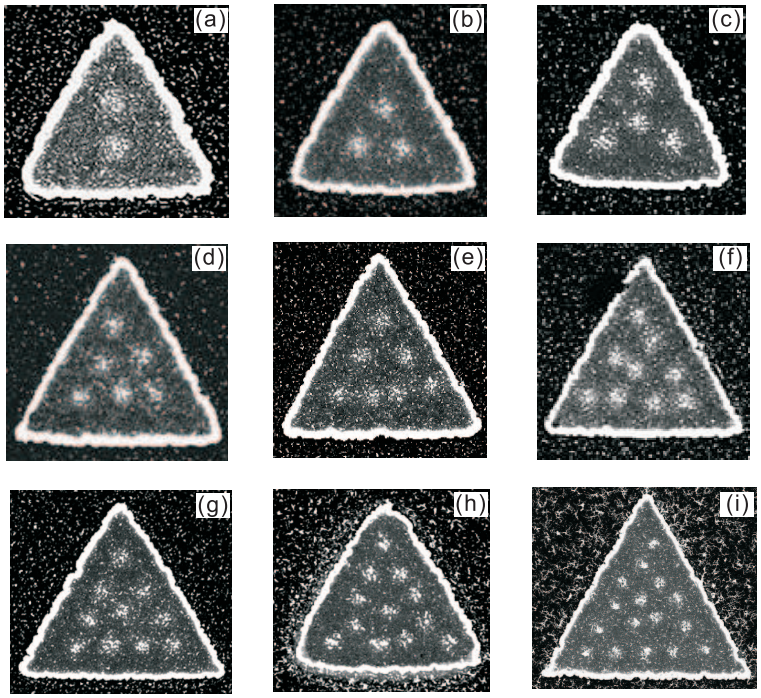

Fig. 3.4 Scanning electron microscope images of vortex states observed experimentally for vorticities $L = 2$ to 16. Clusters of small white (Fe) particles indicate vortex positions. (a) $L = 2$; $a \approx 3$ μm, $H_{\rm ext} = 35$ Oe; (b) $L = 3$; $a \approx 2$ μm, $H_{\rm ext} = 60$ Oe; (c) $L = 4$; $a \approx 3$ μm, $H_{\rm ext} = 40$ Oe; (d) $L = 6$; $a \approx 5$ μm, $H_{\rm ext} = 35$ Oe; (e) $L = 7$; $a \approx 5$ μm, $H_{\rm ext} = 35$ Oe; (f) $L = 9$; $a \approx 5$ μm, $H_{\rm ext} = 40$ Oe; (g) $L = 10$; $a \approx 5$ μm, $H_{\rm ext} = 40$ Oe; (h) $L = 12$; $a \approx 3$ μm, $H_{\rm ext} = 80$ Oe; (i) $L = 16$; $a \approx 5$ μm, $H_{\rm ext} = 60$ Oe;

3.2 Experiment*

To visualise the corresponding vortex configurations experimentally we used the well-known Bitter decoration technique (the details of the technique are described in Sec. 1.3). The mesoscopic samples for this study were made from a 150 nm thick Nb film deposited on a Si substrate using magnetron sputtering. The film's superconducting parameters were: transition temperature $T_c = 9.1$ K, magnetic field penetration depth $\lambda(0) \approx 90$ nm; coherence length

* The experiments were performed at the University of Manchester (UK) by I. V. Grigorieva, in collaboration with S. V. Dubonos and V. Oboznov from the Institute of Solid State Physics in Chernogolovka (Russia).

$\xi(0) \approx 15$ nm; upper critical field $H_{c2}(0) \approx 1.5$ T. The films were then made into arrays of small triangular "dots" of 4 different sizes, with the side of the triangle, a, varying from 1 to 5 μm. To this end, we used e-beam lithography and dry etching through a 250 nm thick Al mask (etching with an Ar ion beam at 5 kV, 0.15 mA/cm^2 at a rate of 0.1 nm/s). A whole array, containing over 150 dots, was decorated in each experiment, allowing us to obtain a snapshot of up to 50 vortex configurations in dots of the same shape and size, produced in identical conditions (same applied magnetic field $H_{\rm ext}$ and temperature T, same decoration conditions). It was therefore possible not only to simultaneously visualise vortex configurations in samples of different sizes but also to gain enough statistics for quantitative analysis of the observed vortex states in terms of their stability, sensitivity to sample imperfections, and so on. Below we present the results obtained after field-cooling to $T \approx 1.8$ K in external fields ranging from 20 to 160 Oe. We note that the above temperature (1.8 K) represents the base temperature for the experiments. Thermal evaporation of Fe particles usually leads to a temporary increase in temperature of decorated samples but the increase never exceeded 2 K in the present experiments, leaving the Nb dots in the low-temperature limit $T < 0.5T_c$. Fig. 3.4 shows typical examples of vortex states observed for vorticities $L = 2$ to 16. The images shown in the figure were obtained in several different experiments (see figure caption of Fig. 3.4) and represent stable configurations for the corresponding values of vorticity, L (see below). We found that for a given value of L the observed configurations did not depend on the sample size or the applied field, at least within the studied field range (the same L resulted from different combinations of a and $H_{\rm ext}$, for example, $L = 4$ was found for $a = 2$ μm and $H_{\rm ext} = 60$ Oe, $a = 3$ μm and $H_{\rm ext} = 40$ Oe, and $a = 5$ μm and $H_{\rm ext} = 20$ Oe). The immediately obvious feature of the observed states is that the triangular shape of the samples imposes a corresponding three-fold symmetry on vortex configurations, while the finer details of the sample boundaries, such as roughness of the boundary or not perfectly sharp angles, do not have any noticeable effect. Furthermore, the vortex states shown in Fig. 3.4 correspond to configurations that we identified as stable for given values of L [47]. Indeed, for most vorticities, we found more that one repeatedly observed vortex configurations for the same L and, after similar analysis to that in Ref. [47], identified the most frequently observed states as ground states and the others as metastable states. This is illustrated in Fig. 3.5 showing the four states observed for $L = 4$, with the state (a) and (b) being almost equally probable (see the figure caption for details), indicating a very small difference between the free energies for corresponding vortex configurations. We note that using many different combinations of the external field and dot sizes allowed us to achieve vortex configurations with almost all possible vorticities L from 0 to about 100. However, as discussed in detail elsewhere [46, 47], as the number of vortices in the dots increases, the effect of confinement potential on the vortices nearer to the center gradually diminishes, so that their arrangement reverts to that in the unpatterned macroscopic film, *i.e.*, the vortex states

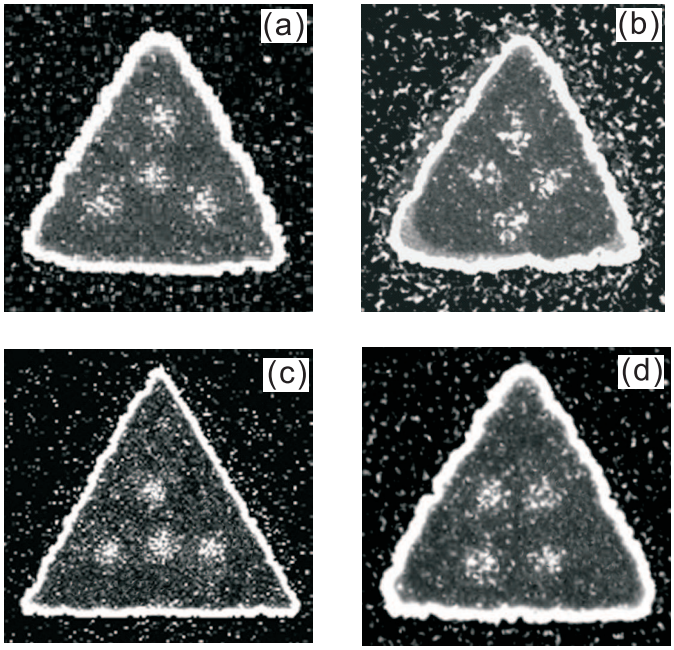

Fig. 3.5 Different vortex configurations observed for the same vorticity $L = 4$, from most frequently found (a) to the least frequent(d). Analysis of the appearance of these states in the same experiment ($a \approx 2$ μm, $H_{ext} = 80$ Oe) revealed the following statistics: Out of the total of 85 dots, 34% showed state (a), 29% showed state (b), 21% showed state (c) and 16% showed state (d).

become less well defined and eventually completely disordered. In circular geometry, the effect of confinement dominated over pinning for vorticities up to $L \approx 40$ [47]. For mesoscopic triangles, however, the well defined states were only found for $L < 20$, as the three-fold symmetry is more difficult to accommodate by interacting vortices. Indeed, our numerical simulations show (see above) that, even in the absence of pinning, stable vortex configurations for certain "incommensurate" vorticities (*e.g.*, $L = 5$ or $L = 14$) appear to be rather disordered.

Finally, we compared the experimentally observed positions of vortices within the triangular dots with those found numerically and we found the vortex states for $L = 1$ to 10 observed in the experiment agree with the result of our simulation (see Figs. 3.2 and 3.4). For $L = 12$, the experiment (Fig. 3.6(b)) shows a "circular" shell structure (i.e., where the vortices of the second "shell", shown by light circles in Figs. 3.2 and 3.3, form a circular-like configuration, see Fig. 3.6). Such "circular" shell structures were found numerically for, e.g., $L = 8$ to 11 (see Figs. 3.2 and 3.3). The calculated

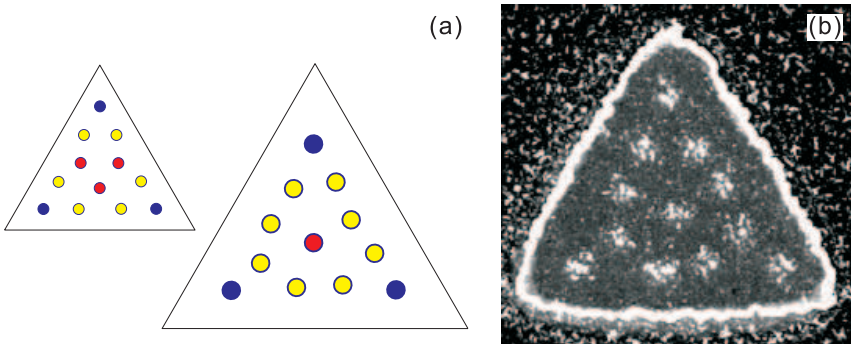

Fig. 3.6 The vortex states for $L = 12$. (a) The calculated vortex configuration for $a = 20\lambda$ and for $a = 3\lambda$ (the inset). (b) SEM images of a vortex configuration with a circular shell for $a = 3\mu\text{m} \approx 33\lambda$.

vortex pattern for $L = 12$ depends on the sample's size. Thus, for $a = 3\lambda$ (the inset in Fig. 3.6(a)), the vortex configuration has a perfect C_3 symmetry, while for $a = 20\lambda$ (Fig. 3.6(a), the main panel), the vortices are less influenced by the boundary and they form a circular-like pattern similar to that found in the experiment. Some small differences between the experimental and the calculated configurations can be explained by imperfections of the samples' shape and presence of weak pinning.

Weak pinning, most probably, is also responsible for the unusual vortex configurations observed for $L = 4$ shown in Figs. 3.5 (experiment) and 3.7 (theory). On the one hand, our numerical simulations show that the only stable state (i.e., the ground state) for $L = 4$ in a *perfect* equilateral triangle is the C_3-symmetric configuration shown in Fig. 3.2(d) (theory) and in Fig. 3.5(a) (experiment). We verified that there are no metastable states for this vorticity even at zero temperature. On the other hand, even a *weak* pinning site (or two pinning sites in Fig. 3.7(c)) placed near the *middle* of the side of the triangle (note that pinning sites in the central part of the sample are more efficient than those near the corners, due to the selective enhancement of the pinning strength [57]) can stabilize (see Fig. 3.7), as *metastable* states, the experimentally observed vortex configurations shown in Figs. 3.5(b), (c), and (d). This also explains why the configuration shown in Fig. 3.5(d) was observed with the lowest probability: we need two pinning sites at suitable positions to realize this configuration. In our numerical calculations, we model pinning sites by parabolic attractive potentials with the maximum pinning force f_p and the radius r_p (see, e.g., Refs. [85, 90, 92, 97–99]), and we take $f_p = 0.5 f_0$, where $f_0 = \Phi_0^2/8\pi^2\lambda^3$, and $r_p = 0.1\lambda$, which correspond to weak pinning regime [57, 157].

In conclusion, we theoretically analyzed vortex configurations in mesoscopic superconducting equilateral triangles within the London theory. We

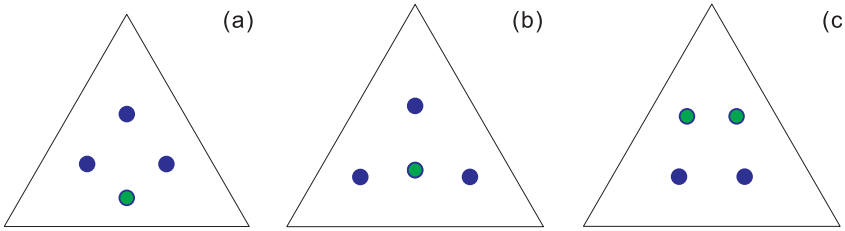

Fig. 3.7 The vortex states for $L = 4$ in the presence of weak pinning with parameters: $f_p = 0.5 f_0$ and $r_p = 0.1\lambda$. The pinned/unpinned vortices are shown by light green/dark blue circles.

solved the London equation analytically using the Green function method. An important feature of the obtained solutions is that they properly describe the effect of the London screening in rather large samples and, in principle, they are applicable to samples of any size. We apply the image technique as an alternative way to find the vortex-vortex interaction. The stable vortex states are obtained by using molecular dynamics simulations. we presented the first direct observation of vortex configurations in mesoscopic niobium triangles, and the theoretical results agree well with the results of the experiment. With corresponding changes, our results can be applied to other interacting systems confined by triangular potentials, e.g., charged particles, colloids, vortices in Bose-Einstein condensates.

Chapter 4

Collective vortex phases in periodic plus random pinning potential*

Vortex states in the presence of pinning were discussed in Sec. 1.4.2, here in this chapter, we consider theoretically a more complicated situation, when there is an additional factor, namely, a random pinning potential [158]. Random pinning is always found in any real physical system; moreover randomness cannot be ruled out even in numerical simulations, where its effect should be carefully analyzed. Samples potentially important for applications have to be very large compared to the period of the regular pinning potential, and therefore disorder and defects in lattices of vortices or other interacting objects are unavoidable. For this reason, understanding of basic properties of such systems is of scientific and hopefully of practical importance.

Thus the structure of the vortex lattice in the system under consideration is determined by three factors: (i) a square array of regular pinning sites, which tries to impose its own symmetry on the vortex lattice, (ii) an interaction between vortices, which favors a triangular configuration of the vortex lattice, (iii) a random pinning potential, which attempts to destroy the regularity in the vortex positions and to depin them from the square lattice. We analyze here analytically various kinds of vortex lattice defects for a two-dimensional system and determine typical values of the random pinning strengths leading to a spontaneous generation of these defects. This allows us to construct an approximate phase diagram of the system in the plane

* This chapter is based on the following publication:
[1] W. V. Pogosov, V. R. Misko, H. J. Zhao, and F. M. Peeters, Phys. Rev. B **79**, 014504 (2009).

of regular pinning strength and random pinning strength. We also perform molecular dynamics simulations in order to model numerically the process of disordering of the square vortex array. The obtained vortex patterns and the typical values of random pinning strength producing disordering are in good agreement with our expectations obtained from the analytical treatment.

Note that the problem studied can be also linked to other situations when there is a competition of randomness and regularity, but where the dimensionalities of the pinning potential and an elastic media are possibly different from two-dimensional. These are flux-line lattices in layered superconductors, where layers act as one-dimensional pinning centers giving rise to a so-called intrinsic pinning. Such pinning centers can also be created by twin boundaries. Since there is always disorder in real superconductors, one can also have a competition between randomness and regularity [159–161]. Other examples are charge and spin density waves.

4.1 Model

4.1.1 Basic formalism

In our model, we treat vortices as point-like objects interacting via a pair-wise potential, which are valid assumptions as long as the applied magnetic field is much lower than the second critical field H_{c2}, and the Ginzburg Landau parameter is large, $\kappa \gg 1$. As was introduced in Sec. 1.2, the interaction energy of two vortices positioned at $\mathbf{r}_1$ and $\mathbf{r}_2$ can be well approximated by the well-known London expression (i.e., Eq. (1.26)). In this chapter, the following dimensionless variables are used: distances are measured in terms of the London penetration depth λ and energy is measured in units of $H_c^2\lambda^3/8\pi$ with H_c being the thermodynamic critical field. An important quantity, which we are going to use, is the interaction energy of a regular vortex row with a given vortex situated outside of this row. If we put a center of coordinates at one of the vortices in the row, and the y-axis is along the row, then the interaction energy of the vortex located at $(x,\, y)$ is given by

$$H_{int}^{row}(x,y) = \frac{2\pi}{\kappa^2} \sum_{m=-\infty}^{\infty} K_0\left(\sqrt{x^2+(y+md)^2}\right), \tag{4.1}$$

where d is the vortex-vortex distance. Using Fourier transformation for a modified Bessel function $K_0(r)$ and performing a summation in the reciprocal

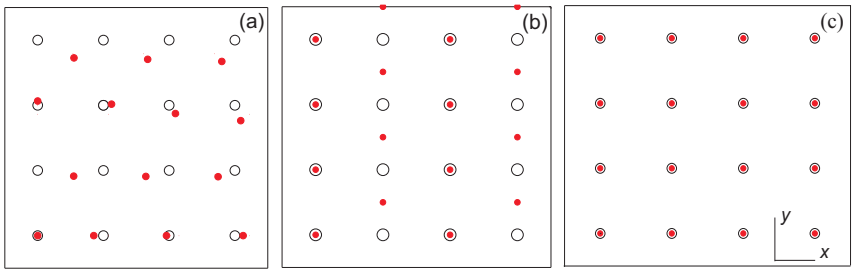

Fig. 4.1 Vortex lattice structure in a superconducting film with weak periodic pinning at filling factor 1. Vortices are shown by red (dark gray) filled circles and pinning sites by black open cirles. Fig. (a) corresponds to the case of very low pinning with the deformed triangular vortex lattice. Fig. (b) shows a half-pinned regular phase realized at intermediate values of pinning strength. Fig. (c) represents a pinned vortex lattice, which is energetically favorable at higher values of pinning strength.

space, Eq. (4.1) can be rewritten as

$$H_{int}^{(row)}(x,y) = \frac{2\pi}{\kappa^2}\frac{\pi}{d}\sum_{m=-\infty}^{\infty}\frac{1}{\sqrt{1+\frac{4\pi^2m^2}{d^2}}} \times \exp\left(-x\sqrt{1+\frac{4\pi^2m^2}{d^2}}\right)\cos\frac{2\pi my}{d}. \tag{4.2}$$

Vortices are located in a two-dimensional film with a periodic square array of pinning sites. To describe the pinning potential of a single site, we use a parabolic function:

$$V(\mathbf{r}) = -U_0\left(1-\left(\frac{|\mathbf{r}|}{\sigma}\right)^2\right) \tag{4.3}$$

inside the well, $r \le \sigma$, and the potential is zero outside the well, $r > \sigma$. In this paper, we consider the situation when the well radius σ is much smaller than the intersite distance a, i.e., $\sigma \ll a$.

In addition to the regular pinning potential there is also a random pinning potential in the system; we denote its energy by $\varepsilon(\mathbf{r})$. The total energy of the system is thus given by

$$E = \sum_{i,j} H_{int}(\mathbf{r}_i,\mathbf{r}_j) + \sum_{i,n} V(\mathbf{R}_n - \mathbf{r}_i) + \sum_i \varepsilon(\mathbf{r}_i), \tag{4.4}$$

where $\mathbf{r}_i$ and $\mathbf{R}_n$ stand for the positions of vortices and regular pinning sites, respectively. We also assume that the number of vortices is exactly equal to the number of pinning sites, i.e., filling factor is one.

Let us recall first the situation when there is no random potential in the system. In this case, as was explained in the Introduction, strong regular pinning favors a square vortex lattice symmetry, see Fig. 4.1(c). At low U_0 the

repulsion between vortices dominates resulting in a slightly deformed triangular lattice that has the lowest energy, as illustrated in Fig. 4.1(a). Finally, in the intermediate range of U_0, a half-pinned lattice becomes the ground state, see Fig. 4.1(b). In the half-pinned phase, an effective pinning potential for depinned vortices is created by their interaction with neighboring rows of pinned vortices. It is easy to see that the following expressions define the boundaries between the triangular lattice and the half-pinned phase, and half-pinned phase and square lattice, respectively [100, 102]

$$U_0 \simeq 2\left(E_{hp} - E_{tr}\right) \tag{4.5}$$

$$U_0 = 2\left(E_{sq} - E_{hp}\right), \tag{4.6}$$

where E_{tr}, E_{hp}, and E_{sq} are the energies of triangular, half-pinned and square vortex lattices, without any pinning, taken per one vortex. In other words, these vortex-vortex interaction energies depend only on vortex lattice symmetry. We focus on the situation when the strength of a regular pinning is not too high, i.e., is close to the boundaries defined by Eqs. (4.5) and (4.6). In this case the vortex lattice can be considered as a collective object and we are far from the regime of single-vortex pinning.

4.1.2 Molecular dynamics simulations

In addition to an analytical approach, we supplement our study with computer experiments. In this section, we describe briefly the basic ingredients of the used computer simulations. We use MD simulations of vortices moving under the action of the forces due to the vortex-vortex interaction and the interaction of vortices with regular and random pinning sites. To find the lowest-energy vortex configurations, we perform simulated annealing simulations by numerically integrating the overdamped equations of motion (see **Chapter** 2):

$$\eta \mathbf{v}_i \;=\; \mathbf{f}_i \;=\; \mathbf{f}_i^{vv} + \mathbf{f}_i^{vp} + \mathbf{f}_i^{T}. \tag{4.7}$$

Here, $\mathbf{f}_i$ is the total force per unit length acting on vortex i, $\mathbf{f}_i^{vv}$ and $\mathbf{f}_i^{vp}$ are the forces due to the vortex-vortex and vortex-pin interactions, respectively, and $\mathbf{f}_i^{T}$ is the thermal stochastic force. η is the viscosity, which is set here to unity. The force due to the interaction of the i-th vortex with other vortices is given by Eq. (1.27). The modified Bessel function $K_1(r)$ decays exponentially for r larger than 1 (λ in dimensional units), thus it is safe to cut off the (negligible) force for distances larger than 5. In our calculations, the logarithmic divergence of the vortex-vortex interaction forces for $r \to 0$ is eliminated by using a cutoff at distances smaller than 0.1.

The force due to the interaction of the i^{th} vortex with the parabolic pinning potentials (Eq. (4.3)) is:

$$\mathbf{f}_i^{vp} = \sum_{k}^{N_p} \left(\frac{f_p}{\sigma}\right) \mid \mathbf{r}_i - \mathbf{r}_k^{(p)} \mid \Theta\Big(r_p - \mid \mathbf{r}_i - \mathbf{r}_k^{(p)} \mid\Big)\, \hat{\mathbf{r}}_{ik}^{(p)}, \tag{4.8}$$

where N_p is the number of pinning sites, f_p is the maximal pinning force of each potential well, σ is the spatial range of the pinning potential (for random potentials, we define $f_{pr} \lesssim f_p$ and $\sigma_r \lesssim \sigma$ as the maximum pinning force and radius, correspondingly), Θ is the Heaviside step function, and $\hat{\mathbf{r}}_{ik}^{(p)} = (\mathbf{r}_i - \mathbf{r}_k^{(p)})/\mid \mathbf{r}_i - \mathbf{r}_k^{(p)} \mid$.

The temperature contribution to Eq. (4.7) is similar as the thermal term used in the previous chapters. The ground state of a system of vortices is obtained as follows. First we set a high temperature to let vortices move randomly, then temperature is gradually decreased down to $T = 0$, thus simulating field-cooled experiments (see, e.g. Refs. [142, 149]).

4.2 Kinks

Both square and half-pinned phases are periodic in the absence of random pinning sites. Translational motion of the vortex lattice as a whole by a period of a regular pinning lattice a does not change the energy of the system. Therefore, one can expect that there exist such solutions when, in one region of the system, the vortex lattice is shifted by a with respect to that in another region. There should also be a kink with intermediate value(s) for deviations of vortex positions separating these domains. In this sense, our system resembles a traditional sine-Gordon system, which describes the behavior of elastic media in a periodic potential [31]. For sine-Gordon systems, a typical kink has a smooth structure and its length depends both on the elastic properties of the media and the strength of the periodic potential, and it can be arbitrary large. Kinks are known to play an important role in the process of disordering of media [31]. Thus one may say that disordering is occurring through a *proliferation of kinks*. Therefore, we will pay special attention to the kink structure.

4.2.1 Continuous kinks versus sharp defects

One can naively assume that there also exist smooth kinks for square pinned and half-pinned lattices. However, despite the similarity with sine-Gordon systems, our system has one specific feature, namely, square and half-pinned vortex configurations are *not* the lowest energy states in the absence of pinning. Moreover, they are *locally* unstable, i.e., even infinitesimally small displacements of vortices lead to the collapse of the lattice into a triangular array. In other words, the elasticity theory does not work properly. This is shown explicitly in the Appendix, where we also determine a structure of an infinite-length kink. We found that it has a "discrete" (i.e., not smooth) structure, which is shown in Fig. 4.2(a). This is a fundamental difference between the system at hand and conventional sine-Gordon systems.

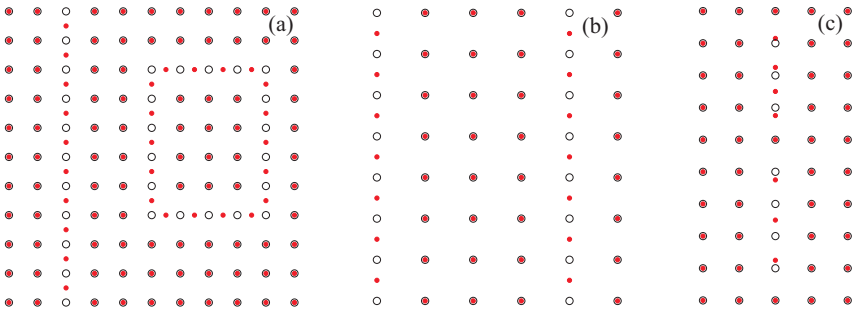

Fig. 4.2 Schematic view of typical defects in a regular vortex lattice. Vortices/pinning sites are shown by red (dark gray) filled circles/black open cirles. Fig. (a) shows elastic strings of unpinned vortices in the square pinned lattice: straight (on the left) and reconnected (on the right). Fig. (b) presents a row of pinned vortices in the half-pinned phase. Fig. (c) corresponds to the quasi-one-dimensional defect of finite length inside the pinned square lattice.

Note that in the infinite system this type of defects has a divergent energy because it is of infinitely long. Therefore, fluctuations generate *reconnected* kinks of finite sizes rather than infinitely long defects, as shown in Fig. 4.2 (a). This point will be explained in detail in Sec. 4.4 Also notice that the fact of appearance of reconnected defects is well-known in the condensed matter physics, see e.g. Ref. [31] for sine-Gordon and related systems.

It is important to notice that the string of unpinned vortices behaves as an elastic object, vortices inside the string are correlated and behave collectively due to their interaction. It is easy to see from Fig. 4.2(a) that such a defect can be considered as a nucleus of a half-pinned vortex phase. The defect energy density can be therefore estimated as a difference in the energy density between the half-pinned and pinned vortex phases. They are given, respectively, by

$$\varepsilon_{hp} = \frac{E_{hp} - U_0/2}{a^2}, \tag{4.9}$$

$$\varepsilon_{sq} = \frac{E_{sq} - U_0}{a^2}. \tag{4.10}$$

The first term in the numerator in the right-hand side (RHS) of Eq. (4.9) (Eq. (4.10)) is the energy of the vortex-vortex interaction, taken per one vortex, while the second term denotes the pinning energy per one vortex. The latter terms are different for the half-pinned (Eq. (4.9)) and for pinned (Eq. (4.10)) phases, since in the second case all the vortices are pinned, while in the first case – only half. Denominators in the RHS of Eqs. (4.9) and (4.10) give the area per one vortex. Finally, for the defect energy density we obtain

$$E_d^{(1)} \approx \varepsilon_{hp} - \varepsilon_{sq} = \frac{U_0/2 - (E_{sq} - E_{hp})}{a^2}. \tag{4.11}$$

It is important to note that the kink energy vanishes at the transition between the square and half-pinned lattices, i.e., at $U_0 = 2\,(E_{sq} - E_{hp})$ since energies of these two phases become equal.

It is easy to realize that the pinned phase can also be disturbed by a domain composed by a region of a deformed triangular vortex lattice. Again such a domain is an elastic object, vortices within the domain are depinned collectively. The region of depinned vortices has higher energy density compared to the previously described string-like defect, since the energy of a deformed triangular lattice has a higher energy than the half pinned lattice in the relevant parameter region. This energy density can be estimated in a similar manner, as the one which led us to Eq. (4.11). For that we need to know the energy density of the deformed triangular lattice, which is given by [102]

$$\varepsilon_{tr} \approx \frac{E_{tr}}{a^2}, \tag{4.12}$$

where E_{tr} is the vortex-vortex interaction energy in the ideal triangular lattice taken per one vortex. In reality, this lattice is deformed and it is not ideal. However, as it was shown in Ref. [102], the energy of elastic distortions is compensated by the pinning energy in the linear approximation with respect to vortices displacement, and Eq. (4.12) is correct. Finally, for the density energy of the defect we obtain

$$E_d^{(2)} \approx \varepsilon_{tr} - \varepsilon_{sq} = \frac{U_0 - (E_{sq} - E_{tr})}{a^2}. \tag{4.13}$$

Now we turn to the description of the half-pinned phase. By similarity with the pinned phase, we can see that a typical kink in the half pinned phase consists of a row of pinned phase. One can also have domains of triangular phases. The first type of defect is shown schematically in Fig. 4.2(b). The energy densities for these kinks can be calculated from the differences in energy densities of the nucleating phase and the initial one, as for Eqs. (4.11) and (4.13). They are given, respectively, by

$$E_d^{(3)} \approx \varepsilon_{sq} - \varepsilon_{hp} = \frac{-U_0/2 + (E_{sq} - E_{hp})}{a^2}, \tag{4.14}$$

$$E_d^{(4)} \approx \varepsilon_{tr} - \varepsilon_{hp} = \frac{U_0/2 - (E_{hp} - E_{tr})}{a^2}. \tag{4.15}$$

which of the kinks has a lower-energy density depends on the position in the phase diagram. As again can be expected, defects of the first type, shown in Fig. 4.2(b), should be reconnected in finite systems.

4.2.2 Quasi-one-dimensional defects

We note that a one more type of the defects appears in the system for sufficiently larger values of U_0, when the potential well for a pinned vortex row is

much deeper than the effective potential well created for a depinned vortex row by surrounding rows of pinned vortices. In this limit, the defect considered is a finite row of unpinned vortices, but *not reconnected*. Such a structure can exist due to the fact that in one part of the defect, the string of vortices is stretched so that there is one missing vortex and the last vortex in this part of the string deviates from its equilibrium position by one period of the regular lattice a. In another part of the defect, the string of vortices is compressed so that there is an excess vortex. This defect is shown schematically in Fig. 4.2(c) for the most simple case, when it is straight. It consists of a finite elastic string of vortices in the same row, which are displaced along the direction of the row. Thus this object as a whole can be considered as a *quasi-one-dimensional kink-antikink structure*. In Sec. 4.4, by using molecular dynamics simulations and rather general arguments, we argue that both reconnected chains of depinned vortices and quasi-one-dimensional defects are limiting cases of wider class of collective fractal-like defects. In other words, defects considered in this section are not necessarily straight, but straight defects can be more easily studied analytically.

We now calculate typical energy and length of this quasi-one-dimensional defect. We assume that positions of all other vortices in the system remain unchanged. The potential energy of a vortex in the string is given by the interaction energy with the fixed vortices, with pinning sites, and also with each other. The first contribution to the string energy can be found from Eq. (4.2), where one can neglect all the terms except of the ones with $m = 0, \pm 1$ provided that $a \sim 1$, which results in

$$E_1^{(1D)} \simeq \frac{4\pi}{\kappa^2}\frac{\pi}{a}\sum_k \left(\frac{\exp(-a)}{1-\exp(-a)} + \frac{a}{\pi}\exp(-2\pi)\cos\frac{2\pi y_k}{a} \right), \qquad (4.16)$$

where the summation is performed over positions of all vortices in the string y_k. Note that from this equation one can see that the vortex-vortex interaction favors a shift of $a/2$ of the row in the y direction with respect to the lattice making a symmetry closer to the triangular one. Note that the potential energy (Eq. 4.16) for each vortex has a typical sine-Gordon structure.

The interaction energy for the vortices with pinning sites in the row reads

$$E_2^{(1D)} = \sum_{n=-\infty}^{\infty}\sum_k V(an - y_k), \qquad (4.17)$$

where $V(y)$ is defined by Eq. (4.3) and the index n stands for the positions of the pinning sites. For illustrative purposes, we plot the sum of $E_1^{(1D)}$ and $E_2^{(1D)}$ in Fig. 4.3(a) for vortices in the string that are positioned periodically, $y_k = y + ka$. The resulting potential is, of course, a periodic function in y. The energy minimum for the string is attained for a square configuration due to our choice of parameters, i.e., for strong enough regular pinning. To show that this potential is of a quasi-one-dimensional form, we also plot it in three dimensional form in Fig. 4.3(b).

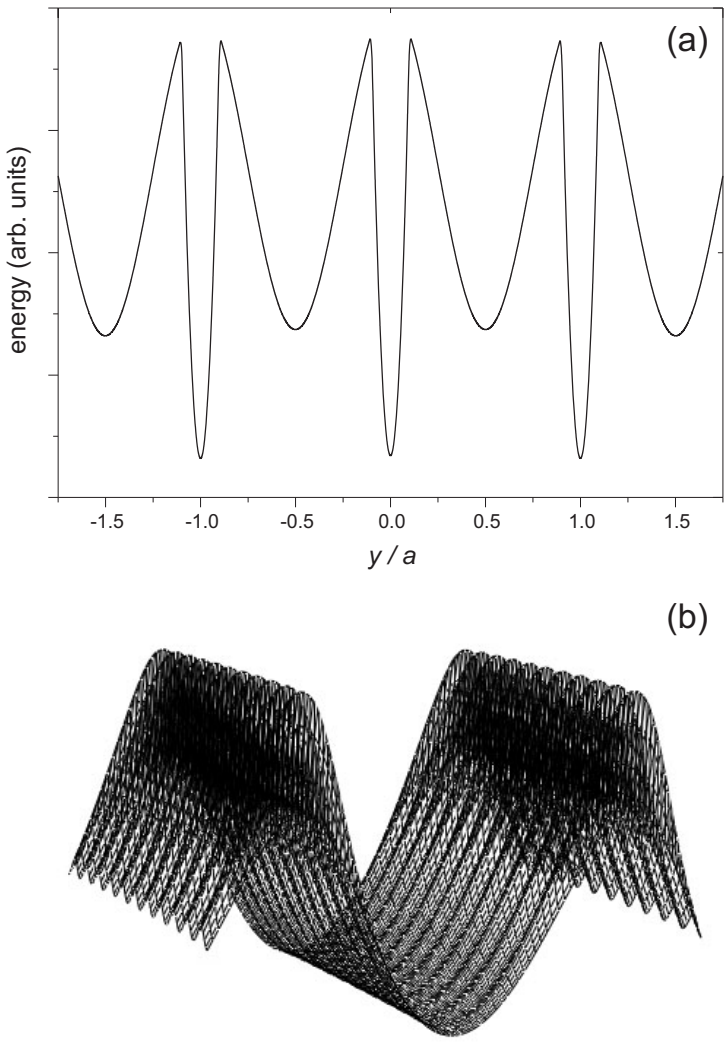

Fig. 4.3 Potential energy profile for the vortex row in the square lattice along one of the principal axis, provided that positions of vortices in the row are fixed with respect to each other and all other vortices are pinned. Fig. (a) corresponds to the dependence on one coordinate, whereas Fig. (b) shows a dependence on both coordinates, which is of quasi-one-dimensional form.

There is an additional contribution to the energy of the vortex, which is due to its interaction with other vortices in the string, i.e., the elasticity term. This contribution depends on the mutual positions of the vortices. We will take into account only the interaction with nearest neighbors, as is usually done in elasticity theory. Taking into account Eq. (4.1) and using a Taylor expansion for the modified Bessel function, we obtain the following expression for the energy of the whole string of vortices

$$E_3^{(1D)} = \frac{2\pi}{\kappa^2}\left(K_0(a) + \frac{K_1(a)}{a}\right)\sum_k (\Delta u_k)^2, \tag{4.18}$$

where Δu_k is the displacement of k^{th} vortex with respect to the $(k-1)^{th}$ one. As usual, we can replace $\Delta u_k/a$ by du/dy and also switch from the summation to the integration in the RHS of Eq. (4.18) [31]:

$$E_3^{(1D)} = \frac{2\pi a}{\kappa^2}\left(K_0(a) + \frac{K_1(a)}{a}\right)\int \left(\frac{du}{dy}\right)^2 dy, \tag{4.19}$$

where the integration is performed along the length of the defect. The total energy of the defect is thus given by the sum of three contributions:

$$E^{(1D)} = E_1^{(1D)} + E_2^{(1D)} + E_3^{(1D)}, \tag{24}$$

which can be estimated in a simple manner. We assume that a typical kink-antikink structure has a length l_{1D}. There are l_{1D}/a vortices along this defect and they are depinned from their lowest energy positions. Each vortex gains some energy by being depinned. If the width of the potential well σ is much smaller than the intersite distance a, the gain is given by U_0, as follows from Eq. (4.19). At the same time, each vortex also loses some amount of energy due to the fact that it no longer forms a square configuration with vortices from the surrounding fixed rows, as can be seen from Eq. (4.19). Thus, the total energy increase for the string of l_{1D}/a depinned vortices is given approximately by

$$E_1^{(1D)} + E_2^{(1D)} \approx l_{1D}/a\left(U_0 - \frac{4\pi}{\kappa^2}e^{-2\pi}\right). \tag{4.20}$$

The elastic energy of the string $E_3^{(1D)}$ can be easily estimated from Eq. (4.19) as

$$E_3^{(1D)} \approx \frac{2\pi a^3}{\kappa^2}\frac{1}{l_{1D}}\left(K_0(a) + \frac{K_1(a)}{a}\right). \tag{4.21}$$

If we now minimize the total defect's energy $E^{(1D)}$ with respect to its length l_{1D}, we obtain

$$l_{1D} \approx \sqrt{\frac{2\pi a^4}{\left(U_0 - \frac{4\pi}{\kappa^2}e^{-2\pi}\right)\kappa^2}\left(K_0(a) + \frac{K_1(a)}{a}\right)}. \tag{4.22}$$

This leads to the following result for the defect energy

$$E^{(1D)} \approx 2\sqrt{\frac{2\pi a^2\left(U_0 - \frac{4\pi}{\kappa^2}e^{-2\pi}\right)}{\kappa^2}\left(K_0(a) + \frac{K_1(a)}{a}\right)}, \tag{4.23}$$

which has a nontrivial dependence on U_0. As we will see below, in the limit of weak pinning, quasi-1D defects have higher energies compared to previously analyzed ones. This can be explained by noticing that vortices in the string are situated neither exactly in a potential well induced by pinning sites nor in that created by the neighboring rows of vortices.

Note that a quasi-1D defect can have a slightly different structure, when the maximum deviation of vortex in the string from its equilibrium position is given by $a/2$ but not by a. In this case, the position of the most strongly displaced vortex in the row is stabilized by the interaction with neighboring rows of vortices and not by a pinning site. Our estimates for length and energy of quasi-one-dimensional defect, given by Eqs. (4.22) and (4.23), however remain applicable also for such a defect.

4.3 Random potential

In this section, we characterize the random potential and describe how to deal with it in our problem. We assume that the random potential is created by randomly distributed pinning wells with size $\sigma_r \lesssim \sigma$, a and depth $U_r \lesssim U_0$. The concentration of random sites is denoted by n_r, and we also assume that it is higher or equal to the concentration of regular pinning sites, $n_r \gtrsim a^{-2}$.

It is well-known that the actual pinning energy due to the random pinning is produced by fluctuations of the random potential in a given region of the system, i.e. by bunches of pins, and not by pinning potential averaged value. If we have a region of area $S_0 \gg n_r^{-1}$, the distribution probability $P(N)$ for having N random pinning sites within this region can be well described by a normal distribution

$$P(N) = \frac{1}{\sqrt{2\pi}}\frac{1}{\sqrt{n_r S_0}}\exp\left[-\frac{(N - n_r S_0)^2}{2n_r S_0}\right]. \tag{4.24}$$

As can be expected, the averaged value of N is given by

$$\langle N\rangle = n_r S_0, \tag{4.25}$$

whereas the mean-square deviation reads

$$\sqrt{\langle N^2\rangle - \langle N\rangle^2} \simeq n_r S_0. \tag{4.26}$$

The probability to have any number of random pinning sites larger than some definite value N_0 within the region S_0 can be found by integration,

$\int_{N_0}^{\infty} P(N)dN$, and this integral can be estimated as (provided that $N_0 - n_r S_0 \gtrsim \sqrt{n_r S_0}$)

$$\int_{N_0}^{\infty} P(N)dN \approx \frac{1}{\sqrt{2\pi}} \frac{\sqrt{n_r S_0}}{N_0 - n_r S_0} \exp\left[-\frac{(N_0 - n_r S_0)^2}{2 n_r S_0}\right]. \tag{4.27}$$

The probability for this event not to occur is, of course, $1 - \int_{N_0}^{\infty} P(N)dN$. If we now have a larger region $S > S_0$, the probability that, within S, one cannot find a region of area S_0 with number of random pinning sites larger than N_0 is estimated as $\sim \left(1 - \int_{N_0}^{\infty} P(N)dN\right)^{S/S_0}$. Finally, the probability to find such a region is $1 - \left(1 - \int_{N_0}^{\infty} P(N)dN\right)^{S/S_0}$. From this analysis and from Eq. (4.27) it is easy to see that if $S \sim S_0$ and $|N_0 - n_r S_0| \sim \sqrt{n_r S_0}$, this probability is very close to 1. This means that within the domain of area S slightly larger than S_0 we can always find a bunch of pines, such that the pinning energy around this bunch (within region of area S_0) deviates by $\sqrt{n_r S_0}$ from its average value. This illustrates that the effective pinning energy within some region can be closely approximated by mean-square deviation of random pinning potential within this region, $U_r\sqrt{n_r S_0}$. This conclusion is well-known in the physics of disordered flux-line lattices [162]. The famous Larkin-Ovchinnikov theory is also based on the idea that the mean-square deviation of random pinning energy is balanced with the energy of lattice distortions within some domain.

Each kind of defects described in Sec. 4.3 has its own typical energy and sizes. In order to estimate the random pinning strength leading to a proliferation of such defects one can equate the defect energy to the mean-square deviation of the random pinning potential within the characteristic area of the defect. By doing this, one can study the phase diagram of the system in the plane of random and regular pinning sites strengths.

4.4 Phase diagram

In the absence of random pinning, there are two phase boundaries separating the pinned square, half pinned and deformed triangular lattices, as given by Eqs. (4.5) and (4.6). We now consider the effect of the random pinning potential. Note that a deformed triangular vortex lattice is aperiodic even in the absence of random pinning, since periods of vortex and regular pinning sites lattices are incommensurate. Therefore we consider disordering of square pinned and half-pinned vortex lattices, which have a regular structure. As was already explained, the destruction of the order occurs via a proliferation of defects. Using the tools developed in Secs. 4.2 and 4.3, we can estimate the typical random pinning strengths leading to a generation of different defects, identified in Sec. 4.2. We do not expect that this will give us the full phase

diagram, since we have found defects only in some simple and limiting cases. In order to obtain a deeper insight to the problem we will also use molecular dynamics simulations.

Let's start from the case of a square pinned lattice. The lowest energy defect in such a situation, among those we have found, is constructed from the elastic string of collectively depinned vortices, as explained in Sec. 4.2. This row has to be reconnected because otherwise its energy is infinitely large [31] (therefore, one should pay a special attention to this point both in numerical and real experiments on finite arrays, since there it is easy to get just straight defects - their energies remain finite because the system sizes are finite). The radius of such a defect cannot be too small, since the system is discrete. Therefore, the lowest energy defect has a radius R_d of the order of the intersite distance, $R_d \sim a$, see Fig. 4.2 (a). Let us write R_d as ar_d, where the dimensionless factor r_d is of the order of one, $r_d \sim 1$. The energy of such a defect can be found from Eq. (4.11):

$$E_{kink} \sim 2\pi r_d \left[U_0/2 - (E_{sq} - E_{hp})\right]. \tag{4.28}$$

The area of this structure is just $\pi a^2 r_d^2$. To find the random pinning strength leading to a proliferation of this particular kind of defects, we equate the energy of the defect E_{kink} to the mean-square deviation of the random pinning energy within the area of the defect $U_r\sqrt{n_r \pi a^2 r_d^2}$ and we find

$$U_r \sim \sqrt{\frac{\pi}{n_r a^2}}\left[U_0 - 2\left(E_{sq} - E_{hp}\right)\right]. \tag{4.29}$$

From Eq. (4.29) we see that the U_r required to destroy the order in the vortex positions in the square pinned phase vanishes at $U_0 = 2\left(E_{sq} - E_{hp}\right)$, i.e., in the point of the transition between the square pinned and half-pinned lattices in the absence of disorder. This means that arbitrary weak disorder destroys the regularity in a square vortex lattice in the vicinity of this point, since the energies of pinned and half pinned lattices are equal to each other there.

We now start to construct a phase diagram of the system in the U_0 - U_r plane for the same concentration of random and regular pins, i.e., $n_r a^2 = 1$. The boundary separating pinned and a mixture of pinned and half-pinned lattices is shown by line 1 in Fig. 4.4 at $a = 1$ and $\kappa = 5$. This mixed phase still can be considered as pinned, as a whole, by the regular pinning sites array, since there is a strong correlation between the positions of regular sites and the vortices.

Let us now switch to the half-pinned phase. As was explained in Sec. 4.2, the lowest energy defect in this case corresponds to the row of pinned vortices, which recovers locally square array, as in Fig. 4.2(b). This row again has to be reconnected. By repeating the derivation which led us to Eq. 4.29, we obtain the following criterion for U_r favoring proliferation of such defects

$$U_r \sim \sqrt{\frac{\pi}{n_r a^2}}\left[-U_0 + 2\left(E_{sq} - E_{hp}\right)\right]. \tag{4.30}$$

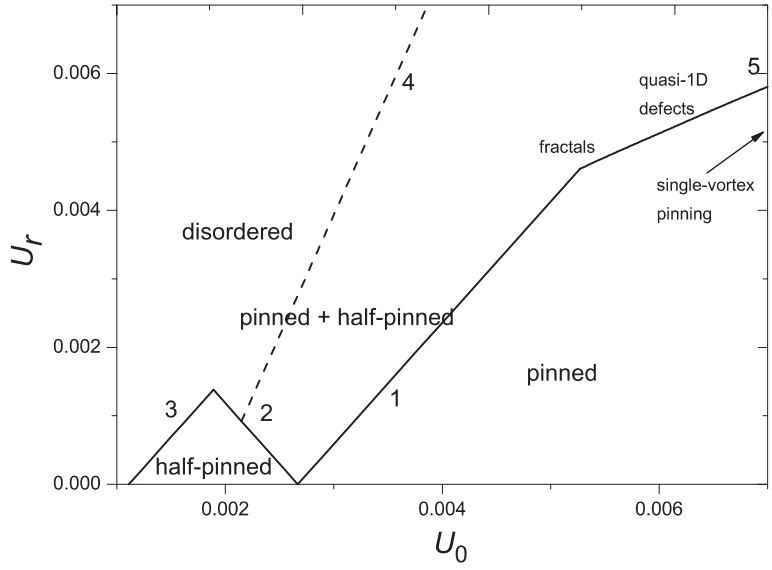

Fig. 4.4 Schematic phase diagram of the vortex lattice in the plane of the periodic pinning strength U_0 and the random pinning strength U_r.

It corresponds to the curve 2 in the phase diagram which is basically a mirror image of the boundary given by Eq. (4.29). It is interesting to note that *disorder* in this case leads to an unexpected situation, namely, it forces vortices within some regions to be pinned by the *regular* array of pinning sites. Also note that if we follow along curves 1 and 2, we see that the minimal random pinning strength required for the partial disordering of the vortex lattice is a non-monotonic function of U_0. This is again a nontrivial result, since one could expect that the higher U_0, the higher must be U_r, which destroys the order in the vortex positions. However, this is not exactly the case, since there is one more factor, i.e., the vortex-vortex interaction, which helps the random pinning sites to destroy order. Thus, at a certain value of U_0 it is energetically favorable for the system to decrease its energy not by introducing vortex lattice defects, but by making a structural phase transition of the vortex lattice, on large scales, into a half-pinned *regular* phase.

The half-pinned phase can also be destroyed via elastic domains of the deformed triangular lattice; the energy density for the corresponding defect is given by Eq. (4.15). Thus, the random energy U_r generating such domains can be estimated as

$$U_r \sim \sqrt{\frac{\pi}{n_r a^2}} \left[U_0 - 2\left(E_{hp} - E_{tr}\right)\right]. \tag{4.31}$$

It is shown as curve 3 in Fig. 4.4, which separates regions of half-pinned and deformed triangular, i.e., completely disordered, phase. Let us stress that proliferation of such domains leads to a complete depinning of the vortex lattice from the underlying square array of pinning sites. Curves 2 and 3 intersect in some point and they bound a region in the phase diagram where the half pinned vortex lattice is stabilized. Of course, this does not mean that there are no defects at all in this region (or in the region of the square pinned lattice), but this implies that their concentration is low. One should also understand that the state, which we call a mixture of pinned and half pinned phases, contains domains with the deformed triangular lattice as well, but again the concentration of such domains is low. There can be other types of defects, like vacancies, when one vortex is redistributed to the position which is very far, in terms of lattice period, from its initial position, however, the probability of such events is low, since we are in the regime of collective pinning. Therefore, such events do not contribute significantly to the process of vortex lattice disordering.

Now we discuss how a mixture of pinned and half pinned phases is finally completely depinned from the regular pinning array. For that we first estimate U_r generating domains of triangular lattice inside the *square* one:

$$U_r \sim 2\sqrt{\frac{\pi}{n_r a^2}}\left[U_0 - (E_{sq} - E_{tr})\right], \tag{4.32}$$

which is depicted as curve 4 in Fig. 4.4. In reality, before such domains appear in the square phase, it is already disturbed by rows of the half-pinned lattice, so that curve 4 does not describe properly such a transition. The same is true for the curve 3 which describes the transition from the half pinned to the deformed triangular lattice. In other words, curves 3 and 4 must intersect.

From the obtained phase diagram we see that the disordering of the square pinned lattice in the limit of weak pinning always occurs in two steps. First, some rows of vortices depin and form reconnected elastic chains; their concentration increases with the increase of random pinning strength U_r. At higher values of U_r, elastic domains of deformed triangular lattice proliferate in the system leading to a complete disordering of vortex array. If we start from the half pinned lattice, two scenarios are possible. If the regular pinning strength U_0 is relatively low, then the order is destroyed in one step due to the proliferation of domains of the deformed triangular lattice. If U_0 is relatively high, again a two-step disordering can take place. As a first step, an admixture of the square pinned lattice appear in the system, and as a second step, domains of a deformed triangular lattice depin the vortex lattice from the regular pinning array. Note that in experimental work [110] on macroscopic charged balls on a square array of traps, the formation of domains in the lattice of these balls was also observed. Although there was no artificial randomness in the experimental setup, the disorder was certainly unavoidable. Since energies of three relevant vortex phases, namely, triangular, pinned, and

half-pinned ones, are quite close to each other, domains formation can be observed in such experiments.

In Sec. 4.2, we also have described a quasi-1D type of defects, which destroy the order in vortex positions within the same row, see Fig. 4.2(c). The typical area of such a defect is $\sim l_{1D}a$, where l_{1D} is given by Eq. (4.22). The energy of the defect is defined in Eq. (4.23). Thus, for U_r leading to the generation of quasi-1D defects we get

$$U_r \sim \frac{2}{\sqrt{a}} \frac{2\pi}{\kappa^2} \left(U_0 - \frac{4\pi}{\kappa^2} e^{-2\pi} \right)^{3/4} \left[K_0(a) + \frac{K_1(a)}{a} \right]^{1/4}. \tag{4.33}$$

Our estimates show that, for realistic values of the parameters, U_r could become larger than the values corresponding to the phase boundary depicted by lines 2 and 3. This conclusion is due to the fact that quasi-1D defects represent an intermediate case between the collective pinning of vortices and a regime of single-vortex pinning at high pinning strengths. The vortex lattice in this case is still an elastic media, with the vortex-vortex interaction being important in the total balance of the energies. The phase boundary corresponding to such a transition is plotted in Fig. 4.4 as line 5. Since quasi-1D defects destroy the order in the vortex positions in the same row, a mixture of pinned and half-pinned phases in this case is also characterized by the absence of such an order in the rows of unpinned vortices; moreover, chains of unpinned vortices are now not necessarily reconnected. In this sense, the difference between the quasi-1D disordered phase and a mixture of pinned and half-pinned states is smeared out.

One can expect that the final regime with sufficiently high U_0 corresponds to zero-dimensional defects, when vortices are depinned individually that is known as the single-vortex pinning regime. Thus, the dimensionality of typical defects leading to the destruction of the order is decreasing continuously from 2 to 0 when the regular pinning strength U_0 is increasing. At low U_0, regularity in the vortex positions is destroyed by the appearance of reconnected elastic chains of collectively-depinned vortices that are ordered within each chain. At higher U_0, these chains start to be open, they should become straighter and, therefore, one can expect neighboring chains to connect due to the lack of free space. If we again increase U_0, chains become quasi-one dimensional elastic rows of finite length, as we have shown schematically in Fig. 4.2(c). Finally, we are in a single-pinning regime, when each vortex is pinned individually, that can be interpreted as chain shrinking towards a single lattice period, since the chain length given by Eq. (4.22) decreases with the increase of regular pinning strength.

So far only limiting cases of the first stage of vortex lattice disordering have been considered, namely, when we have: (i) reconnected chains, i.e., two-dimensional collective defects, (ii) quasi-one-dimensional stripe-like collective defects, (iii) quasi-zero-dimensional individual defects in the regime of a single-vortex pinning. To have a deeper insight into the problem and to understand better how these defects evolve, we perform molecular dynamics simulations

for the regime intermediate between the weak and strong pinning regimes. In Figs. 4.5-4.8 we present typical vortex patterns corresponding to an increasing strength of the random pinning potential U_r with a constant concentration of random sites, which is set equal to the concentration of regular pins. The initial state of the system (i.e., without random pinning) is a square lattice of vortices pinned on regular pins. A simulation region with the sizes 20×20 λ contains an array of 20×20 regular pinning arrays and 400 vortices. We use periodic boundary conditions at the boundaries of the simulation region. The value of U_0 is $0.045 \times 2\pi/\kappa^2$, whereas the vortex-vortex distance is 1 in units of λ. This value of U_0 is several times larger than that required for the transition from the square phase to the half-pinned state, i.e., we are indeed in the intermediate regime, where both reconnected and open chains of depinned vortices are expected to appear in the system with increasing U_r. This is exactly what we see in Fig. 4.5 at $U_r = 0.72U_0$, which contains both types of chains, and still there is no domains of a deformed triangular lattice. In general, these elastic chains are packed into finite fractal-like structures with a quasi-self-similar topology and dimensionality between 1 and 2. The building blocks of these fractals are represented by parts of rectangles of discrete sizes (i.e., commensurate with the period of the pinning array). If we increase U_r, as in Fig. 4.6 for $U_r = 0.85U_0$, domains of deformed triangular lattice start to appear in the system, and thus they coexist with chains of unpinned vortices. However, these domains somehow suppress the networks of depinned vortices by simply cutting them, since there is a competition between these two kinds of defects for a free space in the system. Further increasing U_r leads to the increase of the concentration of domains of totally depinned vortices, as indicated in Fig. 4.7 at $U_r = 1.28U_0$. It is interesting to note that domains of pinned square vortex lattice turn out to be rather robust with respect to the random pinning; some of them survive up to quite large values of U_r, several times greater than that corresponding to the situation shown in Fig. 4.7, with the fraction of pinned vortices decreasing slowly with increasing U_r. Fig. 4.8 shows the final state with quite high value of $U_r = 5.3U_0$, when almost all the vortices are depinned from the regular pinning array and there is no correlation between the positions of the regular pins and vortices, but there is a pronounced correlation between the positions of the vortices and random pins. Note that typical values of U_r leading to the generation of defects are in good qualitative agreement with our analytical predictions.

We also performed simulations for even higher U_0. We found that indeed the initial defects turn out to be quasi-one-dimensional stripes with the characteristic length of few lattice periods, rather than long-length and branched structures. Other defects found correspond to higher values of U_r, and they are more similar to a single-particle imperfections than to regions of elastically distorted media, which are constructed of many interacting particles. In fact, these defects correspond to domains of totally depinned vortices described above, in the limiting case of a single-vortex pinning. Finally, single-vortex defects and stripe-like defects also match, when the length of the stripes tends

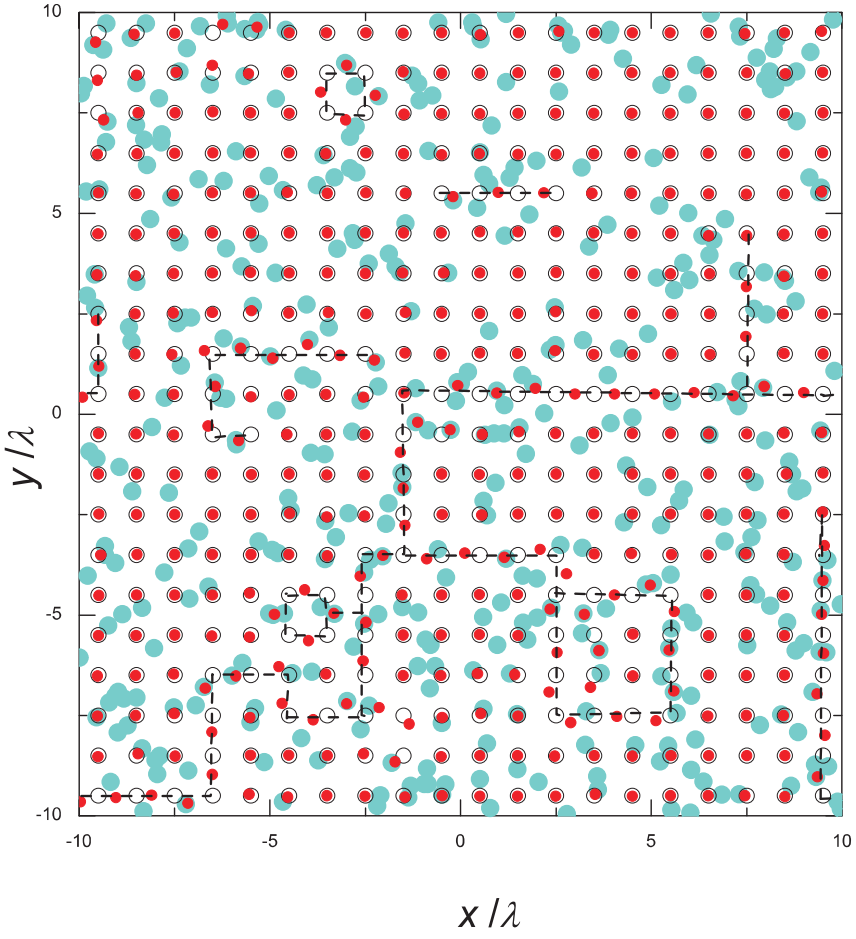

Fig. 4.5 Vortex pattern in the film with regular square and random pinning arrays for $U_r = 0.72U_0$, obtained in molecular dynamics simulations. Dashed lines are guides for eyes indicating positions of chains of unpinned vortices. Irregular blue (light gray) spots represent positions of random pins, red (dark gray) filled circles show positions of vortices, and regular black open circles correspond to periodic pins.

to a one lattice period. A general qualitative picture of the evolution of defects is presented in Fig. 4.9.

Thus, the molecular dynamics simulations enable us to relate defects of various dimensionalities and to better understand their evolution.

In conclusion, in this chapter, we studied theoretically the effect of disorder on vortex lattices in the presence of a regular square array of pinning sites. We considered a two-dimensional system with the same concentration of regular pinning sites and vortices, i.e., with filling factor 1. We were mostly

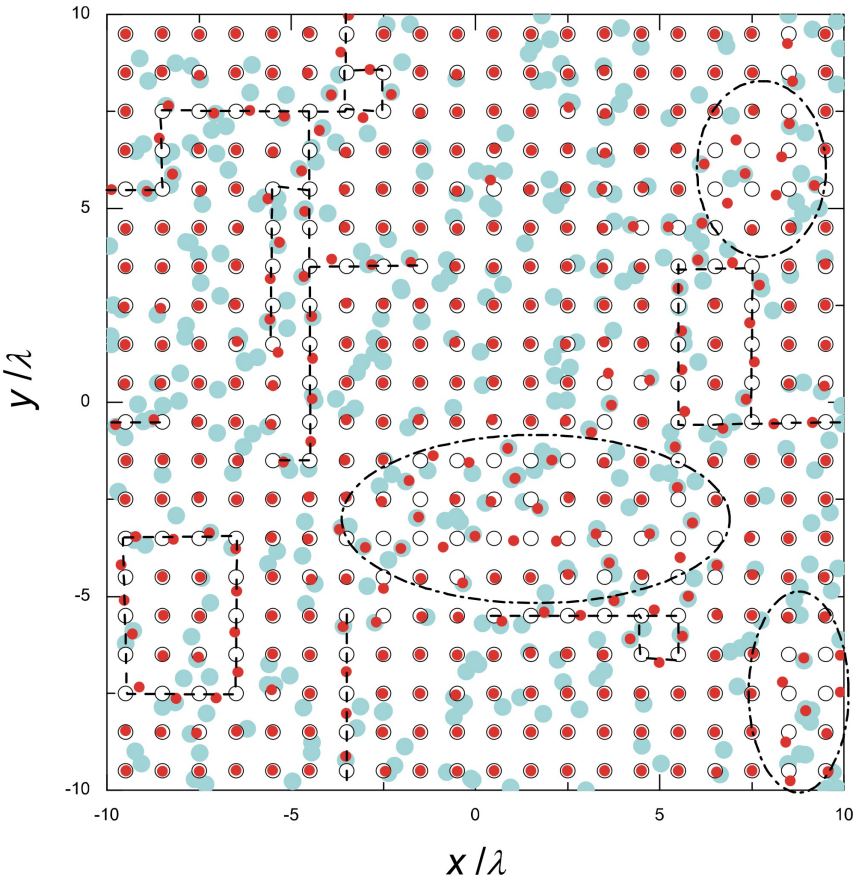

Fig. 4.6 Vortex pattern in the film with regular square and random pinning arrays for $U_r = 0.85U_0$, obtained in molecular dynamics simulations. Dashed lines are guides for eyes indicating positions of chains of unpinned vortices. Dash-dotted lines show borders of domains of deformed triangular lattice which is depinned from the underlying regular pinning array. Irregular blue (light gray) spots represent positions of random pins, red (dark gray) filled circles show positions of vortices, and regular black open circles correspond to periodic pins.

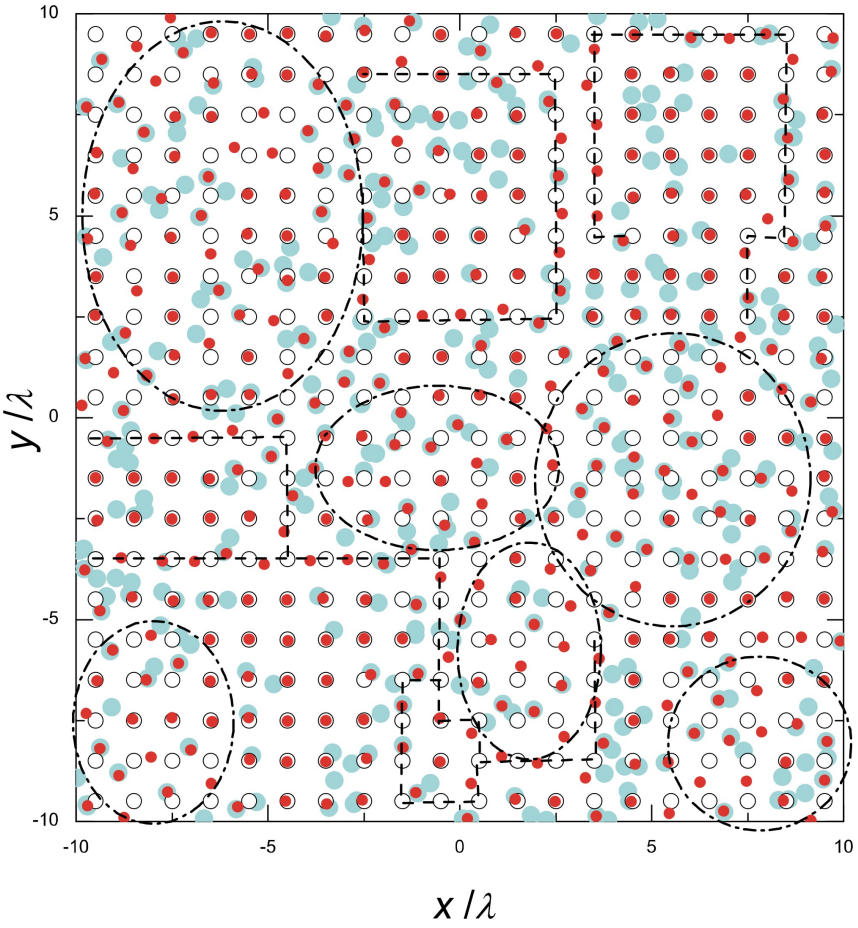

Fig. 4.7 Vortex pattern in the film with regular square and random pinning arrays for $U_r = 1.28U_0$, obtained in molecular dynamics simulations. Dashed lines are guides for eyes indicating positions of chains of unpinned vortices. Dash-dotted lines show borders of domains of deformed triangular lattice which is depinned from the underlying regular pinning array. Irregular blue (light gray) spots represent positions of random pins, red (dark gray) filled circles show positions of vortices, and regular black open circles correspond to periodic pins.

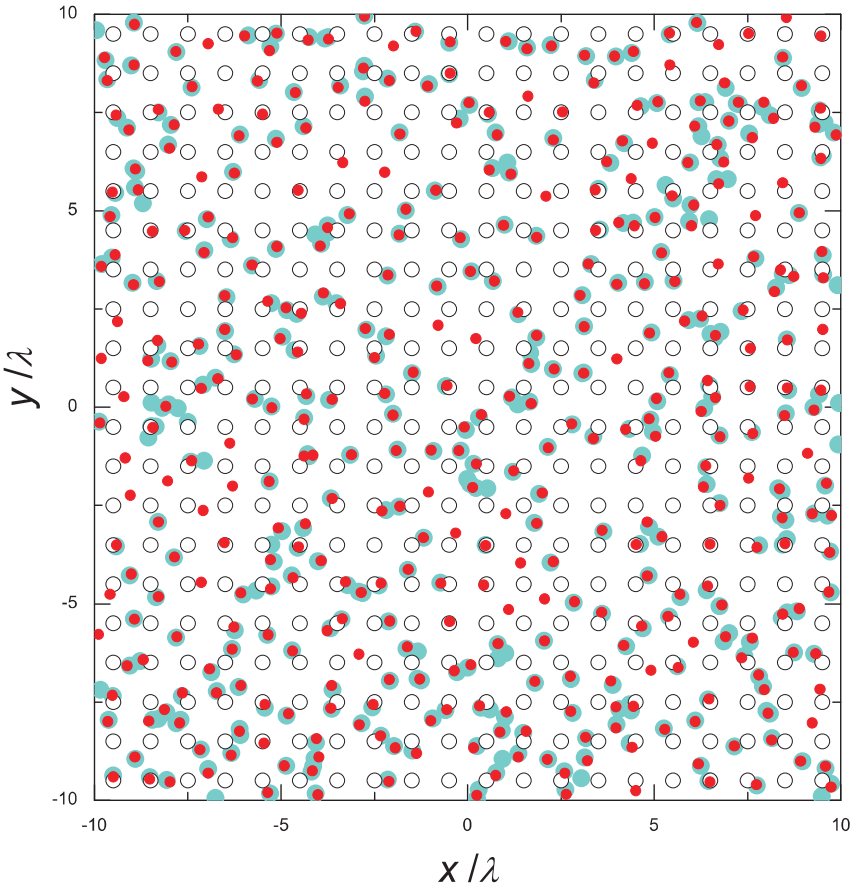

Fig. 4.8 Vortex pattern in the film with regular square and random pinning arrays for $U_r = 5.3U_0$, obtained in molecular dynamics simulations. Irregular blue (light gray) spots represent positions of random pins, red (dark gray) filled circles show positions of vortices, and regular black open circles correspond to periodic pins.

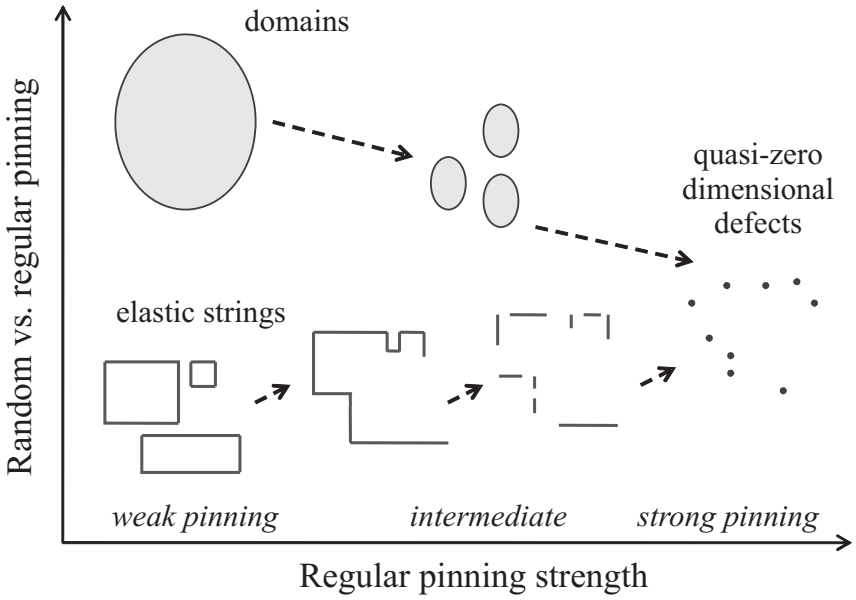

Fig. 4.9 General picture of the evolution of disorder-induced defects for square pinned vortex lattice. Lower branch corresponds to the elastic strings of collectively depinned vortices. First, they appear as reconnected chains. Then chains break and straigthen. As a result, they start to overlap and form fractal-like clusters. Finally, they decay to quasi-one-dimensional stripes, which shrink gradually to quasi-zero-dimensional individual defects corresponding to the single-pinning regime. Upper branch shows the evolution of higher-energy elastic defects, which form domains of vortices collectively depinned from regular pins. These domains break into uncorrelated blocks of smaller sizes and finally also shrink to quasi-zero dimensional defects thus matching with the lower branch of defects.

focused on a weak pinning regime, when vortex lattice demonstrates collective properties due to the mutual repealing of vortices. The resulting structure of the vortex lattice is determined by the competition between the square symmetry of the regular pinning array, by the triangular symmetry imposed by the vortex-vortex interaction, and by the action of randomness trying to destroy the order in vortex positions. Typical defects of vortex lattices have been identified for some limiting and therefore simple cases and their energies and sizes have been estimated analytically. Molecular dynamics simulations were also used for exploring regions on phase diagram, which are difficult to approach in an analytical way. Topological defects found are of various dimensionalities including fractional ones having fractal-like structure. We were able to predict analytically two limiting cases of these fractal-like structures: a reconnected chain of unpinned vortices and a straight stripe-like defects, while molecular dynamics simulations allowed us to reveal the connection between these limits.

We then constructed an approximate phase diagram of the system in the plane of random and regular pinning strengths. We found that disordering of the regularity in vortex positions can occur either in one or two steps depending on the strength of the regular pinning potential. In the former case, domains of deformed triangular lattice start to appear spontaneously in the film. In the latter case, in the beginning, reconnected chains of unpinned vortices are generated inside a square lattice (or the opposite: chains of pinned vortices appear inside the half-pinned phase), and only after that again domains of deformed triangular lattice depin the vortex lattice as a whole from the regular pinning array. Both chains and domains are elastic defects with interacting vortices depinned collectively.

We also analyze an intermediate regime for values of regular pinning strength, which are between the regimes of collective and single-vortex pinning. In this case, the first step of disordering occurs by proliferation of opened, not reconnected, elastic chains of depinned vortices, which can form long fractal-like defects with complicated quasi-self-similar topology. Fractals appear due to the process of opening of reconnected chains and their straightening, when different chains start to connect to each other. At the same time, the average length of these defects is going to decrease with the increase of regular pinning strength due to a periodic potential sharpening, so that there is a competition between two tendencies. As a result, chains become straighter and relatively short thus forming quasi-one-dimensional stripes. Finally, for high values of periodic pinning strength, they shrink continuously towards a quasi-zero-dimensional defects corresponding to a single-pinning regime. The latter regime is characterized by one-step disordering, i.e., the width of the region on the phase diagram with coexistent chains of unpinned vortices and domains of totally depinned vortices has to vanish with the growth of regular pinning strength, since these two types of defects also match. Thus, we can understand on the same footing all the regimes of disordering starting from a collective pinning to a single-vortex pinning.

Our results are applicable not only to vortices in superconductors, but also for a broader class of physical systems containing a large number of repealing objects and underlying system of traps: for instance, vortices in ultracold gases in optical lattices, colloids, macroscopic elastic balls interacting via Coulomb forces, charge and spin density waves.

Appendix

Let us assume that for a square pinned lattice, an infinite kink can have a smooth structure and is directed along the y axis (x and y axes are directed like in Fig. 4.1(c)), thus separating two regions of vortex lattices shifted by a in y direction with respect to each other, as for usual sine-Gordon systems [31]. We also denote kink's length along x as l_{2D} ($l_{2D} \gg a$). There are $l_{2D}/a \gg 1$ vortex rows within the kink's length and we denote deviations of vortices in the n's row along the y direction as u_n. We also restrict ourselves to lattices with vortex-vortex distances of the order of the penetration depth λ ($a \sim 1$ in dimensionless units). In this case, the dominant contribution to the interaction energy of a given vortex with all other rows of vortices is provided by harmonics with $m = 0, \pm 1$, as can be seen from the exponent in the RHS of Eq. (4.2). This energy is then given by

$$E_n \simeq \frac{(2\pi)^2}{\kappa^2 a}\frac{e^{-a}}{1-e^{-a}} + \frac{2\pi}{\kappa^2}e^{-2\pi} \times \left[\cos\left(\frac{2\pi(u_{n+1}-u_n)}{a}\right) + \cos\left(\frac{2\pi(u_n-u_{n-1})}{a}\right)\right]. \tag{A1}$$

Now we can expand the RHS of Eq. (A1) in terms of $\Delta u_n/a$. To find the energy of the kink, we have to sum the contributions from all the rows within the kink. But instead it is convenient to switch from summation to integration with the simultaneous exchange of $\Delta u_n/a$ by $\frac{du}{dx}$, i.e., to use a continuous limit and introduce smoothly varying deformation field of the vortex lattice. This method is applicable for sine-Gordon systems [31], and we repeat the same arguments for the system at hand. Finally, for the u dependent part of the vortex-vortex energy of the kink (per length of the kink in y direction), we have:

$$E_{kink}^{(vv)} = -\frac{(2\pi)^3}{\kappa^2 a^2}e^{-2\pi}\int\left(\frac{du}{dx}\right)^2 dx. \tag{A2}$$

The derivative $\frac{du}{dx}$ can be estimated as $\frac{du}{dx} \approx \frac{a}{l_{2D}}$, and this leads us to the following expression

$$E_{kink}^{(vv)} \approx -\frac{(2\pi)^3}{\kappa^2}e^{-2\pi}\frac{1}{l_{2D}}. \tag{A3}$$

There is also a contribution to the kink energy coming from the regular pinning potential. It appears due to the fact that vortex rows within this kink are depinned. In the limit of small potential wells, $\sigma \ll a$, this energy (per length of the kink in y direction) is given by

$$E_{kink}^{(vp)} \approx U_0\frac{l_{2D}}{a^2}. \tag{A4}$$

For the total energy of the kink we thus have

$$E_{kink} = E_{kink}^{(vv)} + E_{kink}^{(vp)} \approx -\frac{(2\pi)^3}{\kappa^2}e^{-2\pi}\frac{1}{l_{2D}} + U_0\frac{l_{2D}}{a^2} \tag{A5}$$

If we now try to minimize the kink energy given by Eq. (A5) with respect to kink's length, we immediately see that $l_{2D} = 0$ is the lowest energy solution. Of course, in reality l_{2D} cannot be shorter than a, and $l_{2D} = a$ is a true solution. This conclusion is based on the physical fact that a square lattice of free interacting vortices is unstable in the absence of pinning, leading to a *negativeness* of "elastic constant", in contrast to the sine-Gordon and related systems [31].

Chapter 5

Kink-antikink vortex transfer in periodic-plus-random pinning potential*

In **Chapter** 4, we studied the static vortex states in superconductors with both regular and random pinnings. The aim of the present chapter is to investigate the vortex dynamics in similar system in **Chapter** 4 to reveal correlations between the static defects and the dynamical regimes under an external drive [163].

5.1 Model and simulation

The model of this chapter is just a modification of the one in **Chapter** 4 by adding an external driving force $\mathbf{F}_d$ (i.e., a Lorentz force created by an applied current), which is directed along one of the principle axes of the square pinning array. The analytical approach is also similar, which is based on the fact that in various configurations most of the vortices remain pinned, so that the vortex transfer occurs through collective defects that can be described reasonably well by just few parameters.

* This chapter is based on the following publication:
[1] W. V. Pogosov, H. J. Zhao, V. R. Misko, and F. M. Peeters, Phys. Rev. B **81**, 024513 (2010).

5.2 Dynamical regimes

In order to reveal various dynamical regimes in the weak disorder limit, we carry out numerical experiments and supplement them by the theoretical analysis. The characteristic quantity, which enables us to distinguish between different regimes, is the average vortex velocity $\langle v \rangle$ in the direction of the driving force $\mathbf{F}_d$, as a function of $F_d = |\mathbf{F}_d|$. Averaging is performed both among all the vortices in the system and over time, after the steady flow is achieved. In general, the smaller the number of depinned and flowing vortices the larger the average vortex velocity. Thus this quantity is similar to the dynamical order parameter that can be defined as a fraction of depinned and moving vortices.

Below we present our results for the following set of parameters: the lattice period for regular pins $a = \lambda(T)$, $\sigma_{reg} = 0.15a$, $\sigma_{ran} = 0.2a$, $f_{reg} = 0.6\Phi_0^2/8\pi^2\lambda(T)^3$, the number of regular and random sites being the same. These results are rather generic with respect to the variation of main parameters, until conditions σ_{ran}, $\sigma_{reg} \ll a \sim \lambda(T)$ are fulfilled. The value of f_{reg} is chosen in such a way that it allows us to describe the most interesting region of the phase diagram that corresponds to intermediate regular pinning strengths. As shown in **Chapter** 4, in this regime and for a weak disorder, static defects of pinned square vortex lattice consist of clusters containing elastic chains of depinned vortices. Our simulations show that until we are in the intermediate regime, variations of f_{reg} do not lead to qualitative changes in the dynamical regimes.

Typical driving dependences of the average vortex velocity are presented in Fig. 5.1, where one can clearly see three distinct dynamical regions for the case of a weak disorder (curves 1 and 2), while for stronger disorder they are smeared out due to chaotization (curve 3). We associate these different regions with different dynamical regimes of vortex lattice motion. These $\langle v \rangle$-F_d curves of course are sensitive to the particular realization of disorder. However, we found that in general the shape of the curve, that is characterized by three different regions, is quite robust with respect to different realizations of disorder, except of some special cases, which are discussed below. The characteristic values of driving force for the crossover regions between different regimes are also rather reproducible, while absolute values of average vortex velocity can vary.

5.2.1 Regime-I: depinning of stripes

Very weak driving results in no vortex motion (pinned regime). If the driving force F_d reaches some threshold value $F_d^{(I)}$, part of vortices start to move. An analysis of vortex patterns shows that vortex motion is not individual, since vortices travel collectively in a soliton-like manner, being localized within vortex rows [164]. Moving collective structures are just depinned kink and

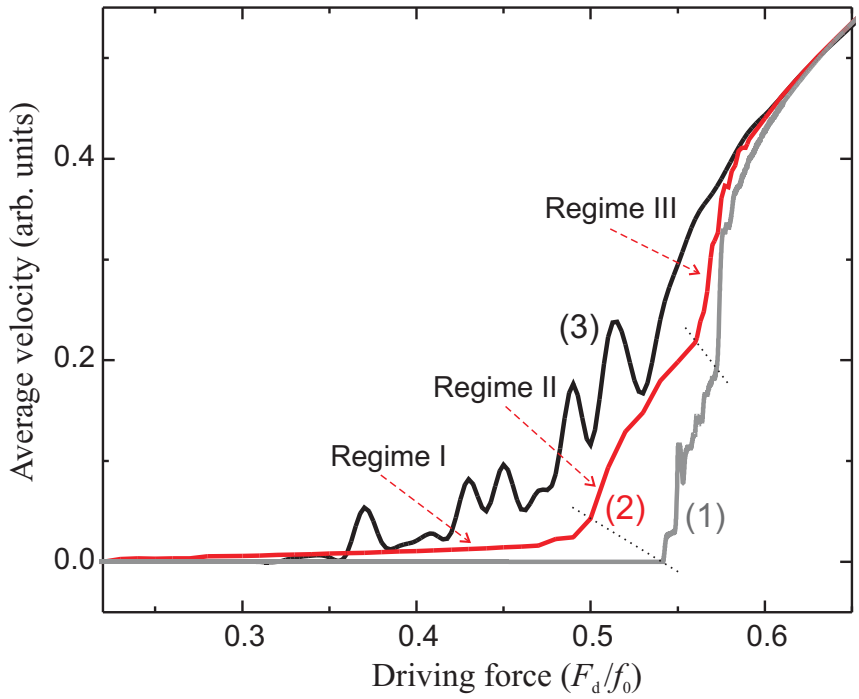

Fig. 5.1 The average vortex velocity as a function of driving for different values of the random pinning force: $f_{rand} = f_{reg}/6$ (curve 1), $f_{reg}/3$ (curve 2), $f_{rand} = f_{reg}/2$ (curve 3). Black dotted lines show the transitions (crossovers) between different dynamical regimes.

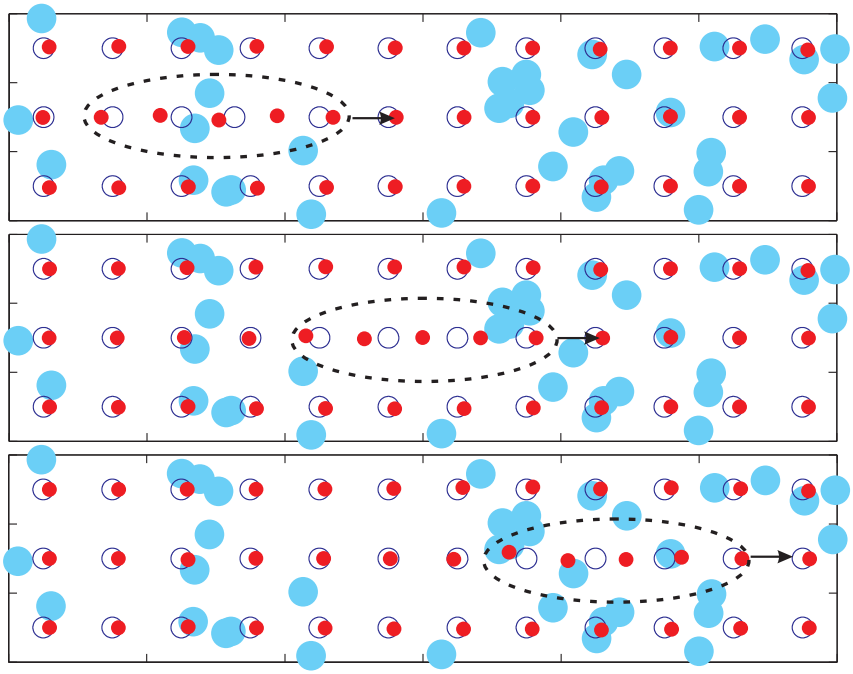

Fig. 5.2 Motion of the stripe shown by three snapshots. Irregular blue (light gray) spots represent positions of random pins, red (dark gray) filled circles show positions of vortices, and regular black open circles correspond to periodic pins. Dashed lines are guides for eyes indicating positions of defects, arrows show the direction of their motion.

antikink defects (stripes) earlier predicted for static configurations in **Chapter** 4. Such a defect consists of a finite-length chain of depinned vortices, whose length depends on f_{reg}, this length being much larger than a in the regime of intermediate strength of the regular pinning potential. The defects contain either one extra vortex (kink) or one vacancy (antikink). Kinks move in the direction of an applied force, so they represent "compression waves" in vortex rows, as seen in Fig. 5.2. Vacancy-based antikinks flow in the opposite direction; they can be considered as "decompression waves".

In order to understand why the dynamical threshold is associated with the depinning of kinks, let us first analyze the structure of a static kink. Kink appears due to an additional vortex in a particular region of the system. Because of the vortex-vortex repulsion, it displaces other vortices within one row from their pinned positions, while vortices in all other rows remain pinned, i.e., one-dimensional deformation field of a vortex chain changes by a along the kink. In the limit of narrow regular pins, $\sigma_{reg} \ll a$, one can assume that vortices in a kink are completely depinned, whereas all other vortices in the

same row are pinned, as well as vortices in other rows. The total energy of the kink compared to the unperturbed system is thus given by the sum of three contributions, E_1, E_2, and E_3. The first term, E_1, is due to the energy gained by each of D depinned vortices. Before the depinning, each of these vortices was located in the potential well of the depth $U_{reg} = f_{reg}\sigma_{reg}/2$. After the depinning, its energy became nearly equal to the average regular pinning energy within the row, $-\frac{4\sigma_{reg}}{3a}U_{reg}$. Thus, E_1 is given by

$$E_1 \approx \frac{f_{reg}\sigma_{reg}}{2}\left(1 - \frac{4\sigma_{reg}}{3a}\right)D. \tag{5.1}$$

The second term, E_2, is an energy decrease due to the interaction with vortices from the surrounding pinned vortex rows. If we are far enough from the threshold of the transition to the half-pinned phase [100, 102, 107, 108], i.e., in the intermediate regime of pinning strength, this contribution is sufficiently smaller than E_1.Therefore, in the leading order, we can assume that positions of depinned vortices in the row are not correlated with the minima of the potential interaction with surrounding rows, so that the term E_2 can be easily found from Eq. (4.2) by averaging over these positions:

$$E_2 \approx -\frac{\Phi_0^2}{8\pi^2\lambda(T)^2}e^{-2\pi}D. \tag{5.2}$$

The third contribution, E_3, is associated with the increase of the vortex-vortex interaction energy within the row, where the kink is localized, this increase being caused by one excess vortex. Under assumptions of the elasticity theory, one can take into account only interaction between nearest neighbors in the row, from which it follows that distances l between nearest vortices inside the kink are all the same, $l = Da/(D+1)$. By summing the energies of the vortex-vortex interaction, we obtain a D-dependent part E_3 of the corresponding contribution to the energy of the kink, which, in the leading order in a/D, is given by

$$E_3 = \frac{\Phi_0^2}{8\pi^2\lambda(T)^3}K_1\left[a/\lambda(T)\right]\frac{a}{D}. \tag{5.3}$$

The optimal number of vortices in the kink D now can be found by the minimization of $E_1 + E_2 + E_3$:

$$D \approx \left\{\frac{a}{\lambda(T)}\frac{\frac{\Phi_0^2}{8\pi^2\lambda(T)^2}K_1\left(\frac{a}{\lambda(T)}\right)}{\frac{f_{reg}\sigma_{reg}}{2}\left(1 - \frac{4\sigma_{reg}}{3a}\right) - \frac{\Phi_0^2}{8\pi^2\lambda(T)^2}e^{-2\pi}}\right\}^{1/2}. \tag{5.4}$$

For the used values of parameters, we obtain $D \approx 4 - 5$, while in numerical simulation we found that $D \approx 5 - 6$, so that our analytical approach provides a quite good estimate.

If we now suddenly turn on an applied force F_d acting on each vortex, the net external force acting on the whole kink is DF_d. At the same time, the

force of resistance is due to the fact that the first and last vortices in front and behind the kink are pinned, and thus the maximum resistance force is $2f_{reg}$. By equating the external force to the force of resistance, we obtain a simple condition for the depinning of the kink:

$$F_d^{(I)} \approx \frac{2f_{reg}}{D}. \tag{5.5}$$

Decoupling of kinks from the underlying pinning array signals as an increase of the average vortex velocity, which is used here as an indicator for distinguishing between different dynamical regimes. In experiments, such a decoupling would result in the increase of sample's resistance, since vortex motion in superconductors is associated with dissipation. Notice that Eq. (5.5) can be also obtained by considering a balance of the forces, acting on each vortex in the kink, one vortex in front of the kink, and one vortex behind it, and then by summing up these forces. An alternative approach is to use a continuum approximation for the one-dimensional Frenkel-Kontorova model [31], from which one can deduce a deformation field for the vortex chain inside the kink caused by external driving and then equate to f_{reg} the pressure this row exposes on the first or the last pinned vortex along the kink. Eq. (5.5) demonstrates that, in the large D limit, the stripe behaves nearly as a *rigid* body containing D particles. This is the explanation why it is depinned at relatively low driving forces, i.e., significantly smaller than f_{reg}. This rigidity is linked to the fact that regular potential is weak and that is why kink is much longer than a: it is favorable that an excess vortex depins many other vortices in the row. Therefore, vortex chain deformations under an external drive remain small until kink is pinned, resulting in nearly periodic locations of vortices inside it. Eq. (5.5) implies that $F_d^{(I)}$ is very sensitive to the kink's length, which in turn depends on the regular pinning potential. The tendency is that, the stronger regular pinning the shorter kinks and antikinks, so that in the limit of strong pinning one reaches the regime when defects are no longer collective. The analysis of this limit, i.e., when the vortex-vortex interaction does not play an important role anymore, is beyond the scope of the present work.

The results obtained by using Eqs. (5.4) and (5.5) are in a good semi-quantitative agreement with results of our numerical simulations: depinning of stripes is predicted to occur at $F_d^{(I)} \approx 0.48 f_{reg}$ for the set of parameters we used, while in the numerical simulations this value was ranged between $0.30 f_{reg}$ and $0.42 f_{reg}$, for a weak random pinning strength and in different trials. Note that in the particular initial configuration shown in Fig. 5.1 by curve 1, there was no preexisted stripe in the simulation region, which is reflected by the absence of any current up to the dynamical regime-II. This is an example of how different realizations of disorder in our finite-size simulations can lead to different results. The smaller the system the higher the probability that there are no preexisted kinks. However, in the infinite system these defects have a finite concentration and therefore regime-I always exists.

In general, the main requirement for the determination of dynamical regimes in the studied system is that the simulation region has to be significantly larger than the length of a single kink/antikink, since the dynamics is controlled by kinks and antikinks. This condition is justified in our simulations.

In our numerical experiments, we found that kinks and antikinks always disappear when they collide. A similar process, known as kink-antikink annihilation, was studied in Ref. [165] within the sine-Gordon model applied for spatially inhomogeneous media with dissipation and under an external drive, i.e., essentially the conditions realized in our simulations. Another remarkable but quite rare process, in a weak disorder regime, is kink sticking by bunches or voids of random pins. These two processes lead to a decay in time of the total current. Fig. 5.3 shows typical time dependences of the current, where two processes are addressed: (i) when kinks and antikinks annihilate (curve 1), and (ii) when they persist (curve 1'). It is obvious, however, that in infinite systems all the kinks and antikinks have to disappear, since the total number of kinks and antikinks in the single row is the same. Nonvanishing and stable motion in the weak disorder regime thus appears as an artifact of a finite-size simulation region with periodic boundary conditions.

Although the vortex transfer is associated with the depinning of preexisted kinks and antikinks, static defects in the weak and intermediate disorder regimes consist not only of these defects. Kinks and antikinks can be just parts of clusters. One can naively expect that these clusters act as easy-channels for the vortex transfer. Instead, low driving partially "heals" such defects. The reason is that clusters basically consist of two types of segments. Segments of the first kind contain no vacancies or excess vortices, in contrast with segments of the second type, which are nothing but stripe-like defects. For low driving, vortices inside segments of the first kind move collectively to their nearest vacant pins. Such a delicate healing, however, is not possible for segments of the second type, which contain excess vortices or vacancies. Therefore, stripes do persist in the sample, while low driving leads to the fragmentation of clusters. A typical driving force, which heals such defects, can be estimated by considering the limiting case of an infinite chain of depinned vortices. An effective pinning force for vortices from the chain is created by interactions with surrounding rows of pinned vortices. From Eq. (4.2), it is straightforward to obtain the following estimate:

$$F_d^{(h)} \approx \frac{\Phi_0^2}{4\pi\lambda(T)^2 a} e^{-2\pi}. \tag{5.6}$$

In the regime of intermediate regular pinning strength, $F_d^{(h)}$ is much smaller than $F_d^{(I)}$. We will show, however, that $F_d^{(h)}$ plays an important role in the dynamical regimes appearing for higher F_d. Note that the effect of reentrance of square pinned lattice under a weak external drive was revealed in Ref. [102] for the half-pinned phase (in the absence of disorder). This feature

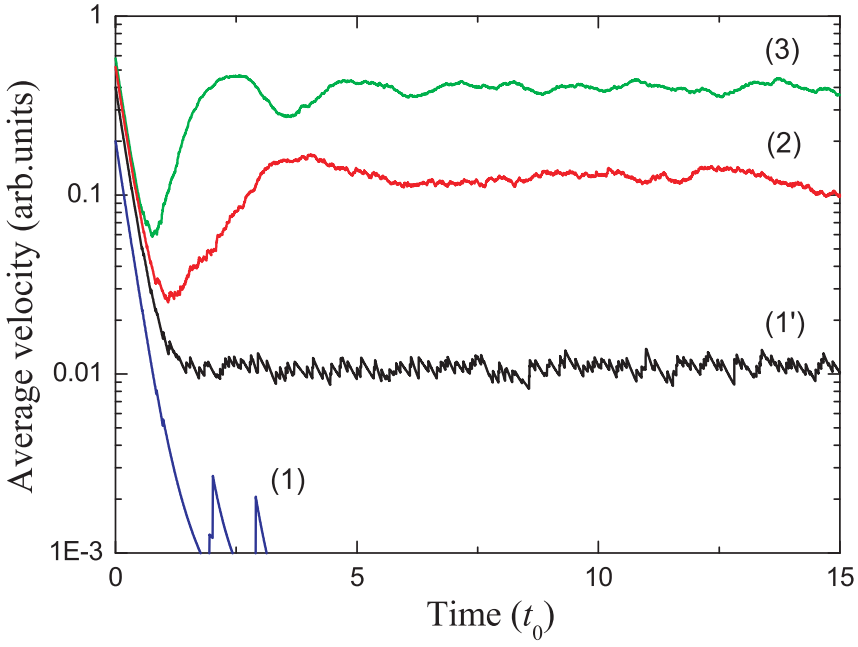

Fig. 5.3 (Color online) Time dependence of the average vortex velocity for different dynamical regimes at $f_{rand} = 0.2$. Here $t_0 = 4\pi^2\lambda(T)^4\eta/\Phi_0^2$. Curves 1 and 1' correspond to regime I at $F_d = 0.4$ and 0.2, respectively. Curves 2 and 3 show regimes II and III for $F_d = 0.52$ and 0.57, respectively.

is consistent with the present results, since chains of depinned vortices are nothing but nuclei of this phase.

As mentioned above, here we consider only the case of the first matching field, when the density of vortices and regular pins are exactly the same. It is, however, clear that small differences between these densities would lead to the appearance of additional kinks or antikinks in the static configuration, such that their numbers will be also different from each other. From that, one can conclude that regime-I (as well as other regimes) will be preserved, although motion of kinks and antikinks will be nonvanishing.

5.2.2 Regime-II: generation of kink-antikink pairs

Now we discuss the origin of the second cusp in curves 1 and 2 of Fig. 5.1, which corresponds to the dynamical regime-II. We found by numerical simulations that, when driving approaches some critical value $F_d^{(II)}$, kink-antikink pairs appear spontaneously from time to time [164]. New kinks move in the direction of the drive, whereas antikinks propagate in the opposite direction. Because of the intensive generations of new kinks and antikinks, the average current increases significantly compared to regime-I, as seen from Fig. 5.3. Most of the pair generation events are triggered by already excited and moving stripes, which create an additional washboard drive acting on the adjacent rows. Therefore, new kink-antikink pairs appear in the rows adjacent to the row with a moving kink, as shown in Fig. 5.4 by three snapshots: one of the vortices is depinned, then it creates an area of vortex row compression in front and the area of decompression behind, these two areas being transformed into the kink-antikink pair. It is easy to realize that the amplitude of this additional periodic drive is equal to $F_d^{(h)}$ in the limit of long kinks ($D \gg 1$), so the total effective driving in the row, adjacent to the moving stripe, is $F_d^{(eff)} \approx F_d + F_d^{(h)}$. However, in some trials there were no preexisted kinks within a simulation region (see, for instance, curve 1 in Fig. 5.1), but kink-antikink pairs did appear by themselves in some "weak points", where vortices were additionally strongly displaced in the direction of the drive by random pins. Therefore, we conclude that, in regime-II disorder is the key factor of kink-antikink nucleation, while moving defects can assist to this process. Besides, the comparison with the numerical results shows that the value of $F_d^{(h)}$ is too low to explain the data for $F_d^{(II)}$ by only a washboard potential of moving stripes.

Let us now analyze how disorder can lead to the generation of kink-antikink pairs and estimate a minimum value of the driving force $F_d^{(II)}$ that triggers this process. We place a center of coordinates in one of the regular pinning sites with axis x being directed along the driving force. In the absence of disorder, this driving force shifts the pinned vortex to the point with coordinates $(r_0, 0)$, where $r_0 = \sigma_{reg} F_d / f_{reg}$. Moving kink or antikink in the adjacent rows leads to an additional displacement and the total amplitude

of the displacement can be estimated by changing F_d to $F_d^{(eff)}$. If we now take into account a disorder and neglect the vortex-vortex interaction within the row, random force in the point $(r_0,\, 0)$ must be nonzero in order to depin the vortex. This restricts possible locations of the random pin(s) acting on the vortex at $(r_0,\, 0)$: there should be at least one pin accommodated within the circle of radius σ_{ran} with the center at $(r_0,\, 0)$. Next, we assume that random force acting on this vortex is created by only one random pinning site, i.e., we neglect possible overlaps between random pins. This is a reasonable assumption (in the leading order in σ_{ran}/a) provided that $\sigma_{ran} \ll a$ and concentration of random pins is not very high, $n_{ran} \sim 1/a^2$. The optimal position for the pin, which minimizes $F_d^{(II)}$, is in the x-axis at $(\sigma_{ran} + r_0,\, 0)$. This condition implies that two criteria are satisfied: (i) the random force is nonzero at $(r_0,\, 0)$ and it is directed along the driving force, and (ii) at the edge of the regular pin, $(\sigma_{reg},\, 0)$, where the regular pinning force is maximum, the opposite random force, $f_{ran}(\sigma_{ran}+r_0-\sigma_{reg})/\sigma_{ran}$, is also maximum, *provided* that the criterion (i) is satisfied. This force together with the driving force $F_d^{(eff)}$ should compensate f_{reg} at the edge of the regular pin. From this we find the critical driving force $F_d^{(II)}$ that depins a given vortex

$$F_d^{(II)} \approx \frac{f_{reg} - f_{ran}\left(1 - \frac{\sigma_{reg}}{\sigma_{ran}}\right)}{1 + \frac{f_{ran}}{f_{reg}}\frac{\sigma_{reg}}{\sigma_{ran}}} - F_d^{(h)}. \tag{5.7}$$

Starting from $F_d = F_d^{(II)}$ one can find an area in the vicinity of each vortex, where a random pin can be positioned, such that it will depin this vortex (with the assistance of moving stripe in one of the two adjacent rows). In an infinite system for a finite concentration of random pins, the concentration of such weak points is also finite. Starting from higher drivings, $F_d \approx F_d^{(II)} + F_d^{(h)}$, kink-antikink pairs can be generated in weak points without an assistance of moving defects that agrees with the results of our numerical experiments. When deriving Eq. (5.7), we didn't take into account the mutual repulsion of vortices within the row, which acts against the depinning of a particular vortex. According to our estimates, such a resistance force is too small to noticeably change $F_d^{(II)}$, since $\sigma_{reg} - r_0 \ll \sigma_{reg}$. Eq. (5.7) is in a reasonably good agreement with our numerical results for a weak disorder. For instance, according to this equation, $F_d^{(II)}$ corresponding to curves 1 and 2 in Fig. 5.1 should be around $0.85 f_{reg}$ and $0.71 f_{reg}$, respectively, while in numerical experiments these quantities are around $0.89 f_{reg}$ and $0.78 f_{reg}$. Variation of these quantities from realization to realization of disorder was within few percent (provided that presence or absence of preexisted stripes was taken into account properly, when analyzing the data), except of some special cases. Among them, the most frequent was the situation when the number of preexisted kinks inside the simulation region was much higher than the average one, so that together they were able to produce locally larger washboard potential, which resulted in smearing out the dynamical regimes.

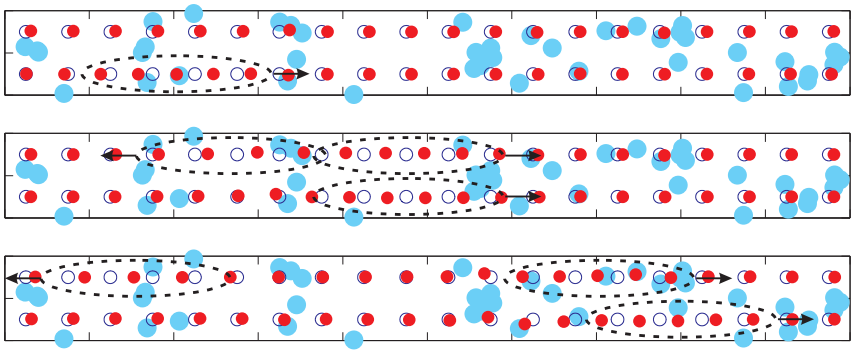

Fig. 5.4 (Color online) The same as Fig. 5.1 but with generation of kink-antikink pair by moving stripe, shown by snapshots. Initially kink flows in the bottom row, then it creates a kink-antikink pair in the upper row.

In the limit of a very weak disorder, Eq. (5.7) reduces to $F_d^{(II)} \approx f_{reg} - f_{ran} - F_d^{(h)}$, which clearly shows a competition between regularity and disorder, the latter factor being enhances by moving kinks through an additional term $F_d^{(h)}$. This condition is not sensitive to the particular form of the potential created by a single site, this fact reflecting the universality of the obtained criterion. Using similar geometrical arguments (but in two dimensions), we also found that above $F_d^{(II)}$, concentration of weak points grows as $\sim (F_d - F_d^{(II)})^{3/2}$, so that the generation of kink-antikink pairs is intensified.

We also notice that, due to a continuous generation of kink-antikink pairs, vortex motion within regime-II no longer decays in time, unlike for regime-I. The motion occurs via groups of kinks and antikinks travelling in the opposite directions and creating, from time to time, new defects. One of these defects joins the same group, whereas its counterpartner starts to flow in the opposite direction. In a steady flow regime, replication of defects has to be balanced with their annihilation, under collisions of individual kinks and antikinks or their groups.

5.2.3 Regime-III: free proliferation of kink-antikink pairs

We finally revealed third dynamical regime, which appears as the last region in curves 1 and 2 in Fig. 5.1, at drivings, which are already very close to the regular pinning force f_{reg}. In this regime, washboard drive produced by moving kink, is already strong enough to generate kink-antikink pairs freely without an assistance of the disorder. The corresponding driving is then

simply given by

$$F_d^{(III)} \approx f_{reg} - F_d^{(h)}. \tag{5.8}$$

In this regime, kink-antikink pairs start to proliferate very intensively being triggered by the motion of defects: preexisted kinks immediately generate kinks and antikinks; in turn, these defects create new pairs, and so on [164]. The area of vortex motion rapidly extends until it covers the whole simulation region. In regime-III, no "islands" are found, where domains of vortex lattice can be pinned for a long time. According to Eq. (5.8), $F_d^{(III)}$ is around $0.98 f_{reg}$, and this value is also in a reasonably good agreement with the numerical results, shown in Fig. 5.1 (approximately, $0.96 f_{reg}$ for curve 1 and $0.94 f_{reg}$ for curve 2, these results typically being reproducible within several percents).

Let us now briefly discuss the dynamics of vortices, when the disorder is no longer very weak, so that it not only triggers motion of defects, but also significantly affects it. The general tendency is that disorder smears out well-separated dynamical regimes, as seen from curve 3 in Fig. 5.1. Kinks and antikinks now can easily bend and jump from row to row. However, very surprisingly, soliton-like origin of the vortex transfer is extremely robust against the disorder, up to the regime of strong disorder, $f_{ran} \sim f_{reg}$. In the limit of the very strong disorder, $f_{ran} \gg f_{reg}$, vortex flow is localized in narrow streams, in which vortices flow one by one. Another mechanism of vortex transfer is pumping, when vortices are pushed into "traps", until their mutual repulsion breaks the blockade.

Note that here we analyzed the first-matching-field regime, while a little imbalance between the numbers of regular pins and vortices could serve as an additional source of disorder. As was shown in Refs. [92, 94], this imbalance results in different dynamical regimes including vortex flow in "incommensurate rows" and negative-differential-resistivity (NDR) parts of the VI-curve of N- [92, 94] and S-type [94]. Very recently, the first experimental observation of the N-type NDR phase has been reported [166]. (See also a related experiment [83, 167] on a triangular array of pins, where channeling of vortices can be suppressed by the random removal of pinning sites [168].)

In conclusion, in this chapter, we studied the competitive effect of periodic square and weak random pinning potentials on the dynamics of vortices in two dimensions. We found new dynamical regimes, which display themselves through distinct regions on the curves of average vortex velocity versus external driving force. There are three regimes, in which vortices move in a soliton-like collective structures travelling within individual vortex rows. These are kinks, each containing an excess vortex and moving in the direction of an external drive, and antikinks, flowing in the opposite direction and containing a vacancy. When colliding, kinks and antikinks annihilate. In the first regime, preexisted static kinks and antikinks decouple from the underlying pinning array and propagate in the system. In the second regime, moving defects excite secondary kink-antikink pairs in the adjacent rows in certain

weak points, which are more corrupted by disorder. In the third regime, these pairs are excited by moving kinks and antikinks freely, not only in weak points, due to their additional washboard potential. We presented analytical semi-quantitative estimates for characteristic values of driving forces leading to crossovers between the regimes, which are in a good agreement with our numerical results.

Although we have concentrated on vortices in superconductors, it is clear that similar dynamical regimes will be realized in other two-dimensional systems with square lattice potentials, containing repealing particles. Moreover, disorder-induced kink-antikink generation under an external drive can appear as a rather universal phenomenon, which exists for systems and lattice potentials of various dimensionalities.

Chapter 6

Pattern formation in systems with competing range interactions*

In this chapter, we investigate pattern formation of vortex states with non-monotonic vortex-vortex interaction, where we use a model competing range interaction potential, which is repulsive for short range and attractive for longer range [169, 170]. In principle, this form of the interaction potential could be used as a model for various systems with non-monotonic inter-particle interaction, e.g., atoms or molecules (i.e., the Lennard-Jones potential), or vortices in two-band superconductors, depending on specific parameters of the potential. We investigate pattern formation in two-dimensional systems, for various interaction potential profiles, for example, we distinguish "soft-core" and "hard-core" interactions and analyze the transitions between different types of patterns. Based on this analysis, we construct a morphology diagram, which represents different morphologies, for various interaction parameters and particle densities [170]. We propose a new approach to characterize the different "morphologies": instead of qualitative characterization of the patterns (e.g., clusters or labyrinths), we introduce a number of quantitative criteria to distinguish these. In particular, the obtained patterns are analyzed in terms of the Radial Distribution Function (RDF) and additional quantities characterizing, e.g., the local density of particles in clusters.

* This chapter is based on the following publications:
[1] H. J. Zhao, V. R. Misko, and F. M. Peeters, Physica C: Superconductivity (2012), doi:10.1016/j.physc.2011.12.033.
[2] H. J. Zhao, V. R. Misko, and F. M. Peeters, arXiv:1107.0699 (New journal of Physics (accepted)) (2012).

6.1 Model

In type-II superconductor which, as shown in Eq. (1.29), the vortex-vortex interaction can be presented with a combination of two Bessel function. The Eq. (1.30) used in Ref. [24, 25] have a long-range Coulomp-type repulsive interaction and a short-range Yukawa attractive, which was also used in Ref. [21–23] to study the pattern formations in 2D electron systems. Thus, Eq. (1.30), is more close to the real vorter-vortex interaction in superconducting films, where the vortex-vortex interaction is logarithmic. In bulk superconductors, we model the vortex-vortex interaction potential using a generalized form of Eq. (1.29) :

$$V_{ij} = V_0 \left(\frac{a}{b} K_0(br_{ij}/\lambda) - K_0(r_{ij}/\lambda) \right). \tag{6.1}$$

Here, K_0 is the zeroth-order modified Bessel function, $r_{ij} =\mid \mathbf{r}_i - \mathbf{r}_j \mid$ is the vortex-vortex distance, V_0 and λ are the units of energy and length, respectively. These units can be specified, depending on the system. For example, in case of a type-II superconductor appropriate units of length λ and the energy V_0, correspondingly, are the magnetic field penetration depth λ and $V_0 = \Phi_0^2/8\pi^2\lambda^2$, where $\Phi_0 = hc/2e$ (see, e.g., Ref. [171]).

In the dimensionless form, the interaction potential (6.1) reads as

$$V'_{ij} = \frac{V_{ij}}{V_0} = \frac{a}{b} K_0(br'_{ij}) - K_0(r'_{ij}), \tag{6.2}$$

where the dimensionless length is defined as $r'_{ij} = r_{ij}/\lambda$. Further on, we will omit the primes and use the dimensionless form of the potential (6.2). The interaction force is then given by

$$\mathbf{F}_{ij} = -\nabla V_{ij} = (aK_1(br_{ij}) - K_1(r_{ij}))\hat{\mathbf{r}}_{ij}, \tag{6.3}$$

where K_1 is the first-order modified Bessel function, $\hat{\mathbf{r}}_{ij} = (\mathbf{r}_i - \mathbf{r}_j)/r_{ij}$, and a and b are two positive coefficients.

The first term of Eq. (6.3) is repulsive while the second term describes an attractive interaction force. Indeed, for $r \to \infty$, $K_1(x) \to \sqrt{\pi/(2x)}e^{-x}$. The interaction force (6.3) has a repulsive (attractive) tail when $b < 1$ ($b > 1$), while for $r \to 0$, $K_1(x) \to 1/x$ and thus $F_{ij} \to (a/b - 1)/r$. Therefore, for short range the interaction force (6.3) is repulsive (attractive) when $a > b$ ($a < b$), and we only consider the case $a > b$ since an attractive interaction for short distances would result in a collapse of our system of point particles. When $a > b$ and $b < 1$, the interaction is always repulsive, and particles form a Wigner crystal structure. The most interesting case is realized when $a > b$ and $b > 1$, and the interaction has a *repulsive core* and *attractive tail* [172]. In this case, there exists a critical distance r_c, where the inter-particle interaction energy (6.1) reaches a minimum (and the interaction force (6.3)

changes sign). By setting the force equal to zero, the coefficient a is given by

$$a = \frac{K_1(r_c)}{K_1(br_c)}. \tag{6.4}$$

The pattern formation is determined by the coefficients b, r_c, and the particle density n. We study pattern formation in a system of interacting point-particles by numerically integrate the Langevin equations using MD simulation [21–23, 171] (see the previous chapters). Here, the overdamped equation of motion is given by:

$$\eta \mathbf{v}_i = \mathbf{F}_i = \sum_{j \neq i} \mathbf{F}_{ij} + \mathbf{F}_i^p + \mathbf{F}_i^T. \tag{6.5}$$

$\mathbf{F}_i^p$ given by

$$\mathbf{F}_i^p = \sum_k^{N_p} \left(\frac{f_p}{r_p} \right) \left| \mathbf{r}_i - \mathbf{r}_k^{(p)} \right| \Theta \left(\frac{r_p - \left| \mathbf{r}_i - \mathbf{r}_k^{(p)} \right|}{\lambda} \right) \hat{\mathbf{r}}_{ik}^{(p)}, \tag{6.6}$$

is the pinning force (although often neglected, in general case we introduced random pinning sites, see Sec. 6.2.2). Here N_p is the number of pinning sites, f_p is the maximum pinning force of each potential well, r_p is the range of the pinning potential, Θ is the Heaviside step function, and $\hat{\mathbf{r}}_{ik}^{(p)} = (\mathbf{r}_i - \mathbf{r}_k^{(p)}) / \left| \mathbf{r}_i - \mathbf{r}_k^{(p)} \right|$.

We consider a two-dimensional (2D) square simulation region $L_x \times L_y$ in the xy-plane and apply periodic boundary conditions in the x and y directions. For the interaction force given by Eq. (6.3), which exponentially decays for large distances, we use a cut-off for $r > 8$. Note that in such a way the interaction in our system is finite-range. The length of the square cell $L_x = L_y = L$ has been varied from 60 to 180 to examine the finite-size effects, and we set $L = 120$ to optimize the calculations, without appreciable influence on the results. To obtain stable particle patterns, we performed simulated annealing simulations (SAS) of interacting particles. For this purpose, particles were initially randomly distributed inside the simulation region at some suitable non-zero temperature. Then temperature was gradually reduced to zero, and the simulation was continued until the total force acting on any single particle became much smaller than typical forces in the system.

6.2 Pattern formation

In this section, we study pattern formation and identify different morphologies depending on parameters of the interaction r_c, b and the particle density n. In Fig. 6.1, we illustrate the change of the interaction force profile due to the

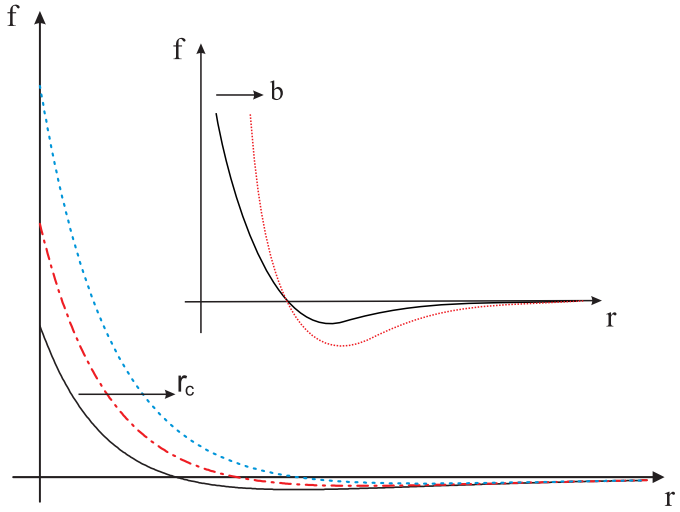

Fig. 6.1 The profile of the model inter-particle interaction force, given by Eq. (6.3), versus the distance. The main panel and the inset panel show the change in the force profile due to an increase of r_c and b, respectively.

increase of r_c and b. The interaction force is very sensitive to r_c, since its increase directly leads to an increase in the repulsive part in Eq. (6.3) (see the main panel of Fig. 6.1). On the other hand, increase of b leads to the increase of both the repulsive and attractive parts (see the inset of Fig. 6.1). However, the repulsive interaction increases much faster for $r < r_c$ than the attractive interaction for $r > r_c$.

Thus, increasing b facilitates stabilization of the minimum inter-particle distance at r_c. In other words, increase of b results in hardening of the core in the interaction force (6.3), i.e., the interaction changes continuously from a "soft-core" to a "hard-core" regime.

6.2.1 Soft-core interaction

In this subsection, we analyze pattern formation in the absence of additional pinning. The influence of random pinning on the pattern formation will be discussed in the next subsection.

To study pattern formation in the soft-core regime, we set the coefficient $b = 1.1$. We define the critical density as $n_c = 8r_c^{-2}/\sqrt{3}$ which is the density of an ideal (hexagonal) Wigner crystal with the lattice constant $a = r_c$. The density is defined as $n = N/S$, where $S = 120 \times 120$ is the area of the simulation region and N is the number of particles (further on, in our analysis of various patterns, we will refer either to the number of particles N in the simulation cell or to the density which is $n = N/14400$). For the case of

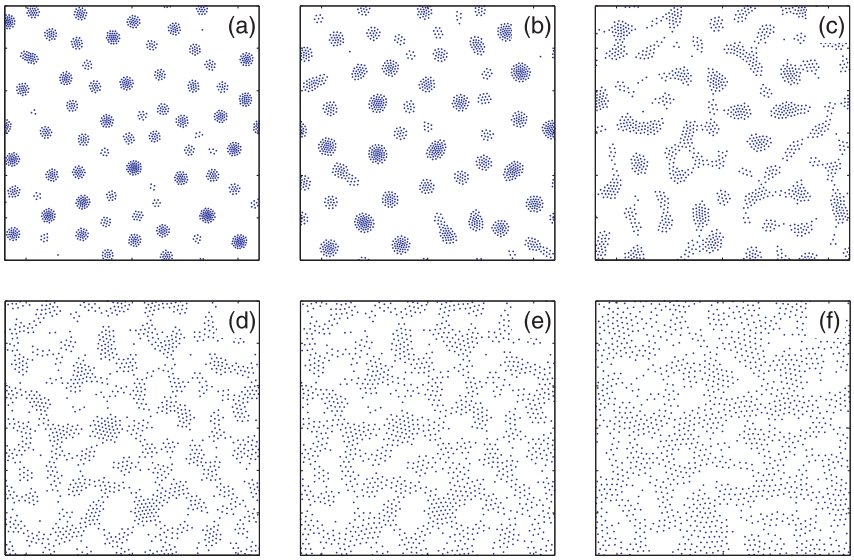

Fig. 6.2 Patterns for $N = 1500$ particles in a unit cell $L \times L$ with $L = 120$ for varying r_c: $r_c = 1.9$ (a), 2.1 (b), 2.3 (c), 2.5 (d), 2.7 (e), 2.9 (f).

$n < n_c$, which is considered here, the Wigner crystal is not stable due to the attractive interaction. In Fig. 6.2, we present patterns formed by $N = 1500$ particles when r_c increases from 1.9 (a) to 2.9 (f). Note that the condition $n < n_c$ is always fulfilled for all the values of r_c in this range. We found that for $r_c < 2.1$ particles form clusters similar to the formation of the "clump" morphology found in colloids and two-dimensional (2D) electrons [21–23, 115] (see Figs. 6.2(a) and (b)). The main difference to the patterns found in Refs. [21–23] is that the relatively softer core in our case is compressed due to the attractive interaction, and the clusters acquire a circular shape. In addition, the interaction between the clusters (decaying exponentially for long distances within the interaction range) becomes negligible for inter-cluster distance of the order of few to several r_0. Therefore, the clusters can be considered as non-interacting for low densities (although they still do not approach each other), contrary to the situation described in Ref. [21, 23] when a super-lattice is formed due to the long-range cluster-cluster repulsion. When r_c increases, the clusters expand. In particular, for $r_c > 2.1$, the clusters start to elongate which is an indication of the instability with respect to the transition to the stripe morphology. For $2.1 < r_c < 2.3$, a mixed state with both stripes and clusters is observed (see Fig. 6.2(c)). Further increase of r_c gradually destroys the clusters and leads to the formation of labyrinths (see Figs. 6.2(d) to (f)).

In order to reveal the influence of the density on the pattern formation, we gradually increase the number of particles from 1500 to 10500 in our sim-

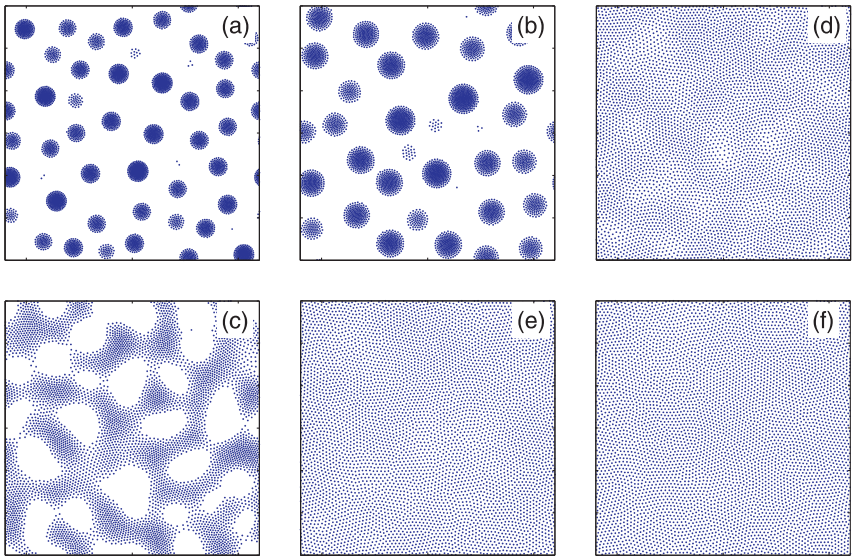

Fig. 6.3 Patterns for $N = 5500$ particles in a unit cell $L \times L$ with $L = 120$ for varying r_c: $r_c = 1.9$ (a), 2.1 (b), 2.3 (c), 2.5 (d), 2.7 (e), 2.9 (f).

ulation cell. First, in Fig. 6.3, we present patterns formed by $N = 5500$ particles for varying r_c. Note that $n > n_c$ for $N = 5500$. As compared to the lower density case shown in Fig. 6.2, in case of clusters, the additional particles lead to the expansion of the clusters (see Figs. 6.3(a) and (b)). A mixture of clusters and stripes is formed when the additional particles form bridges connecting the clusters (see Fig. 6.3(c)) which will be discussed in detail below. For labyrinths (shown in Figs. 6.2(d) to (f) for $N = 1500$), the additional particles fill the empty regions (voids), resulting in the formation of the hexagonal lattice with varying local density (Fig. 6.3(d)) and, finally, a regular hexagonal lattice (see Figs. 6.3(e) and (f)). Note that the lattice with varying local density (Fig. 6.3(d)) is not stable in systems with pure repulsive interaction such as vortices in type-II superconductors.

We analyzed in detail the intermediate regime (i.e., corresponding to the transition from clusters to stripes, see Fig. 6.2(c)) where $r_c \approx 2.3$. The resultig patterns for varying density are shown in Fig. 6.4. Fig. 6.4(a) displays a configuration at low density with $N = 1500$ when many individual clusters are formed. With increasing the density (see Fig. 6.4(b)), the clusters connect with each other and form stripes. A further increase of the number of particles (Fig. 6.4(c)) results in the formation of a complex mixture of interconnected stripes with voids. A very interesting and counter-intuitive evolution is observed when the number of particles increases from $N = 5500$ to $N = 6500$ (see Fig. 6.4(d)): in contrast to the gradual transition from a void-rich config-

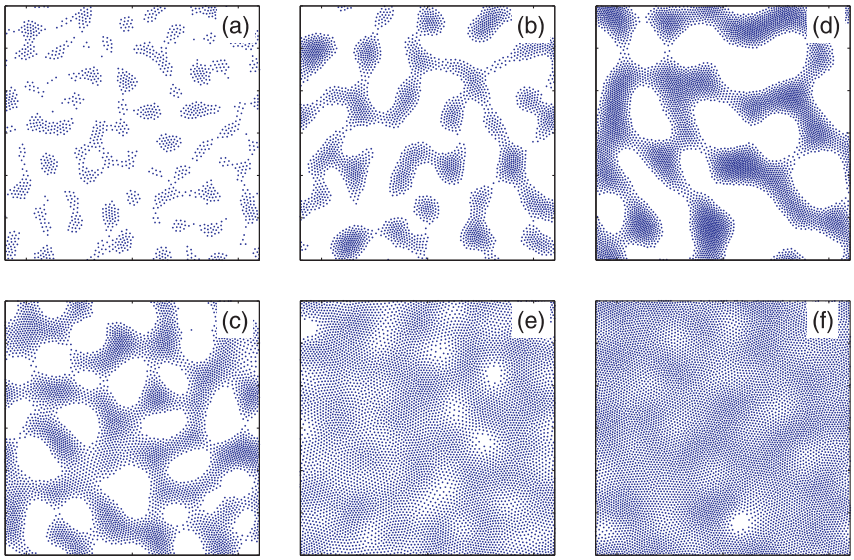

Fig. 6.4 Patterns for $r_c = 2.3$ and varying number of particles N (in the computational unit cell $L \times L$ with $L = 120$): $N = 1500$ (a), 3500 (b), 5500 (c), 6500 (d), 7500 (e), 9500 (f).

uration to a lattice-rich configuration when N changes from $N = 3500$(b) to $N = 5500$(c), in case of $N = 6500$ we observe a "reentrant" behavior, i.e., the void-rich configuration starts to recover which is compensated by an increase of the local density in the stripes. However, further increasing density results in the expansion of the stripes to the empty regions which is accompanied by a decrease of the local density in the stripes, as shown in Fig. 6.4(e). The distribution of particles becomes more uniform, with only few small voids. Finally, for $N = 9500$ (Fig. 6.4(f)), we obtain a deformed hexagonal lattice characterized by a varying local density with only one small void.

Our calculations show that the obtained patterns are very sensitive to variations in r_c. Thus, if r_c slightly decreases (e.g., $r_c = 2.25$), the number of clusters greatly increases as compared to the case $r_c = 2.3$, for the same density of particles. For $r_c = 2.25$, we also observe the transition from a void-rich configuration to a lattice-rich configuration. However, since the decrease of r_c increases the attractive component of the inter-particle interaction this occurs at much higher density. For even smaller values of r_c, i.e., $r_c < 2.1$, we do not observe lattice pattern, even for extremely large number of particles (up to $N = 20000$).

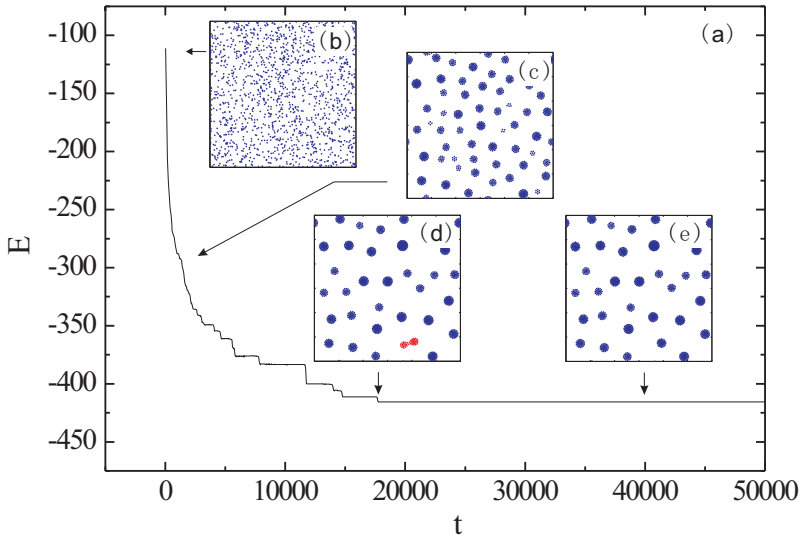

Fig. 6.5 The evolution of the energy E versus time t (a); snapshots corresponding to various annealing times (b)∼(e). Two merging clusters are shown in red(gray) in (d).

6.2.2 Analysis of stability of the patterns

To further study the stability of the patterns, here we analyze the influence of the cut-off procedure and the annealing time used in our simulations. Alternatively, we consider the effect of additional weak pinning and modify the inter-particle interaction by introducing a weak repulsive tail.

First, we consider the case when clusters are formed (i.e, $r_c < 2.3$). We choose $r_c = 1.9$ and increase the cut-off distance from 8 to 16λ. We also increase the annealing time from typically $(10000 - 20000)\Delta t$ to $200000\Delta t$, where $\Delta t = 0.04$ is the time step of the MD simulation. In Fig. 6.5, we plot the evolution of the energy with time, and we show some representative snapshots in the insets. We start from a random configuration of particles (see Fig. 6.5(b)). During the annealing, the energy first drops rapidly due to the clusterization of the particles. After relatively short time, small clusters start to merge and form larger clusters (see Fig. 6.5(c)). The average inter-cluster distance increases when the total number of clusters decreases. The merging becomes more difficult and considerably slows down when the clusters are well separated. As a result, short-living metastable states are formed (see Fig. 6.5(d)). However, during the merging of the clusters, the life-time

of the metastable states increases very rapidly, and gradually the short-living metastable states evolve into *long-living metastable states* when the clusters are well separated (see Fig. 6.5(e)). Comparing with the relatively faster annealing case (i.e., $20000\Delta t$), we see that the slower annealing process results in a decrease of the number of clusters inside the simulation cell, which increases the life-time of the metastable states. However, even for the shorter annealing times (i.e., $20000\Delta t$), we arrive at long-living metastable configurations which can have either slightly higher energy or even the same energy as those states obtained during the long-time annealing (note that the energy of the configuration does not change over the time interval from $\approx 15000\Delta t$ to $50000\Delta t$). It is worth noting that the morphology is similar to that found in the "fast" annealing process.

Thermodynamically stable states can be obtained in the presence of weak random pinning. To verify this, we introduce weak random pinning sites in the system, with the maximum pinning force $f_p = 0.2$ and radius $r_p = 0.3$, and the density of random pinning sites being the same as the density of the particles. We found that such weak pinning produces no appreciable impact on stripes, labyrinths or lattices. In case of clusters, the bonding energy due to the inter-particle interaction within every individual cluster is strong, and the weak pinning is not sufficient to destroy the structure of the clusters. However, the inter-clusters interaction is weak, therefore, those clusters can be easily stabilized by weak pinning. Thus, comparing to the patterns obtained without pinning, we find that slightly smaller clusters are formed in the presence of pinning, and the merge of clusters is prevented even for two relatively close but small neighbor clusters (see Fig. 6.6). Note that in the absence of pinning, clusters have nearly circular shape while their shape is less regular in case of weak pinning. In the latter case, some of the particles were pinned individually, i.e., outside the clusters, see Fig. 6.6(b).

An alternative way to stabilize clusters (and approach the thermodynamically stable configurations) consists in using a modified force with an additional weak *repulsive tail*, e.g., taken in the form: $\mathbf{F}'_{ij} = \mathbf{F}_{ij}\cosh(r_e - r)$, where r_e is a parameter chosen as $r_e = 10$, and the cut-off of the interaction is set at 16λ. Then the resulting modified force coincides with the one given by Eq. (6.3) for $r < 8$ but the weak attractive tail smoothly evolves to repulsive when $r > 10$. The modified interaction force leads to very similar patterns as the original one (given by Eq. (6.3)) because the weak repulsive tail is not efficient for the clusters to form super-structures (see, e.g., Ref. [21, 23, 24]), but is sufficient for stabilizing the configurations of particles. When we increase the inter-cluster *repulsive* interaction by increasing the particles density, the resulting patterns are similar to the previously calculated long-living metastable states. The reason for this behavior is that the radius of a cluster is insensitive to the particle numbers within the cluster. As a result, the inter-cluster repulsive increases very slowly as the density increases.

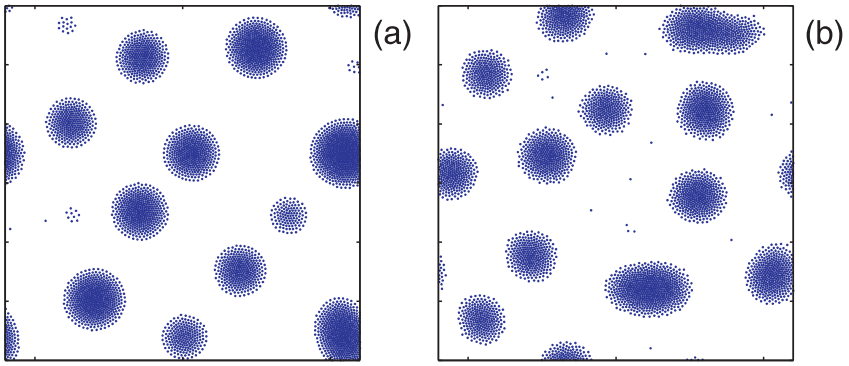

Fig. 6.6 Calculated patterns for $r_c = 2.1$, $N = 4500$ and the annealing time $50000\Delta t$: without pinning (a) and in presence of weak random pinning with the maximum pinning force $f_p = 0.2$ and radius $r_p = 0.3$ (b).

6.2.3 Morphology diagram

Based on the above analysis of the patterns, we constructed a morphology diagram (as we explained above, the calculated patterns are long-living metastable states, i.e., in the absence of additional pinning or the long-range repulsive tail, – rather than real thermodynamic phases; thus the diagram presents various morphologies) in the plane of r_c and the number density n (see Fig. 6.7). For extremely low density ($n < 0.03$), particles form small clusters which are well separated, and the patterns are rather insensitive to variations in r_c. However, morphologies become richer when density n increases (i.e., $n > 0.1$). Low values of r_c (i.e., $r_c < 2.1$) still favor cluster formation for a broad range of densities, although the particle density in clusters increases for large n. With increasing r_c, clusters become unstable with respect to the formation of the "bridges" between separate clusters, which is a precursor of the formation of stripes. Stripes are formed in a rather narrow range of r_c when $r_c > 2.1$ (see Fig. 6.7). The stripe patterns can be divided into two sub-groups, I and II, i.e., void-rich (see Fig. 6.7(i)) and void-poor (lattice-rich) stripes (Fig. 6.7(j)). For larger r_c and $n < n_c$, particles form labyrinth structures. However, when increasing the density, additional particles fill the empty regions and finally they form a deformed hexagonal lattice with varying density. Depending on r_c and $n < n_c$, deformed lattice is characterized by a varying local density or by the appearance of voids. Correspondingly, we distinguish two regions (1 and 2 in Fig. 6.7). Note that in the vicinity of the morphology boundaries, patterns are always mixtures of the two morphologies (e.g., clusters and stripes) except the transition from the stripes to the deformed hexagonal lattice. Near this morphology boundary, particles form either stripes with high local density or deformed hexagonal

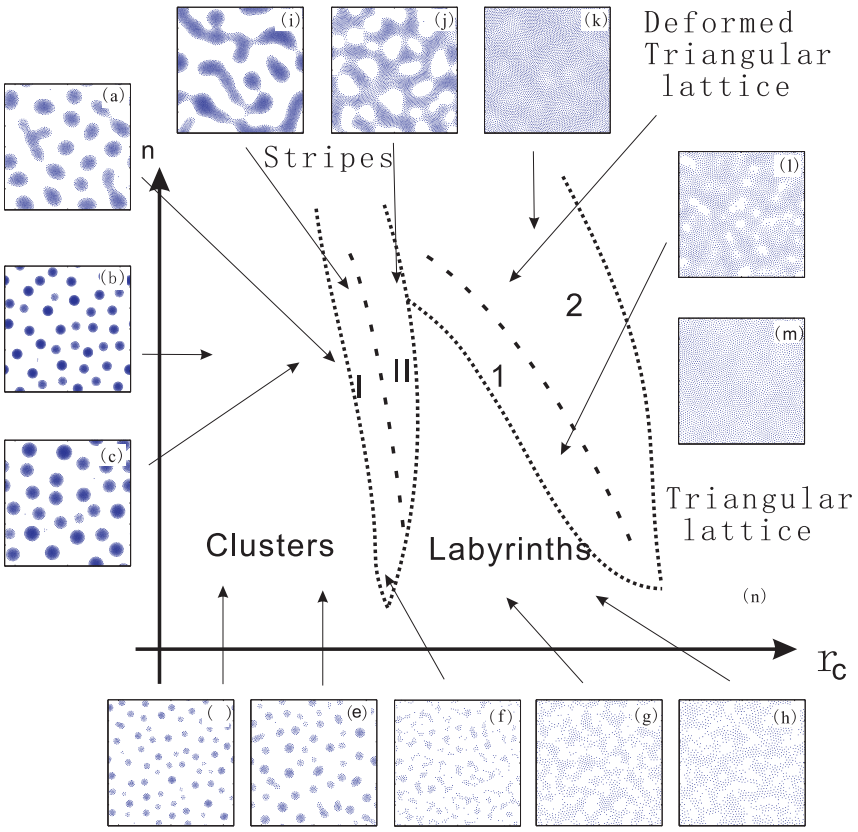

Fig. 6.7 The morphology diagram in the plane "critical radius r_c − density n" (n) and representative patterns (a to m) for the different types of patterns. For extremely low density ($n < 0.03$), particles form small, well separated, clusters. For $r_c < 2.1$, particles form clusters. For larger r_c, the size of the clusters increases (see the change from (d) to (e) and (b) to (c)). The increase of the density results in increasing the size of the clusters (see the change from (d) to (b) and (e) to (c)). Further increase of r_c leads to the elongation of the clusters and the formation of "bridges" between them (a). Thus, the configurations change gradually from clusters to stripes (i). When r_c or n become even larger, stripes interconnect and form patterns with voids (j). Thus the stripes are divided into two sub-groups, I and II. When r_c becomes even larger, labyrinth-like configurations are formed for $n < n_c$ (see (g) and (f)). With further increase of r_c or n, deformed hexagonal lattice with (k) or without voids (l) are formed. The deformation of a hexagonal lattice is reduced for even larger values of r_c and n (m).

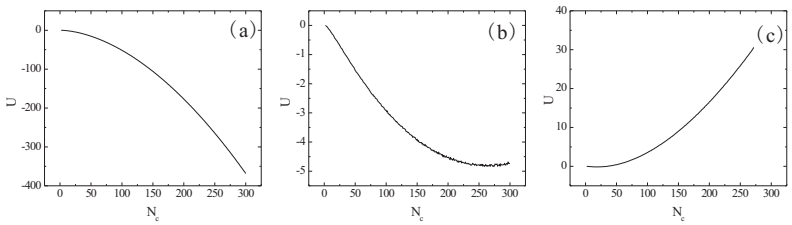

Fig. 6.8 The potential energy per particle U versus the total number of particles within the cluster, N_c, for $r_c = 1.8$ (a), 2.3(b), 2.5(c).

lattices with lower local density. The probability of finding the lattice configuration greatly increases when r_c or n increases. Finally, for very high density, when the average interparticle distance becomes smaller than r_c the repulsive interaction prevails resulting in the formation of an almost perfect hexagonal lattice.

The stability of clusters for varying parameter of the inter-particle interaction, r_c, can be examined by applying additional weak *confinement potential* and calculating the energy corresponding to varying number of particles in the system. For this purpose, we use a parabolic potential, similar to F_p^i in Eq. (6.6), to confine all the particles and gradually decrease f_p to zero during the annealing. This allows us to obtain one large cluster for various r_c. Then we study the stability of these induced clusters, by analyzing the average energy per particle U for various r_c and N_c, where N_c is the total number of particles composing the cluster. We found that for $r_c < 2.3$, the clusters are stable: U is approximately proportional to N_c^2 and it decreases while N_c increases (see Fig. 6.8 (a)). The size of the cluster grows with the number of constituent particles: it goes to infinity for $N_c \to \infty$, which corresponds to *phase separation*. Note that this result could be understood from a comparison of the model potential (Eq. (6.2)) with the Lennard-Jones potential: for small r_c, both the potentials become very similar, in particular, for $r_c \approx 1$. On the other hand, it is well-known that the Lennard-Jones potential leads to phase separation.

For $r_c = 2.3$, which is a typical value for stripe formation, there is a saddle point in the function U versus N_c, which shows that the clusters have an *optimal* size, e.g., $N_c \approx 280$ (see Fig. 6.8 (b)). Finally, for $r_c > 2.3$, U changes the sign when $N_c > 7$, resulting in a positive energy indicating that the clusters in this case are overheated by the parabolic potential and therefore are not stable. Labyrinths are more favorable in this case.

The patterns presented in Fig. 6.7 are found in many real systems. For example, clusters are found in such systems as colloids [118, 120, 130, 131] and

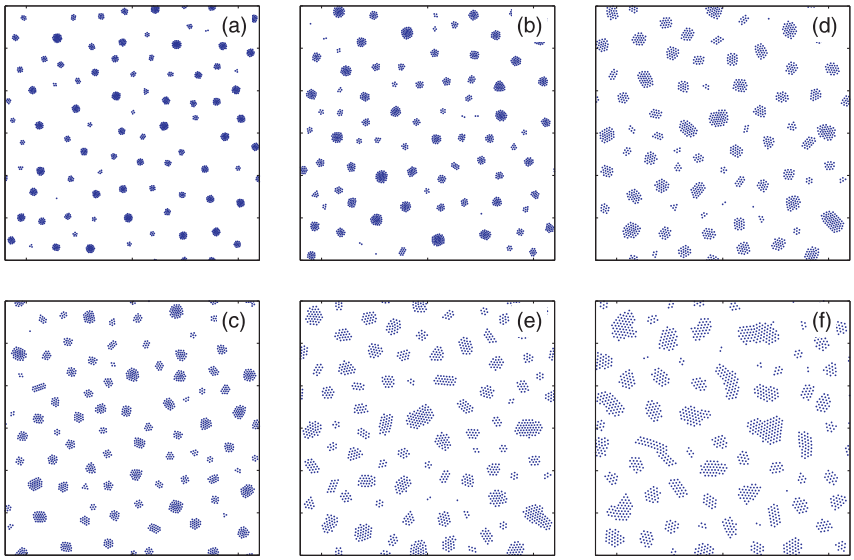

Fig. 6.9 Patterns for $N = 1500$ particles in a unit cell $L \times L$ with $L = 120$, $b = 4$ and for varying r_c: $r_c = 1.15$ (a), 1.3 (b), 1.45 (c), 1.6 (d), 1.75 (e), 1.9 (f).

2D electrons [21–23]. The obtained stripe patters are very similar to those in Langmuir monolayers [117].

Furthermore, several of the calculated morphologies were found in superconductors, e.g., the stripe morphology in the mixed state of type-I superconductors, clusters of Meissner phase or vortex clusters in the intermediate state in low-κ type-II superconductors [18, 19], the labyrinth phase (i.e., vortex lattice with voids) or vortex clusters in type-1.5 superconductors [26]. In spite of the variety of the physical systems and length scales ranging from nano- and micro-objects to cosmic objects, the common feature of all these systems is a competing attractive-repulsive inter-particle interaction which allows analyzing them within the same approach.

6.2.4 Hard-core interaction

Let us now analyze the influence of the b parameter on the pattern formation. As mentioned above (see Fig. 6.1), an increase in parameter b changes the potential from a soft-core to a hard-core. Hardening the repulsive core in the interaction potential generally leads to a decreasing compressibility of the inner parts of the patterns where particles are closely packed. Clearly, that in this case the patterns change as compared to the soft-core regime.

As shown in Fig. 6.9, for $b = 4$ and low density ($N = 1500$ per simulation region), all the patterns are clusters of different shape. Thus for $r_c = 1.15$ and

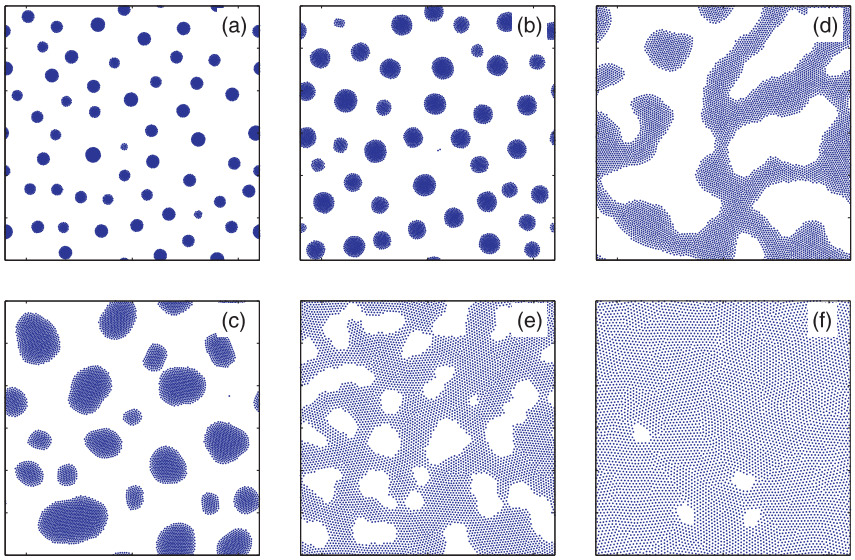

Fig. 6.10 Patterns for $N = 6500$ particles in a unit cell $L \times L$ with $L = 120$, $b = 4$ and for varying r_c: $r_c = 1.15$ (a), 1.3 (b), 1.45 (c), 1.6 (d), 1.75 (e), 1.9 (f).

$r_c = 1.3$, the clusters are of circular shape similar to those found in the soft-core regime, although for $r_c = 1.3$ some clusters, composed of a small number of particles, have polygon shapes. With increasing r_c, polygon-shaped clusters become more favorable, which allows us to identify them as "short stripes". For even larger r_c, the clusters become much larger. They represent separate islands of hexagonal lattice.

For higher density ($N = 6500$), the variety of patterns is much richer. Although for $r_c = 1.15$ circular-shape clusters are still observed (see Fig. 6.10(a)), which grow in size for $r_c = 1.3$ and slightly deviate in shape from circular (Fig. 6.10(b)), for larger $r_c = 1.45$, the deviations of the cluster shape from circular become more pronounced (see Fig. 6.10(c)). With further increasing r_c, i.e., $r_c = 1.6$, stripes start to form (see Fig. 6.10(d)) followed by lattices with voids for $r_c = 1.75$ and $r_c = 1.9$. In the hard core regime, deformations of lattices occur via the appearance of voids instead of varying local density (as it happens in the soft-core regime).

The obtained patterns presented in Figs. 6.9 and 6.10 resemble the nanoscale domain patterns formed by Cu and Pb atoms on a surface of Cu [173, 174]. In particular, the lattice islands (Fig. 6.9(d to f)), the stripes (Fig. 6.10(d)) and void-rich configurations (Fig. 6.10(e)) are similar to the patterns evolving from islands to stripes and "inverted" islands formed by Cu and Pb atoms arranged in a single atomic layer on a Cu(111) surface [173, 174], with increasing the atomic coverage.

6.3 Analysis of the patterns

6.3.1 Radial distribution function

Although different patterns and morphologies studied above are qualitatively well distinguished, it is highly desirable to build a set of solid criteria which would allow us to identify them in a quantitative manner. For this purpose, we analyze here different morphologies by means of the Radial Distribution Function (RDF). The RDF, $g(r)$, describes the variation of the atomic (particle) density as a function of the distance from one particular atom (particle). If we define an average density as $n = N/V$ (where V is the volume or surface area in the 2D case), then the local density at distance r is $ng(r)$. The knowledge of RDF is important since one can measure $g(r)$ experimentally using digital video microscopy [175]. Moreover, macroscopic thermodynamic quantities can be calculated using $g(r)$ in thermodynamics [176].

In our calculations, we define the RDF $g_i(r)$ as follows:

$$g_i(r) = \frac{\triangle N/\triangle r}{2\pi r}. \tag{6.7}$$

Here, the lower index indicates that the RDF centers at the position of the i^{th} particle; $\triangle N$ is the number of particles whose distance to the i^{th} particles is between r and $r + \triangle r$. The average $g(r)$ is given by

$$g(r) = \frac{1}{N}\sum_{i=1}^{N} g_i(r). \tag{6.8}$$

In Fig. 6.11(a), we plot the function $g(r)$ calculated for the low-density cluster configuration shown in Fig. 6.2(b). The function $g(r)$ has two well-pronounced peaks. The first peak corresponds to the average distance to the first coordination sphere (nearest neighbors) while the second one is located at the distance approximately twice the distance to the first peak, which shows short-range periodicity. For r larger than the size of the cluster, and smaller than the inter-cluster distance, $g(r) < 1$, since only few particles are located inside this range. The decreasing tail in the RDF shows a strong aggregation of the particles forming clusters. The minimum of $g(r)$ is very close to zero indicating that most of the clusters have circular symmetry and they are well separated. The position of the minimum of $g(r)$ (marked by the gray arrow in Fig. 6.11(a)) gives an estimate of the average diameter of the clusters.

For stripes (see Fig. 6.11(b) for the pattern shown in Fig. 6.2(d)), there are also two peaks indicating the short-range periodicity, similar to the cluster morphology. However, unlike in the case of clusters, the minimum of $g(r)$ is non-zero since the stripes are generally continuous. For labyrinths (see Fig. 6.11(c) for the pattern shown in Fig. 6.2(f)), only short-range periodic ordering exists, and $g(r)$ becomes uniform for larger r.

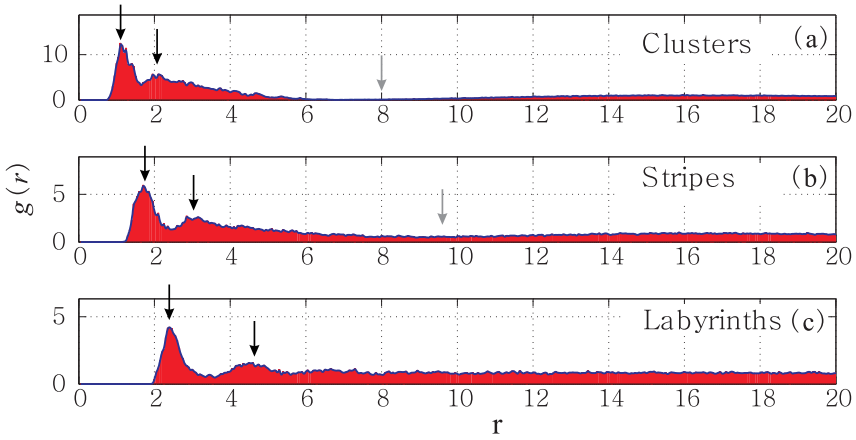

Fig. 6.11 The average RDF of the patterns formed at low density ($N = 1500$). (a), (b), and (c) correspond to the patterns shown in Figs. 6.2(b), (d), and (f), respectively. The peaks marked by dark arrows show the shot-range periodicity. The gray arrow shows the minimum of the RDF.

In Fig. 6.12, we plot $g(r)$ for the patterns formed at high density ($N = 5500$). For clusters, the increase in the density leads to an increasing variation of the cluster size. Note, however, that the sizes of individual clusters are rather insensitive to moderate variations of the number of particles in the clusters, due to the strong compressibility of the core. As a result, the function $g(r)$ for the high density clusters misses the short-range periodicity and the second peak disappears (see Fig. 6.12(a)). Strikingly, this peak still exist for the void-rich morphology (see Fig. 6.12(b)). The decrease of the tail of $g(r)$ becomes very slow, which shows a minor aggregation of the particles.

For lattices (see Fig. 6.12(b)), the position of the first peak is $r_1 \approx a = \sqrt{2/(\sqrt{3}n)}$, where a is the distance between two neighboring particles in the ideal hexagonal lattice with the density n. The positions of the second and third peaks are at $r_2 \approx \sqrt{3}a$ and at $r_2 \approx 2a$, respectively, corresponding to those in a hexagonal lattice. A fourth, fifth and even sixth peaks appear, which show that this structure is much more ordered. However, due to the variation of the local density, these peaks are inhomogeneously broadened: they are actually a combination of many neighboring peaks. These peaks become more pronounced for larger r_c or n, which implies that the lattices become more regular.

It is interesting to compare the results for the function $g(r)$ for hard-core interaction with those for soft-core interaction. Although the clusters shown in Figs. 6.10(a) and (b) have shapes very similar to those of the clusters shown in Figs. 6.3(a) and (b), the analysis using the RDF shows that most of the clusters shown in Fig. 6.10(b) have hexagonal ordered cores. The peaks in $g(r)$

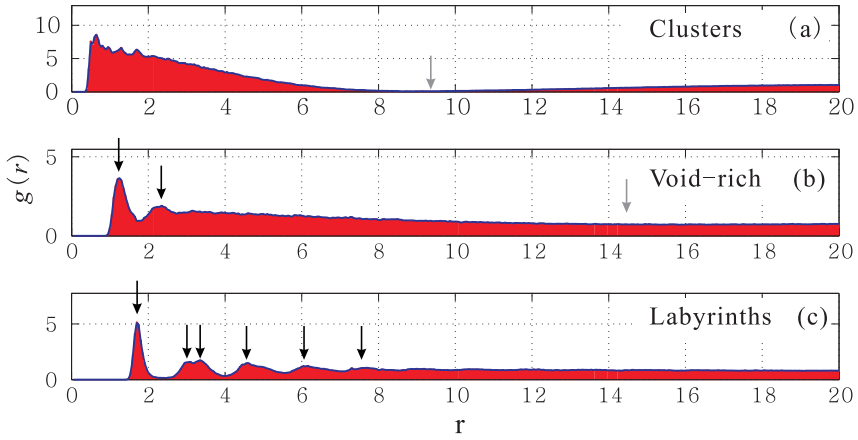

Fig. 6.12 The average RDF of the patterns formed at high density (N=5500). (a), (b), and (c) correspond to the patterns shown in Figs. 6.3(b), (d), and (f), respectively. The arrows have the same meaning as in Fig. 6.11.

appear to be much better separated than, e.g., for the deformed hexagonal lattice formed in the soft-core case (see Fig. 6.12(c)). For the stripe and void-rich patterns, the RDF shows much clearer hexagonal lattice ordering.

Therefore, the analysis using the RDF allowed us to establish quantitative criteria for the different patterns and reveal the differences in the structure of the patterns (which look similar, e.g., clusters) in case of soft- and hard-core interparticle interaction.

6.3.2 Local density

Using the RDF, let us define another useful quantity, the "order parameter", to characterize various types of patterns. By definition, the local density is:

$$I_i = \int_0^{\xi} 2\pi r n g_i(r) dr = N_\xi - 1. \tag{6.9}$$

Here, $N_\xi \approx \pi\xi^2 n$ is the average number of particles within the circle centered at the i^{th} particle with radius $R = \xi$. Since in an ideal hexagonal lattice one particle has six nearest neighbors, then $N_\xi = 7$ and $\xi = \sqrt{N_\xi/\pi n} = \sqrt{7/\pi n}$. Thus, for any configuration characterized by a small local density fluctuation, the average local density $I = \langle I_i \rangle = 6$. From the definition given by Eq. (6.9), we can see that the presence of a large fraction of empty regions can result in a considerable increase of I since only a "shell" of those regions of thickness ξ is considered. In Fig. 6.14(a), we plot the function I for different r_c and N for the soft-core interaction with $b = 1.1$. We see that the function I can be used to charaterize the different types of patterns. Thus we found that, for

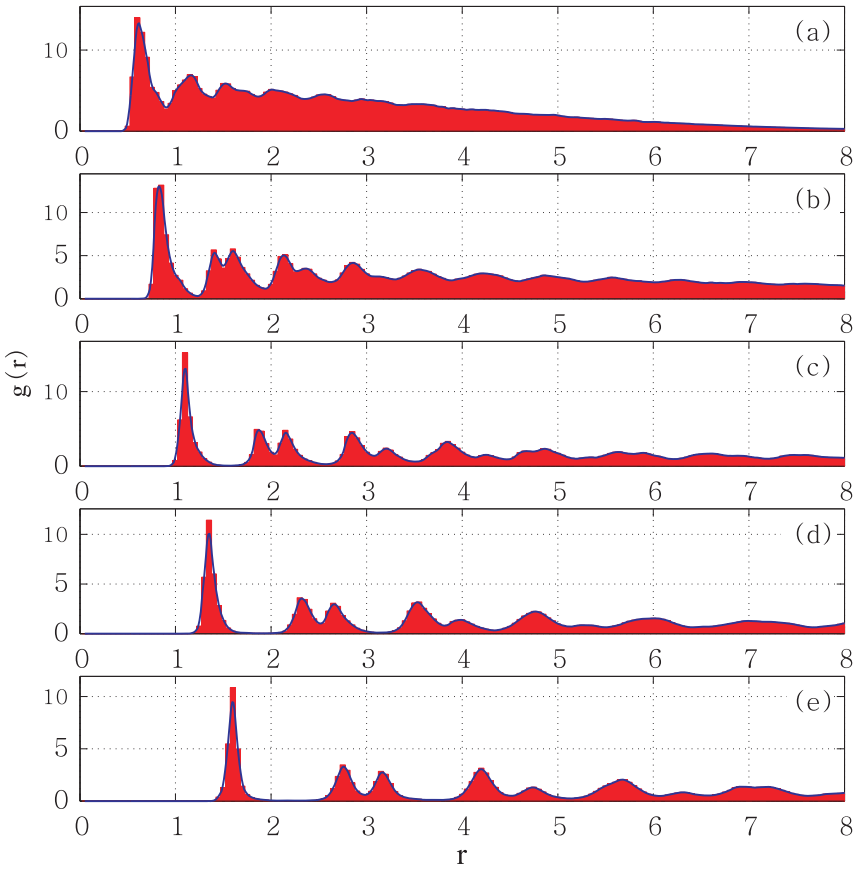

Fig. 6.13 The average RDF of the patterns formed in the hard-core case. (a), (b), (c), (d), and (e) correspond to the patterns (a), (b), (c), (d), and (e) in Fig. 6.10, respectively.

clusters, I is always large ($I > 20$) since aggregation is strong. For stripes, aggregation is weaker, and thus I is smaller ($10 < I < 17$). For labyrinths, the regions free of particles are relatively small. Therefore, I ranges between 6 to 9. Finally, for a hexagonal lattice, I is always 6. Therefore, the function I serves as a measure of the aggregation of particles and allows us to effectively distinguish the different types of patterns.

The function I also provides a tool to analyze the stability of patterns with increasing density. This is demonstrated in Fig. 6.14(b), where we plot I for the hard-core case when $b = 4$. For $r_c = 1.15$, $I > 20$ for all the values of the density, and thus the clusters are stable. However, the situation changes for $r_c = 1.3$: while clusters are formed for low densities up to $N \approx 7500$, for larger density I decreases below the value $I = 20$ which means that clusters elongate and interconnect giving rise to the onset of stripes formation. For $r_c = 1.45$, the particles start to form stripes at even lower density ($N = 3500$). For higher density, the additional particles fill in the empty regions and finally they form a regular lattice. For $r_c > 1.6$, the island-like clusters formed at low densities are very unstable with respect to an increase in density. The additional particles rapidly occupy the empty regions, and the patterns change form clusters to stripes and from stipes to lattice with increasing density.

Therefore, the phenomenological description of pattern evolution with increasing density we revealed above in Sec. 6.2.3 has been verified in a quantitative manner using the solid basis of the local density function approach.

6.3.3 Occupation factor

We demonstrated that the (average) RDF $g(r)$ (Eq. (6.8)) and the local density function I (Eq. (6.9)) allowed us to unambiguously characterize various types of patterns. At the same time, it is still hard to distinguish, using the above tools, between labyrinths (or a lattice with voids) and lattices, especially in the soft-core regime when the corresponding RDF does not differ much from each other, and both types of patterns are characterised by small values of I. However, these can be easily distinguished by employing another additional criterion, namely, the occupation factor which characterizes the fraction of the space occupied by particles to the total space.

Let us assume that all the patterns are formed by islands of hexagonal lattice with the average distance between two nearest neighbor particles $r = r_1$, where r_1 is the position of the first peak of the RDF. Then the ratio of the area occupied by the particles and the whole simulation area is $A = (r_1/a)^2$. As shown in Fig. 6.15(a), this ratio can be used to distinguish between labyrinths and lattices, since for lattices $A \approx 1$.

We also found that circular clusters in the case of soft-core interaction are stable with respect to an increase in the density. In this case, the additional particles cannot efficiently increase the occupation factor due to the increase in the local density of the core. However, for stripes and labyrinths, the occupation factor A increases with the density (see Fig. 6.15(a)). These

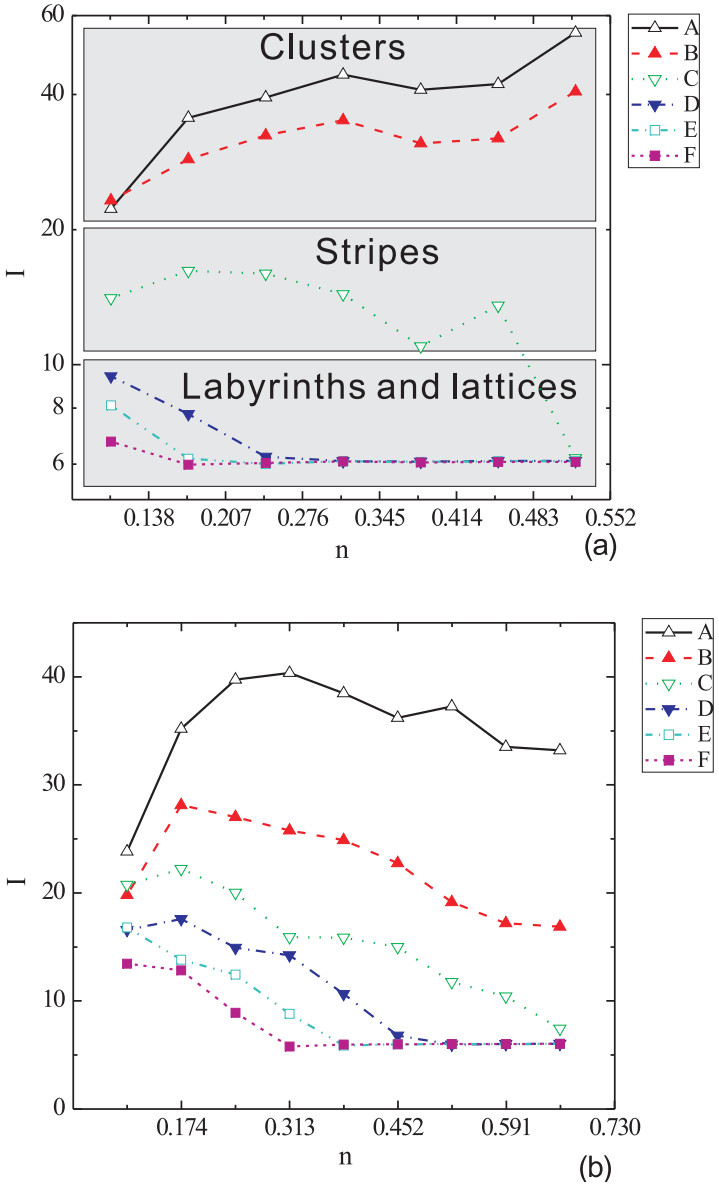

Fig. 6.14 The average local density I versus the particle density n for $b = 1.1$ (soft-core) (a). Curves A, B, C, D, E, and F correspond to $r_c = 1.9$, 2.1, 2.3, 2.5, 2.7, and 2.9, respectively. For clusters, $I > 20$, for stripes, $10 < I < 20$, for labyrinths, $6 < I < 10$; $I = 6$ for lattice and deformed lattice configurations. The local density I versus the particle density n for $b = 4$ (hard-core) (b). Curves A, B, C, D, E, and F correspond to $r_c = 1.15$, 1.3, 1.45, 1.6, 1.75, and 1.9, respectively.

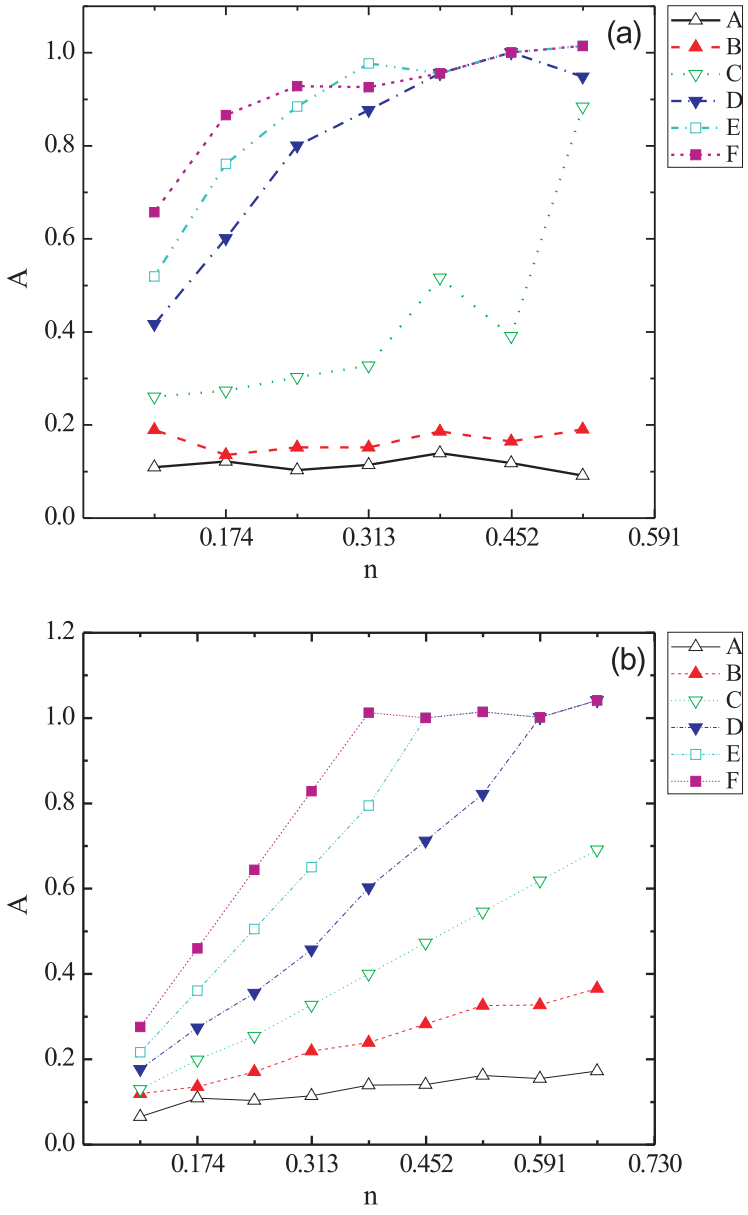

Fig. 6.15 The occupation factor $A = (r_1/a)^2$ for $b = 1.1$ (soft-core) (a). Curves A, B, C, D, E, and F correspond to $r_c = 1.9$, 2.1, 2.3, 2.5, 2.7, and 2.9, respectively. The occupation factor, A for $b = 4$ (hard-core) (b). Curves A, B, C, D, E, and F correspond to $r_c = 1.15$, 1.3, 1.45, 1.6, 1.75, and 1.9, respectively.

patterns are not stable for high density. Thus the large jump in $A(N)$ at $N = 6500$ in curve C in Fig. 6.15(a) shows the transition from stripes to the lattice.

As one can expect, in the case of hard-core interaction, the occupation factor increases nearly linearly versus the density (see Fig. 6.15(b)). Therefore, the polygon shape and island-like clusters are not stable: with increasing density, they evolve to the lattice configuration (the plateau in $A(N)$ in Fig. 6.15(b)).

In addition, let us introduce another useful quantity which characterizes the degree of "perfection" of a lattice. Let us define the particles with the inter-particle distance shorter than ξ as neighboring particles. Then

$$\varepsilon = \frac{1}{a}\sqrt{\frac{\int_0^\xi 2\pi r g(r) n (r-a)^2 dr}{\int_0^\xi 2\pi r g(r) n dr}} = \frac{1}{a}\sqrt{\frac{\int_0^\xi r g(r)(r-a)^2 dr}{\int_0^\xi r g(r) dr}}. \qquad (6.10)$$

is an average displacement of the inter-distance between two neighbor particles (measured in units of a), which is independent of the density. The function ε is non-zero for a deformed hexagonal lattice and zero for the ideal hexagonal lattice. Thus, ε quantitatively measures the degree of perfection of a lattice. Note that ε is only used for lattices as an auxiliary tool to distinguish ordered lattices from less ordered ones (see Table I).

Patterns	$g(r)$	I	A	ε
clusters	peak at $r_1(r_2)$, $g(r)_{min} = 0$	> 20		
stripes	peak at $r_1(r_2)$, $g(r)_{min} > 0$	$10 \sim 20$		
labyrinths	peak at $r_1(r_2)$, $g(r) \approx$ const, $r > r_2$	$6 \sim 10$	< 1	
lattice	several peaks: r_1, $r_2 \ldots$	≈ 6	≈ 1	0
deformed lattice	several peaks: r_1, $r_2 \ldots$	≈ 6	≈ 1	> 0

Table 6.1 The set of criteria used to quantitatively identify various morphologies in terms of the RDF $g(r)$, the local density function I, the occupation factor A, and the parameter ε (for details, see the text).

In conclusion, using molecular dynamics simulations, we analyzed the pattern formation and identified different morphologies in a system of particles interacting via a non-monotonic competing range potential, with a repulsive short-range part and attractive long-range part. The form of the interacting potential is rather general: it describes, depending on the specific parameters, the interparticle interaction in a variety of physical systems ranging from,

e.g., atoms and molecules (Lennard-Jones potential) to colloids and vortices in superconductors. In particular, it can be used as a model of vortex-vortex interaction in low κ type-II superconductors and in recently discovered so-called "type-1.5" superconductors. The obtained different morphologies were summarized in a morphology diagram in the plane "critical radius r_c − density n" (r_c is the critical radius where the interaction force changes its sign). We also analyzed the influence of the hardness of the "core", i.e., the strength of the repulsive core part of the interaction potential on the pattern formation.

We developed a set of criteria in order to unambiguously identify the obtained types of patterns using the following approaches: (i) the Radial Distribution Function (RDF) $g(r)$, (ii) the local density function I, and (iii) the occupation factor A. In addition, we introduced a parameter which characterizes the degree of perfection of a lattice ε. Employing these approaches, we elaborated a set of criteria for the identification of the different morphologies which are summarized in Table 6.1.

Summary

In what follows, we summarize the main results of our study in the order they are presented in this thesis.

In **Chapters** 2 and 3, we performed a systematic study of vortex configurations in mesoscopic superconducting squares and triangles, respectively. We compared the results with vortex patterns observed experimentally in μm-sized Nb squares using the Bitter decoration technique. In the theoretical analysis we relied upon the analytical solution of the London equation in mesoscopic squares and triangles by using the Green function method and the image technique. We calculated the vortex configurations and revealed the filling rules for squares and triangles with growing number of vortices L when gradually increasing the applied magnetic field. In particular, we found that for both triangles and squares and small L, vortices tend to form patterns that are commensurate with the symmetry of the corresponding boundaries of the sample. The filling of "shells" (similar to mesoscopic disks) occurs by periodic filling of the outermost and internal shells. In addition, we showed that some states rarely observed in experiments are due to weak pinning. We also studied the vortex states under the transformation from a square to a rectangle. We found that the states, which are symmetric with respect to the diagonal of the squares, are strongly deformed.

In **Chapter** 4, we investigated theoretically the effect of disorder on the static vortex lattice in the presence of a regular square array of pinning sites, and in **Chapter** 5 we analyzed the competitive effect of disorder and vortex-vortex interaction on the dynamics of vortices. Particularly, in **Chapter** 4, typical elastic defects of vortex lattices have been identified for some limiting and simple cases, and their energies and sizes have been estimated analytically. Other regions were studied numerically. By comparing the defect energy and random pinning energy, we constructed an approximate phase diagram of the system in the plane of random and regular pinning strengths. We also analyzed an intermediate regime for values of regular pinning strength, which are between the regimes of collective and single-vortex pinning. We found that both the elastic chains of depinned vortices and domains of totally depinned vortices vanish with increasing regular pinning strength. Therefore, all the regimes of disordering evolve from a collective pinning to single-vortex pin-

ning. In **Chapter** 5, we studied the competitive effect of periodic square and weak random pinning potentials on the dynamics of vortices. We found new dynamical regimes when vortices move in a soliton-like collective structure travelling within individual vortex rows. These are kinks, each containing an excess vortex, and antikinks containing a vacancy. We revealed three dynamical regimes: (i) initial motion is triggered by depinning of preexisted static kinks and antikinks; (ii) moving defects generate secondary kink-antikink pairs in adjacent rows at certain weak points assisted by random pinning; (iii) these pairs are freely generated by moving kinks and antikinks, i.e., without the help of disorder.

In **Chapter** 6, we analyzed pattern formation and identified different morphologies in a system of particles interacting via a non-monotonic competing potential, with a repulsive short-range part and an attractive long-range part. The form of the interacting potential is rather general: it describes, depending on the specific parameters, the inter-particle interaction in a variety of physical systems ranging from, e.g., atoms and molecules (Lennard-Jones potential) to colloids and vortices in superconductors. In particular, it can be used as a model of the vortex-vortex interaction in low κ type-II superconductors and in recently discovered so-called "type-1.5" superconductors. The obtained different morphologies were summarized in a morphology diagram in the plane "critical radius r_c − density n" (r_c is the critical radius where the interaction force changes its sign). We also analyzed the influence of the hardness of the "core", i.e., the strength of the repulsive core part of the interaction potential on the pattern formation. We developed a set of criteria in order to unambiguously identify the obtained types of patterns using the following approaches: (i) the radial distribution function (RDF) $g(r)$, (ii) the local density function I, and (iii) the occupation factor A. In addition, we introduced a parameter which characterizes the degree of perfection of a lattice ε. Employing these approaches, we elaborated a set of criteria for the identification of the different morphologies.

Finally, we would like to mention that the results of this thesis are applicable not only to vortices in superconductors, but also to a broader class of physical systems, e.g., vortices in ultracold gases, colloids, macroscopic elastic balls interacting via Coulomb forces, charge and spin density waves, etc.

Samenvatting

In wat volgt hebben we de belangrijkste resultaten van onze studie samengevat in de volgorde waarin ze in deze thesis worden gepresenteerd.

In **Hoofdstuk** 2 en 3, hebben we respectievelijk een systematische studie van vortex configuraties in mesoscopische supergeleidende vierkanten en driehoeken uitgevoerd. We vergeleken de theoretische simulatie resultaten met de experimenteel verkregen vortrex-patronen in Nb μm-grootte vierkanten doormiddel van de Bitter-decoratie techniek. Een analytische oplossing van de London vergelijking werd verkregen voor mesoscopische vierkanten en driehoeken door gebruik te maken van de Green-functie methode en de afbeeldingstechniek. We berekenden de vortex configuraties en vonden de opvulregels voor vortices in vierkanten en driehoeken als functie van het aangelegde magnetische veld. Voor een klein aantal vortices hebben deze de neiging om patronen te vormen die in overeenstemming zijn met de symmetrie van het sample. Deze ring-achtige structuren worden gradueel opgevuld met een groter aantal vortices, en (gelijkaardig aan mesoscopicsche schijven) dit gebeurt door het periodieke vullen van de buitenste en de binnenste ringen. Bovendien, toonden we aan dat de toestanden die zelden werden waargenomen veroorzaakt worden door zwakke pinning. We bestudeerden ook de vortex toestanden tijdens de vervorming van vierkant naar rechthoek. We ontdekten dat de toestanden die symmetrisch zijn ten opzichte van de diagonalen van de vierkanten sterk vervormd zijn.

In **Hoofdstuk** 4 hebben we theoretisch het effect van wanorde onderzocht op het statisch vortex-rooster in de aanwezigheid van een regelmatig vierkantigrooster van pinning sites. In **Hoofdstuk** 5 onderzochten we de competitie tussen wanorde en vortex-vortex interacties op de dynamica van vortices. Eenvoudige elastische defecten werden geïdentificeerd in het vortex-rooster en hun energie en grootte werden analytisch benaderd. Een gedetailleerde numerieke studie werd uitgevoerd voor defecten van algemene vorm. Door hun defect-energie en random pinning-energie te vergelijken werd een benaderend fasediagram van het systeem opgesteld in het vlak van random en artificiële pinningsterktes. Verder werd er een intermediair gebied voor regelmatige pinningsterktes geannaliseerd, die gelegen zijn in het gebied tussen de regimes van collectieve en één-vortex pinning. We vonden dat elastische

ketens van vrije en domeinen van vortices verdwijnen met toenemende sterkte van de pinning. Daardoor evolueren alle regimes van wanorde van collectieve pinning naar één-vortex pinning.

In **Hoofdstuk** 5 hebben we het competitieve effect van een periodisch vierkantige en random zwakke pinning-potentiaal bestudeerd op de dynamica van vortices. We vonden nieuwe dynamische regimes waar vortices bewegen collectief in een soliton-achtige structuur, voortbewegend in individuele vortex-rijen. Verder werden er drie nieuwe regimes gevonden: (i) de initiële beweging is getriggerd door depinning van reeds bestaande statische kinks en anti-kinks; (ii) bewegende defecten genereren secondaire kink-anti-kink paren in nabijgelegen rijen en in bepaalde zwakke punten bijgestaan door pinning t.g.v. wanorde; (iii) deze paren worden vrij gegenereerd door bewegende kinks en anti-kinks (zonder de hulp van wanorde)

In **Hoofdstuk** 6 hebben we patroonvorming bestudeerd en verschillende morfologieën geïdentificeerd in een systeem van deeltjes die met elkaar interageren via een niet-monotone potentiaal met een repulsieve kortedracht- en een attractieve langedrachtterm. De precieze vorm van de interactiepotentiaal is algemeen gehouden: afhankelijk van de specifieke parameters beschrijft dit de interactie tussen deeltjes voor een gevarieerde klasse van fysische systemen gaande van, bijvoorbeeld, atomen en moleculen enerzijds tot colloïdale vloeistoffen en vortices in supergeleiders anderzijds. In het bijzonder kan de potentiaal worden gebruikt als een model om vortex-vortexinteracties te beschrijven in type-II supergeleiders met kleine κ en de recentelijk ontdekte "type-1.5" supergeleiders. De verschillende morfologieën die aldus werden verkregen, zijn samengebracht in een morfologiediagram dat de dichtheid n uitzet tegen de straal r_c (r_c is de kritieke straal waarbij de interactiekracht van teken verandert). We hebben ook uitgezocht hoe de hardheid van de "kern" – d.i. de grootte van het repulsieve deel van de kern in de interactiepotentiaal – de patroonvorming beïnvloedt. Vervolgens hebben we een aantal criteria ontwikkeld om de verkregen patroontypes ondubbelzinnig van elkaar te onderscheiden op basis van de volgende grootheden: i) de radiale distributiefunctie (RDF) $g(r)$, (ii) de lokale dichtheidsfunctie I en (iii) het bezettingsgetal A. Daarbovenop hebben we nog een parameter ϵ ingevoerd die de mate waarin het kristal ideaal is, beschrijft.

Tenslotte wijzen we er nog op dat de resultaten van dit proefschrift niet alleen van toepassing zijn op de studie van vortices in supergeleiders maar ook op een ruimere klasse van fysische systemen zoals vortices in ultrakoude gassen, colloïdale vloeistoffen, macroscopische, elastische bollen die door een Coulomb-potentiaal met elkaar interageren, ladings- en spindichtheidsgolven enzovoort.

Bibliography

1. H. K. Onnes, Leiden Comm. **122b**, 124 (1911).
2. J. File and R. G. Mills, Phys. Rev. Lett. **10**, 93 (1963).
3. W. Meissner and R. Ochsenfeld, Naturwissenschaften **21**, 787 (1933).
4. F. London and H. London, Proceedings of the Royal Society of London. Series A - Mathematical and Physical Sciences **149**, 71 (1935).
5. V. L. Ginzburg and L. D. Landau, Zh. Eksp. Teor. Fiz. **20**, 1064 (1950).
6. J. Bardeen, L. N. Cooper, and J. R. Schrieffer, Phys. Rev. **108**, 1175 (1957).
7. J. G. Bednorz and K. A. Müller, Zeitschrift für Physik B Condensed Matter **64**, 189 (1986).
8. M. K. Wu, J. R. Ashburn, C. J. Torng, P. H. Hor, R. L. Meng, L. Gao, Z. J. Huang, Y. Q. Wang, and C. W. Chu, Phys. Rev. Lett. **58**, 908 (1987).
9. P. Dai, B. Chakoumakos, G. Sun, K. Wong, Y. Xin, and D. Lu, Physica C: Superconductivity **243**, 201 (1995).
10. M. Tinkham, *Introduction to superconductivity, 2ed* (McGraw-Hill, New York, 1996).
11. K. Charles, *Introduction to Solid State Physics* (John Wiley & Sons, 2004).
12. L. N. Cooper, Phys. Rev. **104**, 1189 (1956).
13. A. L. Fetter, P. C. Hohenberg, and P. Pincus, Phys. Rev. **147**, 140 (1966).
14. A. Buzdin and J. Brison, Physics Letters A **196**, 267 (1994).
15. E. Sardella, M. M. Doria, and P. R. S. Netto, Phys. Rev. B **60**, 13158 (1999).

16. L. Kramer, Phys. Rev. B **3**, 3821 (1971).

17. F. Mohamed, M. Troyer, G. Blatter, and I. Luk'yanchuk, Phys. Rev. B **65**, 224504 (2002).

18. E. H. Brandt and U. Essmann, physica status solidi (b) **144**, 13 (1987).

19. E. Brandt and M. Das, J. Supercond. Novel Magn. **24**, 57 (2011).

20. I. Luk'yanchuk, Phys. Rev. B **63**, 174504 (2001).

21. C. Reichhardt, C. J. Olson, I. Martin, and A. R. Bishop, Europhys. Lett. **61**, 221 (2003).

22. C. Reichhardt, C. J. O. Reichhardt, I. Martin, and A. R. Bishop, Phys. Rev. Lett. **90**, 026401 (2003).

23. C. Reichhardt, C. J. O. Reichhardt, and A. R. Bishop, Europhys. Lett. **72**, 444 (2005).

24. X. B. Xu, H. Fangohr, S. Y. Ding, F. Zhou, X. N. Xu, Z. H. Wang, M. Gu, D. Q. Shi, and S. X. Dou, Phys. Rev. B **83**, 014501 (2011).

25. X. B. Xu, H. Fangohr, Z. H. Wang, M. Gu, S. L. Liu, D. Q. Shi, and S. X. Dou, Phys. Rev. B **84**, 014515 (2011).

26. V. Moshchalkov, M. Menghini, T. Nishio, Q. H. Chen, A. V. Silhanek, V. H. Dao, L. F. Chibotaru, N. D. Zhigadlo, and J. Karpinski, Phys. Rev. Lett. **102**, 117001 (2009).

27. A. Chaves, L. Komendová, M. V. Milošević, J. S. Andrade, G. A. Farias, and F. M. Peeters, Phys. Rev. B **83**, 214523 (2011).

28. L. Komendová, M. V. Milošević, A. A. Shanenko, and F. M. Peeters, Phys. Rev. B **84**, 064522 (2011).

29. E. Babaev and M. Speight, Phys. Rev. B **72**, 180502 (2005).

30. P. Hänggi and F. Marchesoni, Rev. Mod. Phys. **81**, 387 (2009).

31. P. Chaikin and T. Lubensky, *Principles of condensed matter physics* (Cambridge Univ. Press, Cambridge, 1995).

32. H. Träuble and U. Essmann, physica status solidi (b) **18**, 813 (1966).

33. U. Essmann and H. Träuble, Phys. Lett. **54A**, 596 (1967).

34. N. V. Sarma and J. R. Moon, Philosophical Magazine **16**, 433 (1967), http://www.tandfonline.com/doi/pdf/10.1080/14786436708220854 .

35. I. V. Grigorieva, Supercond. Sci. Technol. **7**, 161 (1994).

36. J. R. Kirtley, Reports on Progress in Physics **73**, 126501 (2010).

37. A. Finkler, Y. Segev, Y. Myasoedov, M. L. Rappaport, L. Ne' eman, D. Vasyukov, E. Zeldov, M. E. Huber, J. Martin, and A. Yacoby, Nano Letters **10**, 1046 (2010).

38. A. M. Chang, H. D. Hallen, L. Harriott, H. F. Hess, H. L. Kao, J. Kwo, R. E. Miller, R. Wolfe, J. van der Ziel, and T. Y. Chang, Applied Physics Letters **61**, 1974 (1992).

39. A. K. Geim, I. V. Grigorieva, S. V. Dubonos, J. G. S. Lok, J. C. Maan, A. E. Filippov, and F. M. Peeters, Nature (London) **390**, 259 (1997).

40. P. S. Deo, V. A. Schweigert, F. M. Peeters, and A. K. Geim, Phys. Rev. Lett. **79**, 4653 (1997).

41. Y. E. Lozovik and E. A. Rakoch, Phys. Rev. B **57**, 1214 (1998).

42. V. A. Schweigert and F. M. Peeters, Phys. Rev. B **57**, 13817 (1998).

43. V. A. Schweigert and F. M. Peeters, Phys. Rev. Lett. **83**, 2409 (1999).

44. B. J. Baelus, F. M. Peeters, and V. A. Schweigert, Phys. Rev. B **63**, 144517 (2001).

45. B. J. Baelus, L. R. E. Cabral, and F. M. Peeters, Phys. Rev. B **69**, 064506 (2004).

46. V. R. Misko, B. Xu, and F. M. Peeters, Phys. Rev. B **76**, 024516 (2007).

47. I. V. Grigorieva, W. Escoffier, J. Richardson, L. Y. Vinnikov, S. Dubonos, and V. Oboznov, Phys. Rev. Lett. **96**, 077005 (2006).

48. A. Kanda, B. J. Baelus, F. M. Peeters, K. Kadowaki, and Y. Ootuka, Phys. Rev. Lett. **93**, 257002 (2004).

49. L. Chibotaru, A. Ceulemans, V. Bruyndoncx, and V. Moshchalkov, Nature (London) **408**, 833 (2000).

50. L. F. Chibotaru, A. Ceulemans, V. Bruyndoncx, and V. V. Moshchalkov, Phys. Rev. Lett. **86**, 1323 (2001).

51. V. R. Misko, V. M. Fomin, J. T. Devreese, and V. V. Moshchalkov, Phys. Rev. Lett. **90**, 147003 (2003).

52. R. Geurts, M. V. Milošević, and F. M. Peeters, Phys. Rev. B **75**, 184511 (2007).

53. J. J. Palacios, Phys. Rev. B **58**, R5948 (1998).

54. A. K. Geim, S. V. Dubonos, J. J. Palacios, I. V. Grigorieva, M. Henini, and J. J. Schermer, Phys. Rev. Lett. **85**, 1528 (2000).

55. M. V. Milošević, S. V. Yampolskii, and F. M. Peeters, Phys. Rev. B **66**, 024515 (2002).

56. M. V. Milošević and F. M. Peeters, Phys. Rev. B **68**, 024509 (2003).

57. I. V. Grigorieva, W. Escoffier, V. R. Misko, B. J. Baelus, F. M. Peeters, L. Y. Vinnikov, and S. V. Dubonos, Phys. Rev. Lett. **99**, 147003 (2007).

58. V. Moshchalkov, L. Gielen, C. Strunk, R. Jonckheere, X. Qiu, C. Van-haesendonck, and Y. Bruynseraede, Nature **373**, 319 (1995).

59. V. Bruyndoncx, J. G. Rodrigo, T. Puig, L. Van Look, V. V. Moshchalkov, and R. Jonckheere, Phys. Rev. B **60**, 4285 (1999).

60. V. Fomin, V. Misko, J. Devreese, and V. Moshchalkov, Solid State Communications **101**, 303 (1997).

61. V. M. Fomin, V. R. Misko, J. T. Devreese, and V. V. Moshchalkov, Phys. Rev. B **58**, 11703 (1998).

62. V. A. Schweigert and F. M. Peeters, Phys. Rev. B **60**, 3084 (1999).

63. H. T. Jadallah, J. Rubinstein, and P. Sternberg, Phys. Rev. Lett. **82**, 2935 (1999).

64. T. Schuster, H. Kuhn, E. H. Brandt, and S. Klaumünzer, Phys. Rev. B **56**, 3413 (1997).

65. G. P. Mikitik and E. H. Brandt, Phys. Rev. B **62**, 6800 (2000).

66. B. J. Baelus and F. M. Peeters, Phys. Rev. B **65**, 104515 (2002).

67. J. Bonča and V. V. Kabanov, Phys. Rev. B **65**, 012509 (2001).

68. A. S. Mel'nikov, I. M. Nefedov, D. A. Ryzhov, I. A. Shereshevskii, V. M. Vinokur, and P. P. Vysheslavtsev, Phys. Rev. B **65**, 140503 (2002).

69. T. Mertelj and V. V. Kabanov, Phys. Rev. B **67**, 134527 (2003).

70. V. Misko, V. Fomin, J. Devreese, and V. Moshchalkov, Physica C: Superconductivity **369**, 361 (2002).

71. R. Geurts, M. V. Milošević, and F. M. Peeters, Phys. Rev. Lett. **97**, 137002 (2006).

72. M. Baert, V. V. Metlushko, R. Jonckheere, V. V. Moshchalkov, and Y. Bruynseraede, Phys. Rev. Lett. **74**, 3269 (1995).

73. V. V. Moshchalkov, M. Baert, V. V. Metlushko, E. Rosseel, M. J. Van Bael, K. Temst, R. Jonckheere, and Y. Bruynseraede, Phys. Rev. B **54**, 7385 (1996).

74. A. T. Fiory, A. F. Hebard, and S. Somekh, Appl. Phys. Lett. **32**, 73 (1978).

75. A. Castellanos, R. Wördenweber, G. Ockenfuss, A. v.d. Hart, and K. Keck, Appl. Phys. Lett. **71**, 962 (1997).

76. R. Wördenweber, P. Dymashevski, and V. R. Misko, Phys. Rev. B **69**, 184504 (2004).

77. J. Eisenmenger, Z.-P. Li, W. A. A. Macedo, and I. K. Schuller, Phys. Rev. Lett. **94**, 057203 (2005).

78. J. E. Villegas, E. M. Gonzalez, M. I. Montero, I. K. Schuller, and J. L. Vicent, Phys. Rev. B **68**, 224504 (2003).

79. M. I. Montero, J. J. Åkerman, A. Varilci, and I. K. Schuller, Europhys. Lett. **63**, 118 (2003).

80. J. E. Villegas, S. Savel'ev, F. Nori, E. M. Gonzalez, J. V. Anguita, R. García, and J. L. Vicent, Science **302**, 1188 (2003).

81. L. Van Look, B. Y. Zhu, R. Jonckheere, B. R. Zhao, Z. X. Zhao, and V. V. Moshchalkov, Phys. Rev. B **66**, 214511 (2002).

82. A. V. Silhanek, S. Raedts, M. Lange, and V. V. Moshchalkov, Phys. Rev. B **67**, 064502 (2003).

83. M. Kemmler, C. Gürlich, A. Sterck, H. Pöhler, M. Neuhaus, M. Siegel, R. Kleiner, and D. Koelle, Phys. Rev. Lett. **97**, 147003 (2006).

84. A. V. Silhanek, W. Gillijns, V. V. Moshchalkov, B. Y. Zhu, J. Moonens, and L. H. A. Leunissen, Appl. Phys. Lett. **89**, 152507 (2006).

85. F. Nori, Science **271**, 1373 (1996).

86. C. Reichhardt, C. J. Olson, J. Groth, S. Field, and F. Nori, Phys. Rev. B **52**, 10441 (1995).

87. C. Reichhardt, C. J. Olson, J. Groth, S. Field, and F. Nori, Phys. Rev. B **53**, R8898 (1996).

88. C. Reichhardt, J. Groth, C. J. Olson, S. B. Field, and F. Nori, Phys. Rev. B **54**, 16108 (1996).

89. C. Reichhardt, J. Groth, C. J. Olson, S. B. Field, and F. Nori, Phys. Rev. B **56**, 14196 (1997).

90. C. Reichhardt, C. J. Olson, and F. Nori, Phys. Rev. Lett. **78**, 2648 (1997).

91. C. Reichhardt, C. J. Olson, and F. Nori, Phys. Rev. B **57**, 7937 (1998).

92. C. Reichhardt, C. J. Olson, and F. Nori, Phys. Rev. B **58**, 6534 (1998).

93. V. R. Misko, S. Savel'ev, A. L. Rakhmanov, and F. Nori, Phys. Rev. Lett. **96**, 127004 (2006).

94. V. R. Misko, S. Savel'ev, A. L. Rakhmanov, and F. Nori, Phys. Rev. B **75**, 024509 (2007).

95. G. R. Berdiyorov, M. V. Milošević, and F. M. Peeters, Phys. Rev. B **74**, 174512 (2006).

96. G. R. Berdiyorov, M. V. Milošević, and F. M. Peeters, Phys. Rev. B **76**, 134508 (2007).

97. V. Misko, S. Savel'ev, and F. Nori, Phys. Rev. Lett. **95**, 177007 (2005).

98. V. R. Misko, S. Savel'ev, and F. Nori, Phys. Rev. B **74**, 024522 (2006).

99. V. R. Misko, S. Savel' ev, and F. Nori, Physica C: Superconductivity **437 - 438**, 213 (2006).

100. V. Rudko, O. Shevtsova, and S. Shiyanovsky, Fiz. Nizk. Temp. **22**, 1314 (1996).

101. C. Reichhardt, C. J. Olson, R. T. Scalettar, and G. T. Zimányi, Phys. Rev. B **64**, 144509 (2001).

102. W. V. Pogosov, A. L. Rakhmanov, and V. V. Moshchalkov, Phys. Rev. B **67**, 014532 (2003).

103. Q. H. Chen, G. Teniers, B. B. Jin, and V. V. Moshchalkov, Phys. Rev. B **73**, 014506 (2006).

104. C. Reichhardt and C. J. O. Reichhardt, Phys. Rev. B **76**, 064523 (2007).

105. V. Zhuravlev and T. Maniv, Phys. Rev. B **68**, 174507 (2003).

106. G. Berdiyorov, M. V. Milošević, and F. M. Peeters, Physica C: Superconductivity **468**, 809 (2008).

107. J. W. Reijnders and R. A. Duine, Phys. Rev. Lett. **93**, 060401 (2004).

108. H. Pu, L. O. Baksmaty, S. Yi, and N. P. Bigelow, Phys. Rev. Lett. **94**, 190401 (2005).

109. S. Tung, V. Schweikhard, and E. A. Cornell, Phys. Rev. Lett. **97**, 240402 (2006).

110. G. Coupier, M. Saint Jean, and C. Guthmann, Phys. Rev. B **75**, 224103 (2007).

111. K. Mangold, P. Leiderer, and C. Bechinger, Phys. Rev. Lett. **90**, 158302 (2003).

112. D. Deb and H. H. von Grünberg, Journal of Physics: Condensed Matter **20**, 245104 (2008).

113. A. Libál, C. Reichhardt, and C. J. O. Reichhardt, Phys. Rev. Lett. **97**, 228302 (2006).

114. O. M. Braun and Y. S. Kivshar, *The Frenkel-Kotorova Model* (Springer, Cambridge, 2004).

115. E. Y. Vedmedenko, *Competing interactions and patterns in nanoworld* (WILEY-VCH Verlag GmbH & Co. KGaA, 2007).

116. V. M. Kaganer, H. Möhwald, and P. Dutta, Rev. Mod. Phys. **71**, 779 (1999).

117. K. A. Suresh, J. Nittmann, and F. Rondelez, Europhys. Lett. **6**, 437 (1988).

118. N. Hoffmann, F. Ebert, C. N. Likos, H. Löwen, and G. Maret, Phys. Rev. Lett. **97**, 078301 (2006).

119. P. J. Lu, E. Zaccarelli, F. Ciulla, A. B. Schofield, F. Sciortino, and D. A. Weitz, Nature **453**, 499 (2008).

120. A. I. Campbell, V. J. Anderson, J. S. van Duijneveldt, and P. Bartlett, Phys. Rev. Lett. **94**, 208301 (2005).

121. C. L. Klix, C. P. Royall, and H. Tanaka, Phys. Rev. Lett. **104**, 165702 (2010).

122. F. F. Munarin, K. Nelissen, W. P. Ferreira, G. A. Farias, and F. M. Peeters, Phys. Rev. E **77**, 031608 (2008).

123. M. F. Islam, K. H. Lin, D. Lacoste, T. C. Lubensky, and A. G. Yodh, Phys. Rev. E **67**, 021402 (2003).

124. D. Lacoste and T. C. Lubensky, Phys. Rev. E **64**, 041506 (2001).

125. R. E. Rosensweig, M. Zahn, and R. Shumovich, J. Magn. Magn. Mater. **39**, 127 (1983).

126. A. Tsebers and M. Maiorov, Magnetohydrodynamics (New York) **16**, 21 (1980).

127. G. R. Berdiyorov, A. D. Hernandez, and F. M. Peeters, Phys. Rev. Lett. **103**, 267002 (2009).

128. C. J. Horowitz, M. A. Pérez-García, and J. Piekarewicz, Phys. Rev. C **69**, 045804 (2004).

129. M. Seul and D. Andelman, Science **267**, 476 (1995).

130. F. Sciortino and P. Tartaglia, Advances in Physics **54**, 471 (2005).

131. F. Sciortino, S. Mossa, E. Zaccarelli, and P. Tartaglia, Phys. Rev. Lett. **93**, 055701 (2004).

132. M. Tarzia and A. Coniglio, Phys. Rev. Lett. **96**, 075702 (2006).

133. M. Tarzia and A. Coniglio, Phys. Rev. E **75**, 011410 (2007).

134. S. Mossa, F. Sciortino, P. Tartaglia, and E. Zaccarelli, Langmuir **20**, 10756 (2004).

135. A. de Candia, E. Del Gado, A. Fierro, N. Sator, M. Tarzia, and A. Coniglio, Phys. Rev. E **74**, 010403 (2006).

136. H. J. Zhao, V. R. Misko, F. M. Peeters, V. Oboznov, S. V. Dubonos, and I. V. Grigorieva, Phys. Rev. B **78**, 104517 (2008).

137. V. R. Misko, H. J. Zhao, F. M. Peeters, V. Oboznov, S. V. Dubonos, and I. V. Grigorieva, Superconductor Science and Technology **22**, 034001 (2009).

138. A. Abrikosov, *Fundamentals of the Theory of Metals* (North-Holland, Amsterdam, 1986).

139. J. Ketterson and S. Song, *Superconductivity* (Cambridge University Press, 1999).

140. L. R. E. Cabral, B. J. Baelus, and F. M. Peeters, Phys. Rev. B **70**, 144523 (2004).

141. V. M. Bedanov and F. M. Peeters, Phys. Rev. B **49**, 2667 (1994).

142. K. Harada, O. Kamimura, H. Kasai, T. Matsuda, A. Tonomura, and V. V. Moshchalkov, Science **274**, 1167 (1996).

143. B. J. Baelus, A. Kanda, N. Shimizu, K. Tadano, Y. Ootuka, K. Kadowaki, and F. M. Peeters, Phys. Rev. B **73**, 024514 (2006).

144. A rhombus-shaped vortex state is not consistent with the C_4-symmetry and it does not appear as a metastable state in a *perfect* square for $L = 4$. However, the presence of imperfections (or other vortices as, e.g., outer-shell vortices for states with $L = 12$ and 16) favors appearance of triangular- or rhombus-shaped vortex configurations.

145. M. F. Laguna, C. A. Balseiro, D. Domínguez, and F. Nori, Phys. Rev. B **64**, 104505 (2001).

146. B. Zhu, F. Marchesoni, and F. Nori, Physica E: Low-dimensional Systems and Nanostructures **18**, 318 (2003).

147. B. Zhu, L. V. Look, V. Moshchalkov, F. Marchesoni, and F. Nori, Physica E: Low-dimensional Systems and Nanostructures **18**, 322 (2003).

148. B. Y. Zhu, F. Marchesoni, and F. Nori, Phys. Rev. Lett. **92**, 180602 (2004).

149. Y. Togawa, K. Harada, T. Akashi, H. Kasai, T. Matsuda, F. Nori, A. Maeda, and A. Tonomura, Phys. Rev. Lett. **95**, 087002 (2005).

150. J. Van de Vondel, C. C. de Souza Silva, B. Y. Zhu, M. Morelle, and V. V. Moshchalkov, Phys. Rev. Lett. **94**, 057003 (2005).

151. C. de Souza Silva, J. V. de Vondel, M. Morelle, and V. Moshchalkov, Nature **440**, 651 (2006).

152. S. Savel'ev, V. Misko, F. Marchesoni, and F. Nori, Phys. Rev. B **71**, 214303 (2005).

153. E. M. Gonzalez, N. O. Nunez, J. V. Anguita, and J. L. Vicent, Appl. Phys. Lett. **91**, 062505 (2007).

154. A. V. Silhanek, J. V. de Vondel, V. V. Moshchalkov, A. Leo, V. Metlushko, B. Ilic, V. R. Misko, and F. M. Peeters, Appl. Phys. Lett. **92**, 176101 (2008).

155. H. J. Zhao, V. R. Misko, F. M. Peeters, S. Dubonos, V. Oboznov, and I. V. Grigorieva, Europhys. Lett. **83**, 17008 (2008).

156. B. J. McCartin, SIAM Review **45**, 267 (2003).

157. G. R. Berdiyorov, V. R. Misko, M. V. Milošević, W. Escoffier, I. V. Grigorieva, and F. M. Peeters, Phys. Rev. B **77**, 024526 (2008).

158. W. V. Pogosov, V. R. Misko, H. J. Zhao, and F. M. Peeters, Phys. Rev. B **79**, 014504 (2009).

159. A. A. Zhukov, H. Küpfer, G. K. Perkins, A. D. Caplin, T. Wolf, K. I. Kugel, A. L. Rakhmanov, M. G. Mikheev, V. I. Voronkova, M. Kläser, and H. Wühl, Phys. Rev. B **59**, 11213 (1999).

160. K. Kugel, A. Rakhmanov, and A. Zhukov, Physica C: Superconductivity **334**, 203 (2000).

161. I. Voloshin, A. Kalinov, L. Fisher, K. Kugel' , and A. Rakhmanov, Journal of Experimental and Theoretical Physics **84**, 1177 (1997).

162. G. Blatter, M. V. Feigel'man, V. B. Geshkenbein, A. I. Larkin, and V. M. Vinokur, Rev. Mod. Phys. **66**, 1125 (1994).

163. W. V. Pogosov, H. J. Zhao, V. R. Misko, and F. M. Peeters, Phys. Rev. B **81**, 024513 (2010).

164. See supplementary material at
http://link.aps.org/supplemental/10.1103/PhysRevB.81.024513 for
Mov. 1. Regime-I: Motion of individual stripes, preexisted in the system.
Mov. 2. Regime-II: Generation of kink-antikink pairs by simultaneous effect of disorder and moving defects.
Mov. 3. Regime-III: Free generation of kink-antikink pairs by moving defects.

165. V. V. Konotop and L. Vazquez, *Nonlinear Random Waves* (World Scientific Publishing, Singapore, 1994).

166. J. Gutierrez, A. V. Silhanek, J. Van de Vondel, W. Gillijns, and V. V. Moshchalkov, Phys. Rev. B **80**, 140514 (2009).

167. M. Kemmler, D. Bothner, K. Ilin, M. Siegel, R. Kleiner, and D. Koelle, Phys. Rev. B **79**, 184509 (2009).

168. C. Reichhardt and C. J. O. Reichhardt, Phys. Rev. B **76**, 094512 (2007).

169. H. J. Zhao, V. R. Misko, and F. M. Peeters, Physica C: Superconductivity (2012), 10.1016/j.physc.2011.12.033.

170. H. J. Zhao, V. R. Misko, and F. M. Peeters, arXiv:1107.0699 (New journal of Physics (accepted)) (2012).

171. V. R. Misko, D. Bothner, M. Kemmler, R. Kleiner, D. Koelle, F. M. Peeters, and F. Nori, Phys. Rev. B **82**, 184512 (2010).

172. Note that we do not characterize the interaction force as "short-range repulsive and long-range attractive" since both the contributions are rather "short-range", due to the Bessel functions. The fact that the interaction is short-range allows us to use a cut-off for long distances.

173. R. Plass, J. Last, N. Bartelt, and G. Kellogg, Nature **412**, 875 (2001).

174. R. Plass, N. C. Bartelt, and G. L. Kellogg, Journal of Physics: Condensed Matter **14**, 4227 (2002).

175. J. C. Crocker and D. G. Grier, Journal of Colloid and Interface Science **179**, 298 (1996).

176. D. Frenkel and B. Smit, *Understanding molecular simulation : from algorithms to applications*, 2nd ed. (Academic Press, 2002).

CURRICULUM VITAE

Personal Data

Name: Haijun Zhao

Born in Minqin City, Gansu Province, P. R. China on June 11*th*, 1982

Nationality: Chinese

Email: zhaonavy@gmail.com

Education

2007-2012	Ph.D in Condensed Matter Theory	Universiteit Antwerpen, Belgium
2006-2007	Adv. M. S. in Nanophysics	Universiteit Antwerpen, Belgium
2002-2006	B. S. in Physics	Zhejiang University, China

List of Publications

H. J. Zhao, V. R. Misko, F. M. Peeters, S. Dubonos, V. Oboznov and I. V. Grigorieva, *Vortex configurations in mesoscopic superconducting triangles: Finite-size and shape effects*, Europhys. Lett. **83**, 17008 (2008).

H. J. Zhao, V. R. Misko, F. M. Peeters, V. Oboznov, S. V. Dubonos and I. V. Grigorieva, *Vortex states in mesoscopic superconducting squares: Formation of vortex shells*, Phys. Rev. B **78**, 104517 (2008). Also selected for: the October 1, 2008 issue of Virtual Journal of Applications of Superconductivity.

V. R. Misko, H. J. Zhao, and F. M. Peeters, V. Oboznov, S. V. Dubonos and I. V. Grigorieva, *Formation of vortex shells in mesoscopic superconducting squares*, Supercond. Sci. Technol. **21**, 034001 (2009).

W. V. Pogosov, V. R. Misko, H. J. Zhao, and F. M. Peeters, *Collective vortex phases in*

periodic plus random pinning potential, Phys. Rev. B 79, 014504 (2009). Also featured in: APS Kaleidoscope, February 2009: (http://prb.aps.org/kaleidoscope).

W. V. Pogosov, H. J. Zhao, V. R. Misko, and F. M. Peeters, *Kink-antikink vortex transfer in periodic-plus-random pinning potential: Theoretical analysis and numerical experiments*, Phys. Rev. B 81, 024513 (2010). Also selected for: the February 1, 2010 issue of Virtual Journal of Applications of Superconductivity.

H. J. Zhao, V. R. Misko, and F. M. Peeters, *Pattern formation and phase transitions in systems with non-monotonic interaction*, New Journal of Physics (accepted), arXiv:1107.0699v1 [cond-mat.soft] 4 July 2011.

H. J. Zhao, V. R. Misko, and F. M. Peeters, *Vortex Configurations with nonmonotonic interaction*, Physica C: Superconductivity (2012), doi:10.1016/j.physc.2011.12.033.

Participation in conferences & workshops

Vortex structures in mesoscopic superconducting squares and triangles: the London approach; H. J. Zhao, V.R. Misko, and F.M. Peeters, Abstracts of General Meeting of IAP, November 22nd, 2007, Liege, Belgium. – Poster.

Vortex configurations in mesoscopic superconducting triangles: finite-size and shape effects; H. J. Zhao, V.R. Misko, F.M. Peeters, and I.V. Grigorieva, Abstracts of BPS General Scientific Meeting, CM50, p. 102. May 21st, 2008, Brussels, Belgium. – Poster.

Shape and pinning induced vortex states in mesoscopic superconductors; V.R. Misko, H. J. Zhao, B. Xu, B.J. Baelus, F.M. Peeters, I.V. Grigorieva, W. Escoffier, L.Y. Vinnikov, and S.V. Dubonos, Abstracts of the 25th International conference on low Temperature physics (LT25), August 6th-13th, 2008, Amsterdam, Holland. – Poster.

Vortex configurations in mesoscopic superconducting triangles: Finite-size and shape effects, H. J. Zhao, V.R. Misko, F.M. Peeters, S. Dubonos, V. Oboznov, and I.V. Grigorieva; Winter School on Multiscale Simulation Methods in Molecular Sciences, Forschungszentrum Jülich, Germany, March 2-6, 2009. – Poster.

Vortex configurations in mesoscopic superconducting squares and triangles: Formation of vortex shells; H. J. Zhao, V. R. Misko, F. M. Peeters, V. Oboznov, S. V. Dubonos and I. V. Grigorieva, Abstracts of BPS General Scientific Meeting, C14, p. 43. April 1st, 2009, Hasselt, Belgium. – Poster.

Collective vortex phases in periodic plus random pinning potential; V. R. Misko, W. V. Pogosov, H. J. Zhao, and F. M. Peeters, Abstract Book of the General Scientific Meeting of the Belgian Physical Society & Belgian Biophysical Society, C35, p. 54, Universiteit Hasselt, Belgium, April 1st 2009. – Poster.

Collective vortex phases in periodic plus random pinning potential; H. J. Zhao W. V. Pogosov, V. R. Misko and F. M. Peeters, Abstracts of the 9th European Conference on Applied Superconductivity, September 17th, 2009, Dresden, Germany. – Talk.

Vortex lattice in the system of periodic plus random pinning centra; W. V. Pogosov, V. R. Misko, H. J. Zhao, and F. M. Peeters, Abstracts of the 35th Conference on Low-Temperature Physics (LT-35), Chernogolovka, Russia, 29 September - 2 October, 2009, p. 287. – Talk.

Lattice structure in systems with non-monotonic interaction; H. J. Zhao, V. R. Misko and F. M. Peeters, IAP Workshop on Two-Band Superconductivity and Related Topics, 27 January 2011, Antwerp, Belgium. – Talk.

Lattice formation and phase transitions in systems of particles with non-monotonic interaction; Vyacheslav R. Misko, Haijun Zhao, and Francois M. Peeters, Abstracts of the International Conference on Stimuli Responsive Particles and Particle Assemblies (Particles 2011), Holiday Inn Berlin-City West, Berlin, Germany, 9-12 July 2011. – Contributed Paper 82, p. 93.

Pattern formation and phase transitions in systems with non-monotonic interaction; H. J. Zhao, V. R. Misko and F. M. Peeters, The seventh international Conference on vortex matter in nanostructured superconductors (VORTEX VII) September 10-17th, Rhodes, Greece. – Poster.

Vortex mobility and guided vortex motion in superconductors with antidot arrays in presence of ac and dc driving; V. R. Misko, H. J. Zhao, and R. Wördenweber, The seventh international Conference on vortex matter in nanostructured superconductors (VORTEX VII) September 10-17th, Rhodes, Greece. – Invited Talk.

Winter School

Winter School on Multiscale Simulation Methods in Molecular Sciences, Forschungszentrum Jülich, Germany, March 2-6, 2009.

Scientific award

Chinese Government Award for Outstanding Self-Financed Students Abroad (2011)